**Hierarchical Selective Electrokinetic Concentration: the Universal Next-Generation Biomolecule Enrichment Technique for Molecular Diagnostics**

by

Wei Ouyang

S.M. in Electrical Engineering, Massachusetts Institute of Technology

B.S. in Electrical Engineering, Peking University, Beijing, P.R. China

Submitted to the Department of Electrical Engineering and Computer Science
in partial fulfillment of the requirements for the degree of
Doctor of Philosophy
at the
Massachusetts Institute of Technology
February 2020



Signature of the author: Signature redacted

Department of Electrical Engineering and Computer Science
January 8, 2020

Certified by: Signature redacted

Jongyoon Han
Professor of Electrical Engineering and Biological Engineering
Thesis Supervisor

Accepted by: Signature redacted

Leslie A. Kolodziejski
Professor of Electrical Engineering and Computer Science
Chair, Department Committee on Graduate Students

**Hierarchical Selective Electrokinetic Concentration: the Universal Next-Generation Biomolecule Enrichment Technique for Molecular Diagnostics**

by Wei Ouyang

Submitted to the Department of Electrical Engineering and Computer Science
on January 8, 2020, in partial fulfillment of the
requirements for the degree of
Doctor of Philosophy

**Abstract**

Rapid and reliable detection of ultralow-abundance nucleic acids and proteins in complex biological media may greatly advance clinical diagnostics and biotechnology development. Because of the slow mass transport and weak binding kinetics at ultralow concentration of target biomolecules, enrichment of target biomolecules plays an essential role in the detection of ultralow-abundance biomolecules. Currently, nucleic acid tests rely on enzymatic processes for target amplification (*e.g.* polymerase chain reaction), which have many inherent issues restricting their implementation in diagnostics. On the other hand, there exist no protein amplification techniques, greatly limiting the development of protein-based diagnosis. By learning from the desired and undesired features of existing techniques, we designed the blueprint of the next-generation biomolecule enrichment technique, which should ideally be universally applicable to all kinds of biomolecules and be capable of specifically enriching only the target biomolecules among the background biomolecules by billion-fold rapidly.

Electrokinetic concentration is a promising candidate for the next-generation biomolecule enrichment technique, because of its simple architecture and ease of operation, high concentration speed, universal applicability, and the rich physics of the system that may enable the development of new functionalities. We defined a technical roadmap of engineering the primitive electrokinetic concentration technique toward the next-generation biomolecule enrichment technique. We start by deciphering the mechanism of electrokinetic concentration (Chapter 2), which is instrumental in the rational design and innovation of the system. We next developed specific enrichment of target biomolecules in the electrokinetic concentrator based on electrophoretic mobility-based separation and mobility engineering of affinity binders (Chapter 3). We went on to realize the billion-fold enrichment capability of electrokinetic concentrator by massive parallelization and hierarchical cascading of unit electrokinetic concentrators (Chapter 4). After that, we demonstrated the engineered electrokinetic concentrator as an integrated, self-contained platform for universal amplification-free molecular diagnostics (Chapter 5). Finally, we interfaced the engineered electrokinetic concentrator with standard analytics to enhance their analysis sensitivity and greatly simplify their workflows (Chapter 6). At the end of the thesis, we conclude this thesis and present our outlooks on the future directions (Chapter 7).

Thesis Supervisor: Jongyoon Han
Title: Professor of Electrical Engineering and Biological Engineering

## Acknowledgments

I have been very fortunate to be surrounded by many great mentors and friends during the course of my graduate studies. This dissertation would not have been possible without their support and guidance.

First of all, I would like to thank my thesis advisor Prof. Jongyoon Han for being a great advisor. Prof. Han is not only an insightful and passionate scientist that inspires me to make all my research achievements, but also my role model as a teacher and educator. I would also like to thank my other thesis committee members, Prof. Dennis Freeman and Prof. Rohit Karnik, for their constructive comments and constant encouragement.

I am grateful for my fellow group members of the Han Group: Sung Hee Ko, Bumjoo Kim, Aniruddh Sarkar, Minseok Kim, Hyunryul Ryu, Lidan Wu, Siwon Choi, Taehong Kwon, David Collins, Chenhui Peng, Dhiraj Sarkar, Junghyo Yoon, Hyungkook Jeon, Hyukjin Kwon, Chia-Chen Yu, Matthew Flavin, Kyungyong Choi, Alex Barksdale, Eric Wynne, Kerwin Kwek, Yin Lu, Bee Luan Khoo, Aoli Xiong, Ching Ann Tee, Smitha Thamarath Surendran, Roh Jun Toh, Menglin Shang, and Xiwei Huang.

I would also like to thank my great collaborators from many institutions: Roby Bhattacharyya, Peijun Ma, Lorrie He, and Prof. Deborah Hung of Broad Institute; Xinghui Ye, and Prof. Zirui Li of Wenzhou University; Nathaniel Miller, and Prof. Ram Sasisekharan of MIT Biological Engineering; Annie Wang, Di Wu, and Prof. William Hancock of Northeastern University; Dr. Paul Barone of MIT Center for Biomedical Innovation; Prof. Lihong Liu of Southern Medical University of China; Yechang Guo, Yaoping Liu, and Prof. Wei Wang of Peking University.

I would like to acknowledge the Siebel Scholarship for the financial support.

Finally, I would like to express my deepest gratitude to my family for their unconditional love and support. Above all, I would like to thank my wife, Chenyu Wang, for her understanding, support, encouragement, and love. I would like to dedicate this dissertation to her.

# Table of Contents

## Table of Figures (Main Text)

# Chapter 1 Introduction

As stated by the Central Dogma of Biology (Fig. 1-1), the genetic information is encoded in DNA, which is transcribed to RNA, then RNA is translated to proteins. The proteins are essentially the molecular machines that carry out the majority of the tasks in cells, and they are also the regulators of *in vivo* biochemical reactions. All these biomolecular activities form the basis of biological phenotypes. The information flow is not only true for the human body, but also holds for most human-infecting agents, such as bacteria and viruses. The biofluids of human body, such as serum, urine, sweat, can be considered "biomolecule cocktails" of different recipes. They serve as a snapshot of the human body, which may potentially enable us to diagnose diseases rapidly and minimally invasively.

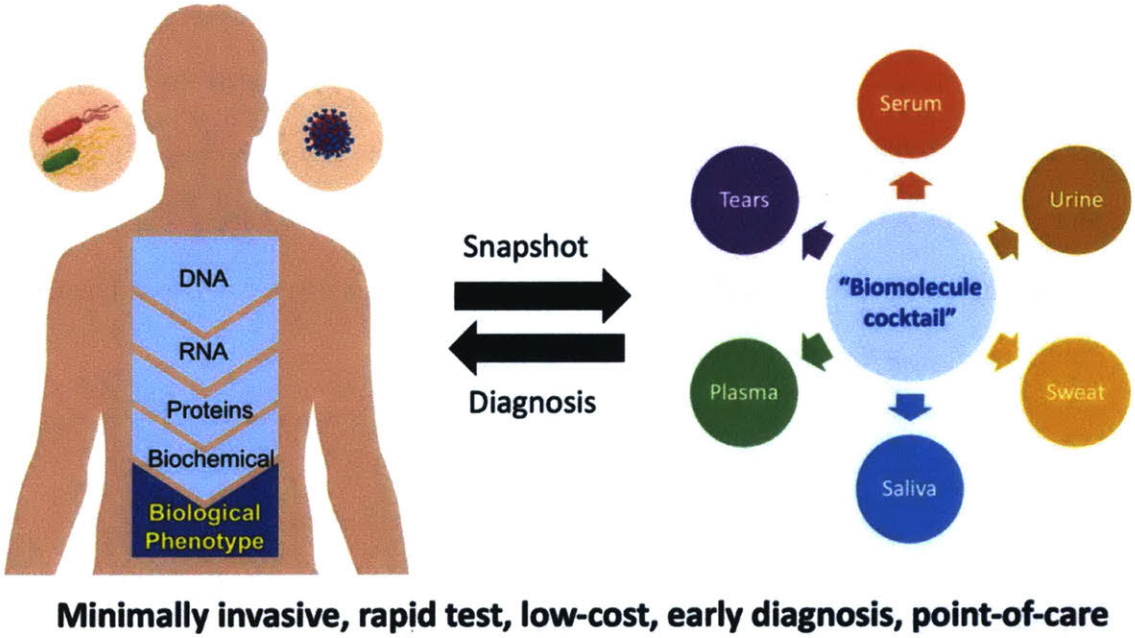


**Figure 1-1** Importance and advantages of molecular diagnostics.

The composition of biofluids is highly complicated. In this thesis, we are primarily interested in nucleic acids and proteins (in comparison to small-molecule biochemicals), because they have the most fundamental implications in biology. We will take one of the most studied and the most challenging biofluids, the blood plasma, as an example (Fig. 1-2). The plasma is a rich and diverse library of proteins with a total protein concentration of about 100 mg/ml. However, the biomolecules of interest have much lower abundance. For example, proteins derived from bacteria and viruses in plasma are typically in the range of aM to fM ($10^{-14}$ to $10^{-11}$ mg/ml), which is up to 16 orders of magnitude lower than that of the background proteins. Endogenous proteins, such as hormones and interleukins, are typically in the range of pM to nM ($10^{-8}$ to $10^{-5}$ mg/ml), which is up to 10 orders of magnitude lower than that of the background proteins. While the total cell-free DNAs in plasma is about $10^{-4}$ mg/ml, DNAs of specific sequences have much lower abundance, which are typically in the range of aM to fM (<1000 copies/μL). To sum up, the very low abundance of target biomolecules and very high abundance of background biomolecules make it highly challenging to analyze biomolecules in biofluids, because of the extremely low signal-to-noise ratio.

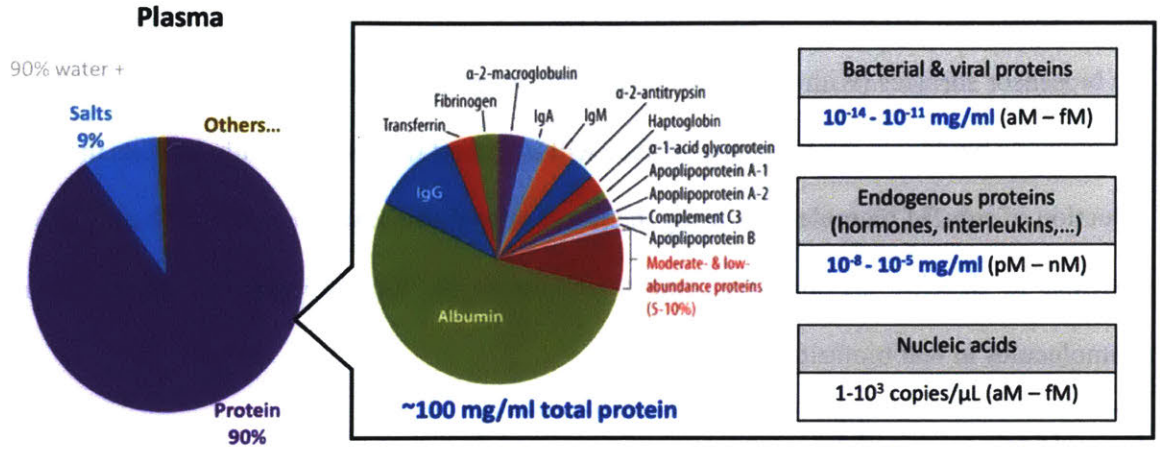


**Figure 1-2** The abundance of biomolecules of interest in human blood plasma [1]. Part of the figure is reproduced from ref. [2] with the permission of Elsevier.

To detect low-abundance target biomolecules among high-abundance background biomolecules, there are generally two strategies: sensor enhancement and signal enhancement. Benefitting from the great advancements of the micro/nanofabrication technology, various highly sensitive micro/nanoscale biosensors have been developed by exploiting the unique phenomena and properties at the micro/nanoscale. The most sensitive micro/nanoscale biosensors are represented by cantilever biosensors [3], nanochannel biosensors [4], graphene field-effect-transistor (FET) biosensors [5], and $MoS_2$ FET biosensors [6] (Fig. 1-3). They typically have high "intrinsic sensitivities", which detect signals even upon the binding of single-digit target biomolecules onto the biosensors. However, their "actual sensitivity" typically does not go beyond the fM-level, which is fundamentally limited by mass transport. In a typical sample volume of 1 μL for micro/nanoscale sensors, there are only 600 target

biomolecules at 1 fM and <1 target biomolecule at 1 aM, which take >10 hours to diffuse to the biosensor surfaces (with extremely small surface areas) [7]. The low likelihood of a target biomolecule binding to the biosensor surface within a short time theoretically inhibits the rapid detection of sub-fM biomolecules using the novel micro/nanoscale biosensors. Therefore, it is essential to develop signal enhancement techniques for the detection of low-abundance biomolecules in real biofluids.

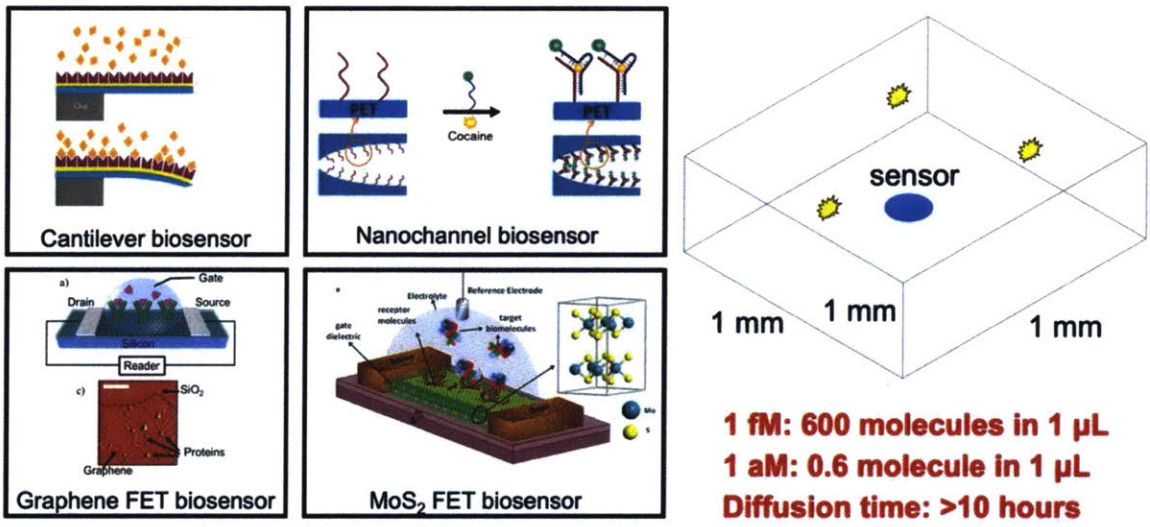


**Figure 1-3** Novel micro/nanoscale biosensors using (a) a cantilever [3], (b) a nanochannel [4], (c) a graphene FET [5], and (d) a MoS2 FET [6]. (e) The fundamental slow mass transport that limits the actual sensitivity of novel biosensors. Figures are reproduced with the permissions of Elsevier, American Chemical Society, and Springer Nature.

In this chapter, we will first introduce the current status of biomolecule enrichment techniques, followed by our perspectives on the next-generation biomolecule enrichment

technique. Finally, we will identify a potential technique that may align to our perspectives, and define a technical roadmap toward our perspectives. The following chapters are organized based on the technical roadmap we define.

## 1.1 Current status of DNA enrichment techniques

Currently, DNA enrichment mainly relies on the revolutionary polymerase chain reaction (PCR), which can amplify the target sequence from as low as a single copy to billions of copies. PCR is extremely powerful but not perfect. It suffers from many inherent issues to different degrees, such as the sensitivity, specificity, and fidelity of amplification, cross-contamination, the instability of polymerases and their susceptibility to inhibitors, and poor multiplex-ability, which stem from the nature of chemical amplifications. It also suffers from practical issues, such as high cost, the requirement of thermal cycling instruments, and the dependence on well-trained personnel to obtain good and reproducible results. These limitations make it difficult to implement PCR for resource-limited settings and point-of-care applications. In recent years, a number of isothermal amplification techniques have been developed (Fig. 1-5), such as loop-mediated isothermal amplification (LAMP) [8], recombinase polymerase amplification (RPA) [9], and helicase dependent amplification (HDA) [10]. These techniques avoid the use of thermal cycling, but still suffer from inherent issues of chemical amplification, such as difficult primer design and poor multiplex-ability, making it difficult to implement these techniques in many applications. Therefore, novel DNA enrichment techniques matching the performance of PCR yet overcoming the aforementioned issues, would be of great significance for developing field-deployable DNA-based molecular diagnostics.

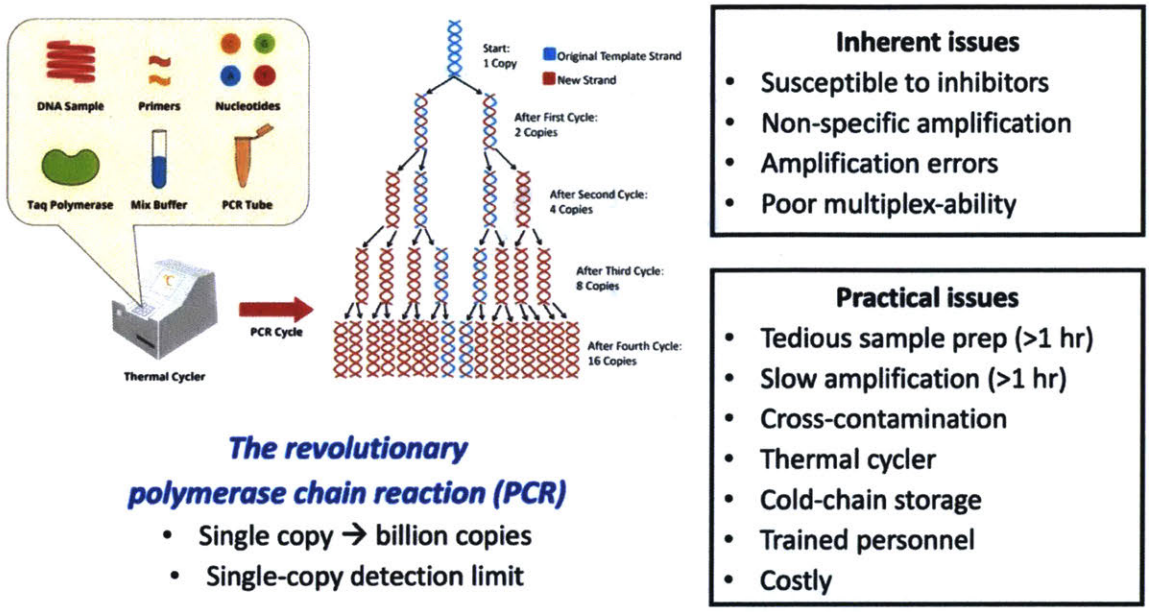


**Figure 1-4** The principle and limitations of PCR [11], [12].

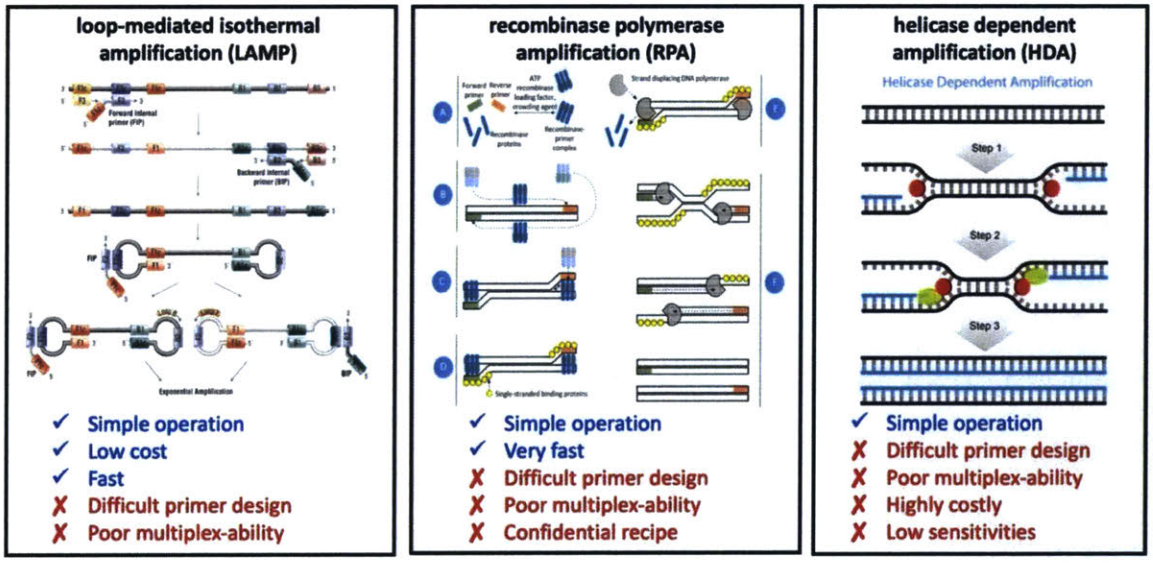


**Figure 1-5** Examples of isothermal amplification techniques and their limitations [9], [13], [14]. Figures are reproduced with the permission of Elsevier.

## 1.2 Current status of protein enrichment techniques

Compared to the spectacular developments of DNA analysis, protein analysis is severely lagging behind. The gold standard protein detection technique, the enzyme-linked immunosorbent assay (ELISA), could only routinely detect ~pM concentrations at the lowest, far above the sub-fM concentrations of many protein biomarkers [7]. ELISA relies on enzymatic signal amplification processes (*e.g.* horseradish peroxidase-catalyzed colorimetric signal generation) following the occurrence of target–probe binding, which remains limited by the slow mass transport and weak binding kinetics at ultralow target concentrations. Therefore, target protein enrichment is essential for the detection of ultralow-abundance proteins.

Currently, effective protein enrichment techniques are still lacking, especially for real, complex biofluids. There are no chemical amplification techniques like PCR that can replicate proteins. According to mass conservation, in the absence of chemical protein amplification techniques, the only available approach for protein enrichment is physically concentrating them from a large volume to a small volume. Conventional macroscopic methods, such as immunoprecipitation and affinity chromatography, can only achieve <100-fold concentration of target proteins. In the past two decades, a number of microfluidic techniques have been developed for protein enrichment, such as isotachophoresis [15], field amplified sample stacking [16], [17], electric field gradient focusing [18], [19], and temperature gradient focusing [20], [21]. However, existing microfluidic protein enrichment techniques can only achieve $<10^6$-fold concentration of proteins in an hour, which is far below the performance of

PCR and cannot meet the requirement of detecting the lowest abundance proteins (aM - fM). Moreover, unlike PCR that specifically amplifies the target sequence, the aforementioned microfluidic protein enrichment techniques are physical methods not capable of selectively enriching the target protein v.s. the background proteins. The non-selective concentration of the high-abundance background proteins often results in the precipitation of proteins and degradation or even failure of the devices, preventing the use of these techniques for real, complex biofluids.

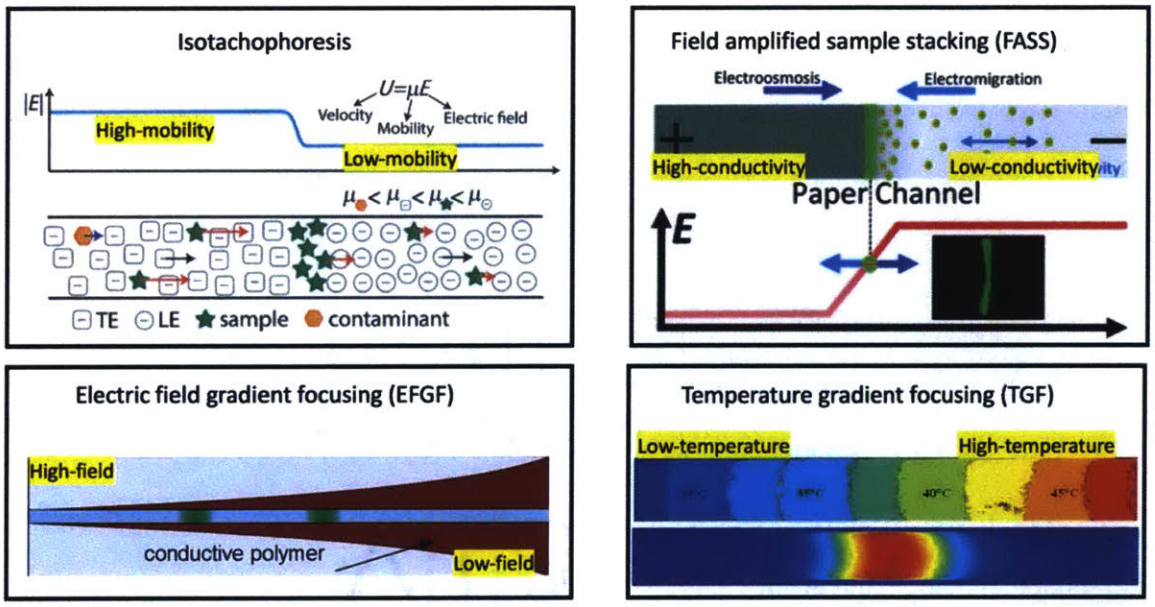


**Figure 1-6** Examples of protein concentration techniques [17]–[21]. Figures are reproduced with the permission of Royal Society of Chemistry.

## 1.3 The blueprint of the next-generation biomolecule enrichment technique

We take the most widely used biomolecule enrichment technique, the PCR, as a model to design the next-generation biomolecule enrichment technique, by learning what features are needed and what features are to be avoided. As shown in Fig. 1-7, in PCR, a specific target sequence is amplified among the pool of DNAs. This is realized by the specific recognition of the target sequence by complementary DNAs (cDNAs) (more specifically, a pair of DNA primers). After that, the cDNA-bound target DNA is specifically amplified by billion-fold via exponential replication of the template using biochemical reactions. Because of the distinct biochemical natures of DNA and protein, PCR only works for DNA. The next-generation biomolecule enrichment technique would ideally be universal for both DNA and protein, yet capture the two most remarkable features of PCR: specific enrichment of the target biomolecule and billion-fold enrichment capability. In protein biochemistry, the analogy of cDNA used in DNA biochemistry is the complementary antibody of the target protein (Fig. 1-7). Therefore, the core merit of the next-generation biomolecule enrichment technique is the capability of specifically enriching the Ab-bound target protein among the pool of background proteins and the cDNA-bound target DNA among the pool of background DNAs by billion-fold. Additionally, given the unavailability of protein amplification chemistry presently and the extreme difficulty in developing one, the next-generation biomolecule enrichment technique is expected to be a physical method, which is naturally immune to the various issues stemming from the nature of chemical amplifications, such as amplification specificity and fidelity, enzyme instability and susceptibility to inhibitors, and poor multiplex-ability. In summary, the next-generation biomolecule enrichment technique should (1) be universally

applicable to DNA and protein, (2) specifically enrich only the target biomolecules, (3) have billion-fold enrichment capability, and (4) be free from inherent issues of chemical amplification.

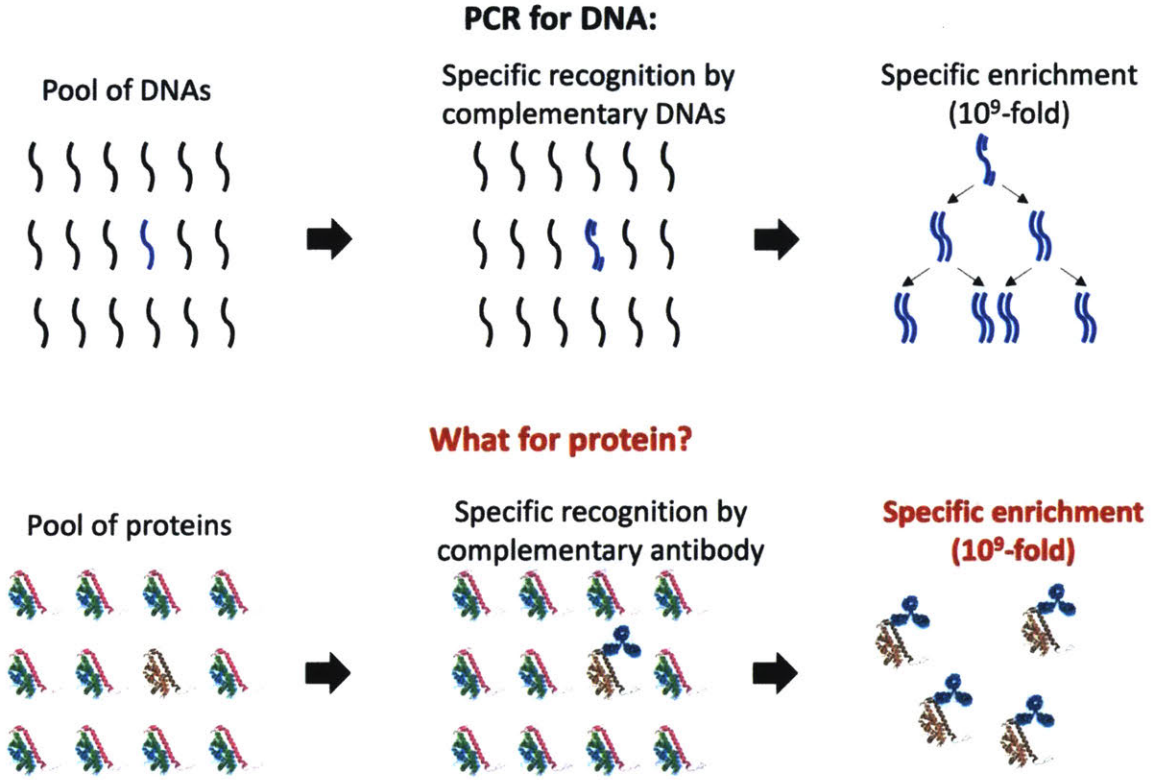


**Figure 1-7** PCR as a model for designing the next-generation biomolecule enrichment technique.

## 1.4 Electrokinetic concentration: a promising candidate for the next-generation biomolecule enrichment technique

Electrokinetic concentration is currently one of the most effective techniques for protein (and DNA) enrichment, with enrichment speeds of $10^3$- to $10^4$-fold in ~10 min and maximum enrichment factors of ~$10^6$ in ~3 hours achieved in clean buffers [22]. The structure of the electrokinetic concentrator can be as simple as a single straight microfluidic channel with a cation-selective membrane patterned at the bottom of the channel [23], as shown in Fig. 1-8(a). Upon the application of a DC voltage, the biomolecules are electrokinetically driven in the microfluidic channel and subsequently continuously concentrate near the cation-selective Nafion membrane [24], as shown in Fig. 1-8(b). The mechanism of electrokinetic concentration is illustrated in Fig. 1-8(c) and qualitatively explained as follows: (1) The selective transport of cations through the cation-selective membrane induces an ion depletion zone near the membrane, in which the ion concentration decreases to near zero and the corresponding electric field is significantly amplified (to main the continuity of the electric current along the channel). (2) The biomolecules (mostly negatively charged under physiological conditions) enter the microfluidic channel with the fluid flow (i.e. electroosmosis), which is counteracted by the electrostatic force (i.e. electrophoresis). (3) As the biomolecules approach the amplified electric field (electric force barrier), the electrophoresis gradually increases until completely canceling out the electroosmosis, leading to the electrokinetic trapping of the biomolecules. (4) The continuous injection of biomolecules and subsequent electrokinetic trapping of biomolecules causes the accumulation of biomolecules in the electric force barrier, which is the electrokinetic concentration effect.

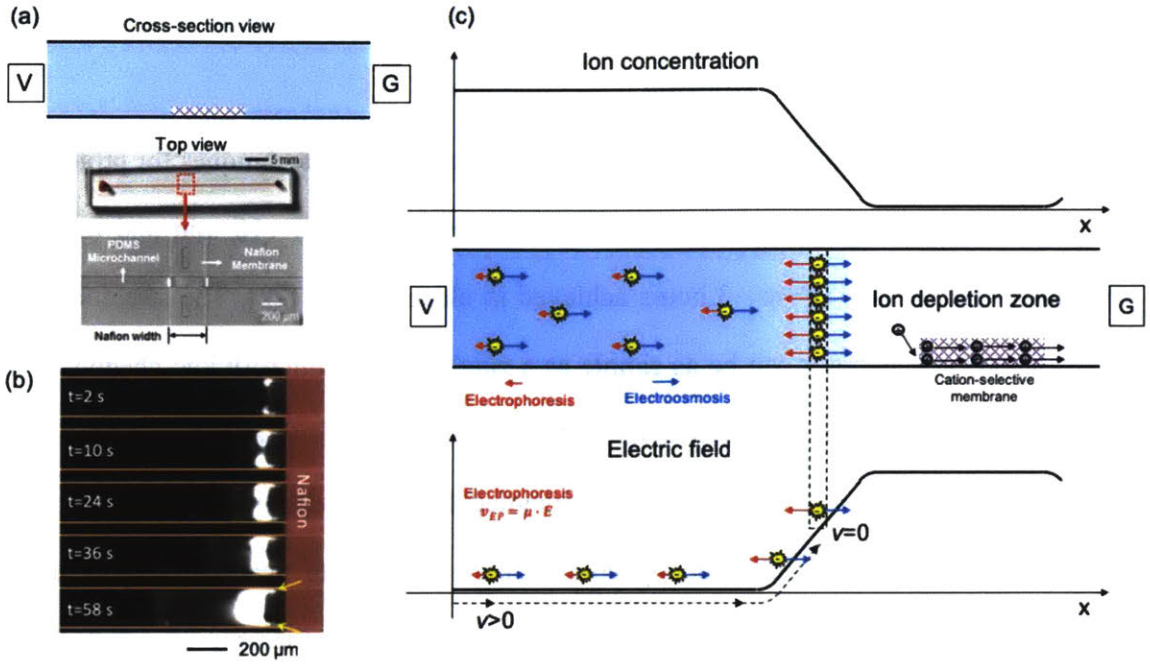


**Figure 1-8** The schematic and principle of electrokinetic concentration. (a) Schematic and photos of the electrokinetic concentrator [23]. (b) Temporal evolution of bovine serum albumin (BSA) concentration in the electrokinetic concentrator [24]. (c) The mechanism of electrokinetic concentration. Figures are reproduced with the permissions of Royal Society of Chemistry and American Institute of Physics.

We deem the electrokinetic concentration technique a promising candidate for the next-generation biomolecule enrichment technique for the following reasons: (1) Electrokinetic concentration is so far one of the highest-performance biomolecule enrichment techniques (in terms of speed and maximum enrichment factor). (2) Electrokinetic concentration is based on the electric charges universally carried by biomolecules and not sensitive to the biochemical

identities of biomolecules, making it a universally applicable method for different types of biomolecules. (3) The architecture of electrokinetic concentration devices is simple as previously mentioned, and the operation of the devices does not require well-tuned multi-electrolyte systems and pH gradients, which are critical in many other biomolecule enrichment techniques. The ease of fabrication and operation may potentially make the technique more robust and more deliverable to end users. (4) Electrokinetic concentration is a multi-physics, non-linear process involving fluid mechanics, charged species transport, and electric field, which offers many degrees of freedom for engineering. Further investigation and engineering of the electrokinetic concentration system may lead to new functionalities and new modalities that are needed in the next-generation biomolecule enrichment technique.

## 1.5 The technical roadmap toward the next-generation biomolecule enrichment technique

While electrokinetic concentration is promising for developing the next-generation biomolecule enrichment technique, it is still its infancy. Firstly, there is minimal quantitative understanding of the mechanism of electrokinetic concentration, causing significant controversies in the literature regarding the behaviors of electrokinetic concentration and also leaving the rational design and optimization of the device infeasible. Secondly, the electrokinetic concentrator enriches all negatively charged biomolecules with no specificity for target biomolecules. The co-concentration of background biomolecules not only causes significant noises for target detection, but also often causes the rapid degradation or even

failure of the device. Finally, the biomolecule enrichment performance of electrokinetic concentration (<$10^6$-fold in 3 hours) is still far below that of PCR (~$10^9$-fold in 1 hour), which must be dramatically enhanced to meet the requirements of the next-generation biomolecule enrichment technique.

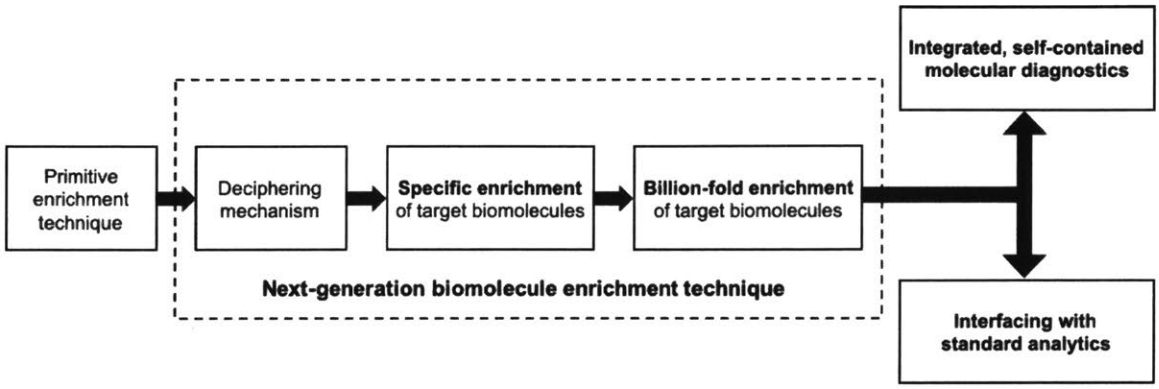


**Figure 1-9** The technical roadmap of developing the next-generation biomolecule enrichment technique from the primitive electrokinetic concentration technique.

In this thesis, we will engineer the primitive electrokinetic concentration technique into the next-generation biomolecule enrichment technique we previously defined, and demonstrate the applications of the engineered electrokinetic concentration technique in real-world molecular diagnostics. To achieve this goal, we designed a technical roadmap as shown in Fig. 1-9. We will start by deciphering the mechanism of electrokinetic concentration by combining numerical simulation, theoretical modeling, and experimental validation (Chapter 2), which is instrumental in the rational design of the device and the development of new functionalities. Next, we will realize the specific enrichment of only the target biomolecules and simultaneous removal of background biomolecules in the electrokinetic concentrator (Chapter 3). Then, we

will realize universally applicable billion-fold enrichment of biomolecules using the electrokinetic concentrator via a hierarchical multi-stage architecture (Chapter 4). After that, we will demonstrate the use of the engineered electrokinetic concentrator (with specific enrichment and billion-fold enrichment capability) for universal amplification-free detection of ultralow-abundance DNA and protein biomarkers in real-world, clinical samples (Chapter 5). Finally, we will demonstrate the interfacing of the electrokinetic concentrator with well-established standard analytical techniques to improve their performance and simplify their workflows (Chapter 6). At the end of this thesis, we will conclude our work and present our outlooks on the future directions (Chapter 7).

# Chapter 2 Deciphering electrokinetic concentration

Note: This Chapter is a direct reproduction of a previously published peer-reviewed journal paper (Wei Ouyang, Xinghui Ye, Zirui Li, and Jongyoon Han, Nanoscale, 2018,10, 15187-15194) with the permission of Royal Society of Chemistry. Appendix 1 is the supplementary information of this article. Wei Ouyang, under the supervision of Jongyoon Han, developed the "electroneutrality limit" part of the analytical model, co-designed the studies to conduct by numerical simulation, and performed all the experimental validations; Zirui Li and his student Xinghui Ye developed the "electrokinetic limit" part of the analytical model, co-designed the studies to conduct by numerical simulation, and performed all the numerical simulations.

Over the past two decades, nano-electrokinetics in micro-nanofluidic systems has been unprecedentedly actively studied with the aid of the recent advancements in nanotechnology [25]. One of the most compelling nano-electrokinetic phenomena is the electrokinetic molecular concentration (EMC) effect at the micro-nanofluidic interface induced by the coupling of ion concentration polarization (ICP) and tangential electroosmotic flow (EOF), which enables over million-fold preconcentration of biomolecules for various biomedical applications [22]–[24], [26]–[32]. Despite the tremendous interests in ICP-based EMC [33], [34], researchers have been constantly reporting controversially different behaviors of ICP-based EMC ever since the conception of the system [23], [28], [35]–[39], such as the maximum concentration capacity and its dependence on system parameters, which remains an enigma so far owing to the minimal scientific understanding of the system. This is mainly hampered by

the high complexity of the system, which involves coupled nonlinear fluid flow, charged species transport, and dynamic evolution of electric field in multi-scale space spanning from sub-nanometers to centimeters. Although considerable progresses have been made towards the understanding of componential problems, such as ICP [40]–[45], nonlinear electrokinetic flow [46]–[49], micro-nanofluidic ion transport [25], [50], the fully coupled mechanism of ICP-based EMC is still rarely known. Shen *et al.* [37] and Jia *et al.* [38], [39] demonstrated numerical simulation as a viable approach for the studying of ICP-based EMC, which yet only provided numerical descriptions of the system under specific conditions with limited implications in the comprehensive fundamental mechanism of the system.

In this chapter, we report a series of experimental and theoretical new findings that decipher the mechanism of ICP-based EMC. We demonstrate the first elucidation of two separate operating regimes of ICP-based EMC, which provided the key for us to establishing the first theoretical model that analytically yet concisely describes this highly complicated nonlinear system. We further unveil the dramatically different scaling behaviors of ICP-based EMC in the two regimes both experimentally and theoretically, thereby clarifying the scientific controversies revolving around ICP-based EMC. These insightful findings significantly advance the scientific understanding of ICP-based EMC, while setting solid foundations for the rational design and optimization of ICP-based EMC devices for various applications.

## 2.1 The numerical model and results of numerical simulation

As introduced in Chapter 1, a simple architecture of the EMC device consists of a single straight microfluidic channel and a cation-selective membrane/nanochannel array patterned at

the bottom of the channel. In this two-terminal architecture, the continuous injection of biomolecules and selective ion transport are induced by the same pair of electrodes, so the conditions of the two phenomena are not independent. In this chapter, as shown in Fig. 2-1, in order to obtain a comprehensive fundamental understanding of the mechanism, we (partially) decouple the conditions of the continuous injection and selective ion transport by introducing an additional electrical terminal at the cation-selective membrane, which enables the free tuning of the electric field that drives the cation transport through the membrane/nanochannel array. Furthermore, in order to reduce the computation load of numerical simulation, a pair of membranes/nanochannel arrays and additional electrical terminals are symmetrically introduced at the two sides of the microchannel. Because the voltages of the additional terminals at the pairing membranes/nanochannel arrays are always kept the same under the symmetrical condition, this architecture is still considered three-terminal.

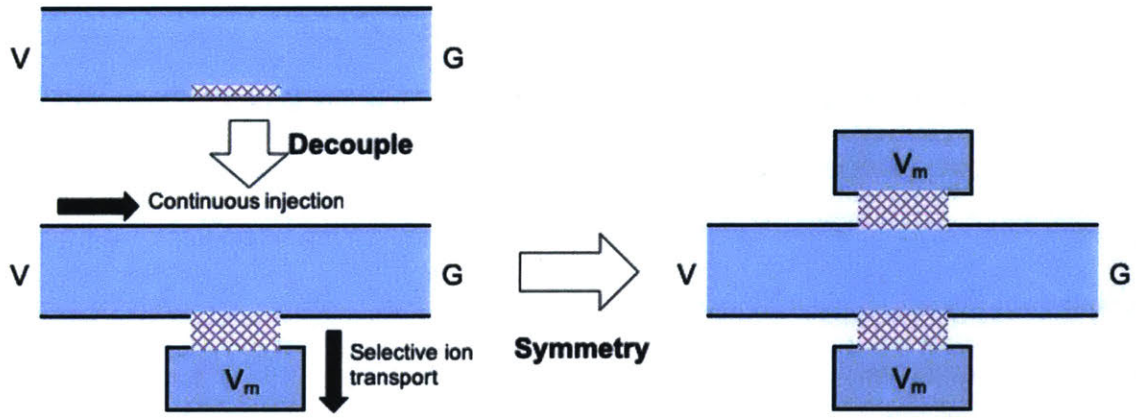


**Figure 2-1** Converting the simple two-terminal EMC device to the three-terminal EMC device for fundamental mechanism studies.

Fig. 2-2(a) shows the photo and schematic of the device. The device consists of a central microchannel in parallel with two side microchannels (all 2 cm long, 100 μm wide and 15 μm deep), which are interconnected by two nanochannel arrays (250 μm long and 400 μm wide). The microchannels were fabricated by polydimethylsiloxane (PDMS) soft lithography, and the nanochannel arrays were patterned on a glass slide using Nafion resin (equivalent nanochannel size: ~4 nm) [51], after which the PDMS and glass slide were bonded by plasma treatment [23]. All the channel walls are negatively charged. The channels are filled with buffer solutions (potassium chloride (KCl) in this study), and the analyte (negatively charged) sample is loaded into the inlet (left reservoir) of the central microchannel. The inlet and outlet of the central microchannel are biased to electric potentials of $V_H$ and $V_L$ ($V_H > V_L$), respectively, while the four reservoirs of the side microchannels are grounded ($V_G$=0 V). The cross-nanochannel voltage $V_{cn}$, defined as $V_{cn}=(V_H+V_L)/2-V_G$, is set to be positive. Under this configuration, cations are selectively transported through the cation-selective nanochannels driven by the normal electric field $E_\perp$, leading to the formation of ion depletion in the central microchannel and ion enrichment in the side microchannels, i.e. the ICP phenomenon. Meanwhile, the tangential electric field $E_{//}$ generated by $V_H$ and $V_L$ induces a tangential electroosmotic flow (EOF) from the inlet towards the outlet of the microchannel, which carries the analyte into the microchannel. The negatively charged analyte is subsequently trapped at the front of the ion depletion zone, the detailed mechanism of which is revealed by numerical simulation using the two-dimensional model shown in Fig. 2-2(b) (see Experimental Section for details). As indicated by Fig. 2-2(c), significantly accelerated non-equilibrium EOFs are generated in the vicinity of the nanochannels due to the non-equilibrium space charge layers induced by ion

depletion [46], [47], [52], which gives rise to the strong vortical flows in the ion depletion zone as a result of the incompressibility of fluid. At the same time, the electric field is significantly amplified near the nanochannels (plotted in natural logarithm-scale) due to the low ion concentration thereof. Consequently, instead of following the streamlines into downstream, the analyte (negatively charged) is retarded by the strong tangential electric force in the ion depletion zone, and pushed towards the backflow of the vortices by the strong normal electric force in the vicinity of the nanochannels, which act jointly to prevent the analyte from moving downstream, resulting in the continuous trapping and concentration of the analyte, i.e. the EMC effect.

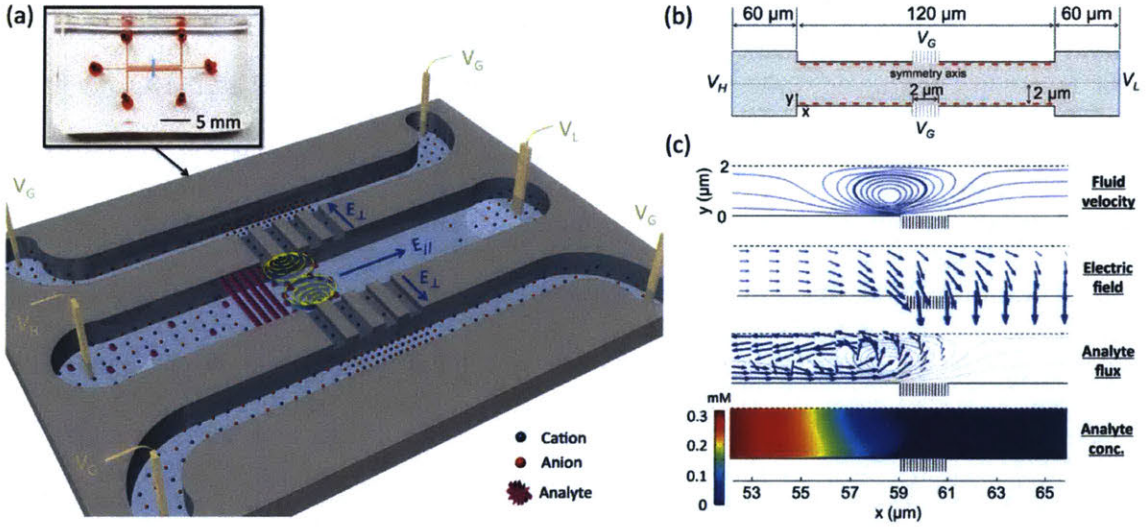


**Figure 2-2** Schematic of the device and the numerical model. (a) The photo and schematic of the ICP-based EMC device. The blue box in the photo indicates the location of the nanochannel arrays (Nafion membrane). (b) Schematic of the simulation model. (c) Simulated profiles of fluid velocity, electric field, analyte flux, and analyte concentration at the steady state. In the

simulation, $V_{HL}$=($V_H$ - $V_L$)=20$V_T$ ($V_T$=25.6 mV, the thermal voltage), and $V_{cn}$ was set to 30$V_T$. The initial concentration of the analyte is 0.1 nM. 1 mM KCl is used as the buffer. Given the symmetry of the system, only the lower half of the channel is plotted.

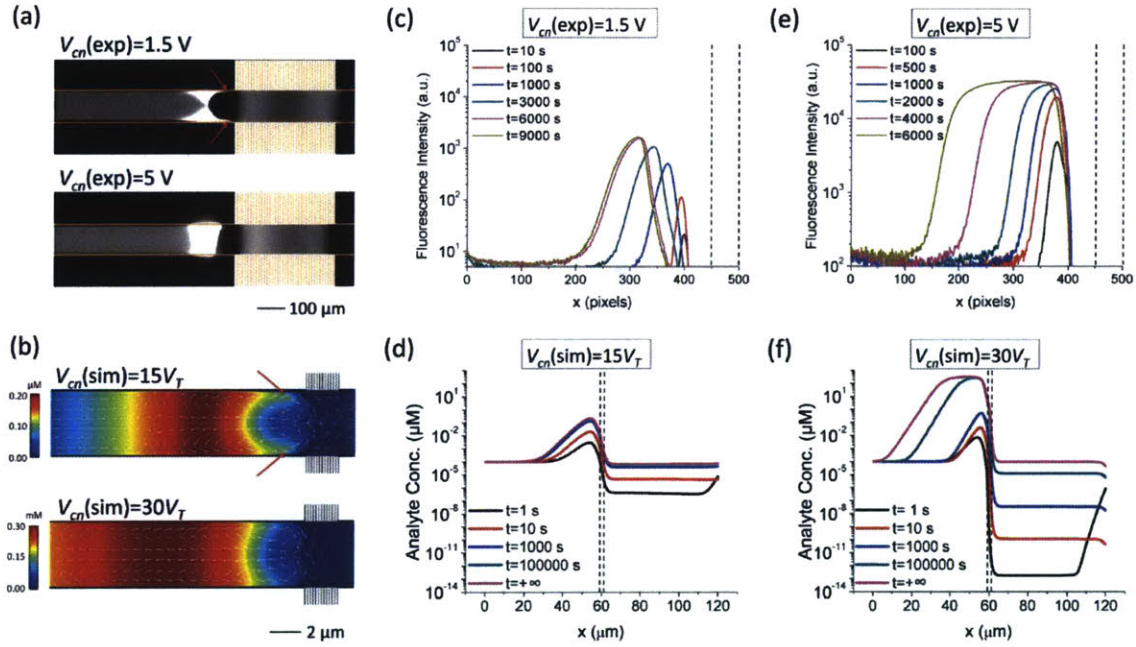


**Figure 2-3** Elucidation of the two separate operating regimes of ICP-based EMC. (a) Fluorescent images showing the concentration behaviors of 21mer single-stranded DNA (ssDNA) at $V_{cn}$=1.5 V (t=100 s) and $V_{cn}$=5 V (t=10 s). In the experiments, the initial analyte concentration is 1 μM, and the buffer is 10 mM KCl. $V_{HL}$ was set to 10 V. (b) Simulation results showing the concentration behaviors of the default analyte particle (see Methods for details) at $V_{cn}$=15$V_T$ and $V_{cn}$=30$V_T$ ($V_T$=25.6 mV, the thermal voltage). The arrows show the flux densities of the analyte, the lengths of which are plotted in natural logarithm-scale. In the simulation, the initial analyte concentration is 0.1 nM, and the buffer is 1 mM KCl. $V_{HL}$ was

set to $20V_T$. (c) Experimental temporal evolution of the fluorescence intensity of the ssDNA at $V_{cn}$=1.5 V. (d) Simulated temporal evolution of the concentration of the analyte at $V_{cn}=15V_T$. (e) Experimental temporal evolution of the fluorescence intensity of the ssDNA at $V_{cn}$=5 V. (f) Simulated temporal evolution of the concentration of the analyte at $V_{cn}=30V_T$. The double dash lines indicate the x-coordinates of the nanochannel arrays.

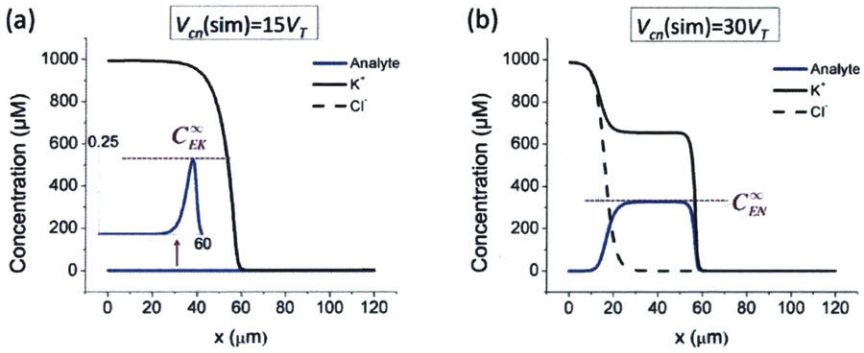


**Figure 2-4** Simulated steady-state concentrations of the buffer ions and the analyte at (1) $V_{cn}=15V_T$ and (1) $V_{cn}=30V_T$. $V_{HL}$ was set to $20V_T$ ($V_T$=25.6 mV, the thermal voltage).

## 2.2 Experimental and numerical observation of the electrokinetic limit and electroneutrality limit

The trapping of the analyte is directly induced by the vortical flows and amplified electric field in the ion depletion zone, which is strongly dependent on $V_{cn}$. The higher $V_{cn}$ is, the stronger the ion depletion effect is. To investigate the concentration behaviors, we experimentally measured the temporal evolution of the concentration of a fluorescent 21mer single-stranded

DNA (ssDNA) under different $V_{cn}$'s, and simulated the process with an analyte particle of similar electrophoretic mobility. As indicated by Figs. 2-3(a-b), at relatively low $V_{cn}$'s, due to the relatively weak electric force, the analyte "protrudes" (annotated with red arrows) into the depletion zone near the channel walls following the fast non-equilibrium EOFs, leading to the non-negligible fluxes of the analyte (shown in white arrows) that "leak" into downstream [24]. On the other hand, at relatively high $V_{cn}$'s, the analyte is almost completely trapped at the front of the ion depletion zone, without "protrusions" into the depletion zone formed and with negligible "leakage" into the downstream. Depending on the trapping efficiency, the concentration behaviors of the analyte are distinct. As shown in Figs. 2-3(c-d), at relatively low $V_{cn}$'s, the analyte concentration increases with a bell-shaped profile until the steady state is reached. In contrast, at relatively high $V_{cn}$'s, the peak concentration increases much faster than that at low $V_{cn}$'s and reaches a maximum concentration, after which the peak starts to broaden to upstream until a wide plateau is formed at the steady state (Fig. 2-3(e-f)). From the simulated steady-state concentration profiles of the buffer ions and analyte at different $V_{cn}$'s shown in Fig. 2-4, we can identify two separate limits for the maximum concentration of the analyte achievable by EMC. When the analyte is not effectively trapped (Fig. 2-4(a)), the maximum concentration of the analyte is significantly smaller than those of the buffer ions, which is determined by the balancing between the convective, electrophoretic, and diffusive fluxes of the analyte. Therefore, this limiting concentration is named the electrokinetic (EK) limit ( $C_{EK}^{\infty}$ ). On the other hand, when the analyte is effectively trapped (Fig. 2-4(b)), the negatively charged analyte will eventually become one of the majority charge carriers as it

continuously concentrates, while the anion concentration correspondingly decreases to maintain electroneutrality. When the anion concentration decreases to zero and the cations are neutralized by the analyte solely, the analyte concentration can no longer increase. Afterwards, the concentration process can only proceed by forming a widening plateau with a fixed concentration. In this sense, this limiting concentration is named the electroneutrality (EN) limit ( $C_{EN}^{\infty}$ ).

## 2.3 Analytical formulation of the electrokinetic limit and electroneutrality limit

We next theoretically formulate the EK and EN limits. The governing equations of the system are the Navier-Stokes, Nernst-Planck, and Poisson equations that describes the incompressible fluid flow, charged species transport, and electric potential [53]–[55], respectively:

$$\rho(\partial \mathbf{U}/\partial t + (\mathbf{U}\cdot\nabla)\mathbf{U}) = -\nabla P + \eta\nabla\cdot\nabla\mathbf{U} - \rho_e\nabla\Phi, \tag{2.1}$$

$$\nabla\cdot\mathbf{U} = 0, \tag{2.2}$$

$$\partial C_i/\partial t = -\nabla\cdot\mathbf{J}_i, \tag{2.3}$$

$$\mathbf{J}_i = -D_i\nabla C_i - D_i(Z_i e_0/kT)C_i\nabla\Phi + \mathbf{U}C_i, \tag{2.4}$$

$$-\nabla\cdot(\varepsilon\nabla\Phi) = \rho_e, \tag{2.5}$$

where $\mathbf{U}$, $P$, and $\Phi$ are the velocity of the fluid, the pressure, and the electric potential, respectively; $\mathbf{E} = -\nabla\Phi$ is the electric field; $\rho$, $\eta$, and $\varepsilon$ are the mass density, dynamic viscosity, and the permittivity of the solution, respectively; $k$, $T$, and $e_0$ are the Boltzmann constant, the absolute temperature, and the elementary charge, respectively; $C_i$ and $\mathbf{J}_i$ are the concentration and flux density of species $i$, respectively. For convenience, we use $i$=1 for the cation, $i$=2 for

the anion, and $i$=3 for the analyte. $D_i$ and $Z_i$ are the diffusion coefficient and valence of species $i$, based on which the electrophoretic mobility $\mu_i$ can be calculated using the Einstein relation ($\mu_i = (e_0 / kT)|Z_i D_i|$) [56]. The space charge density is given by $\rho_e = e_0 \sum_{i=1}^{3} Z_i C_i$. We further define $a = D_2 / D_3$, $b = Z_3 / Z_2$, and $b/a = \mu_3 / \mu_2$ for the forthcoming analyses. We will use the superscript "0" to denote the initial value, and "$\infty$" to denote the steady state.

While this nonlinear equation set is notoriously challenging to solve, elucidation of the two separate operating regimes enables us to establish the approximate one-dimensional analytical solutions. At the EK limit where $C_1^\infty \approx C_2^\infty \gg C_3^\infty$, the concentrating of the analyte does not alter the properties of the system. This fact permits us to approximately solve the parameters of the system first without involving the analyte, based on which the distribution of the analyte can be determined. More specifically, we formulated the EK limit in a four-stepwise procedure (see Section A1.1 of the Appendix 1): (a) the distribution of buffer ions ($C_1^\infty(x)$ and $C_2^\infty(x)$) can be solved for symmetric binary electrolytes ($D_1 = D_2$, $Z_1 = -Z_2$, $C_1^0 = C_2^0$, e.g. KCl) by combining Eq. 2.4 for $i$=1 and $i$=2, with the approximation of $J_2^\infty \approx 0$ (considering $J_1^\infty \gg J_2^\infty$); (b) With $C_2^\infty(x)$ known, the electric field is solved from Eq. 2.4 for $i$=2; (c) With the electric field known, the distribution of the analyte ($C_3^\infty(x)$) is solved from Eq. 2.4 for $i$=3; (d) With $C_3^\infty(x)$ known, the peak concentration ($C_{EK}^\infty = C_3^\infty(\max)$) can be obtained by finding the peak position with $dC_3^\infty(x)/dx = 0$. Accordingly, the system at the EK limit is solved as follows,

$$C_1^{\infty}(x) \approx C_2^{\infty}(x) \approx \left(1-\Psi e^{\mathrm{Pe}\cdot\frac{x}{L/2}}\right)\cdot C_2^0,\ (x<L/2) \tag{2.6}$$

$$C_3^{\infty}(x) \approx \left(\frac{1-\Psi e^{\mathrm{Pe}\cdot\frac{x}{L/2}}}{1-\Psi}\right)\cdot e^{(1-\frac{b}{a})\mathrm{Pe}\frac{x}{L/2}}\cdot C_3^0,\ (x<L/2) \tag{2.7}$$

$$C_{EK}^{\infty} \approx a^{-a}b^{b}(a-b)^{(a-b)}\cdot e^{(a-b)\cdot\mathrm{Pe}}\cdot C_3^0, \tag{2.8}$$

where $\Psi=(1-\frac{C_2^d}{C_2^0})e^{-\mathrm{Pe}}$ and $\mathrm{Pe}=\frac{\bar{u}(L/2)}{D_2}$, with $C_2^d$ being the downstream anion concentration after ion depletion ($C_2^d \ll C_2^0$), Pe being the Péclet number of the system, $\bar{u}$ being the average x-directional fluid velocity, and $L$ being the length of the central microchannel (nanochannel arrays are at $x=L/2$).

At the EN limit, the key constraint is the electroneutrality condition ($Z_1C_1^{\infty}+Z_3C_3^{\infty}\approx 0$, $C_2^{\infty}\approx 0$) at the concentration plateau of the analyte. Based on the electroneutrality condition and $J_i^{\infty}(\mathrm{inlet})=J_i^{\infty}(\mathrm{plateau})$, $dC_i^{\infty}(x)/dx=0$ at the inlet and concentration plateau, we obtained the EN limit for symmetric binary electrolytes as the following (see Section A1.2 of the Appendix 1),

$$C_{EN}^{\infty} \approx \frac{2}{a+b}\cdot C_1^0. \tag{2.9}$$

Eq. 2.8 and Eq. 2.9 clearly illustrate the different natures of the two regimes: the EK limit is determined by electrokinetics of the system (represented by the Péclet number Pe), while the EN limit is bound by the concentration of the counter-ion ($C_1^0$) that allows the sustaining of the electroneutrality.

The central metric of ICP-based EMC is the concentration factor (CF) of the analyte $\beta^{\infty}$, which is defined as the ratio of the peak concentration to the initial concentration, i.e. $\beta^{\infty} = C_3^{\infty}(\max) / C_3^0$. According to Eq. 2.8 and Eq. 2.9, the CF can be expressed as,

$$\beta^{\infty} \approx \begin{cases} e^{(a-b)\mathrm{Pe}}, \text{(EK)} \\ \dfrac{2}{a+b} \cdot \dfrac{C_1^0}{C_3^0}, \text{(EN)} \end{cases}, \tag{2.10}$$

in which the EK limit was simplified by leaving out the term $a^{-a}b^{b}(a-b)^{(a-b)}$, because the order of magnitude of $\beta_{EK}^{\infty}$ is mainly determined by the latter term $e^{(a-b)\mathrm{Pe}}$ (see Section A1.1 of Appendix 1 for values of this term in simulation). According to Eq. 2.10, the theoretical EN limit is only determined by the net charges, diffusion coefficients, and concentrations of the buffer ions and analyte, which allows one to predict the CFs of actual experimental systems in the EN-limited regime without knowing the dimension, surface charge densities, and other physical parameters. On the other hand, the derivation of the theoretical EK limit is much more complicated, which assumes perfect cation-selectivity of the nanochannels and adopts other simplifications (see Section A1.1 of the Appendix 1). Therefore, the value of the theoretical EK limit does not directly correspond to that in actual experimental systems, but it enables one to extract the key scaling laws obeyed in actual experimental systems. The CFs of ICP-based EMC devices range sparsely from O(1) to O($10^7$) in the literature [33], which has not been explainable due to the poor understanding of the system. With the two separate operating regimes elucidated and the analytical model established, we further unveil the dramatically different scaling relations between the CF and system parameters in the two regimes both

experimentally and theoretically, thereby enabling the rational interpretation and prediction of the performance of ICP-based EMC devices.

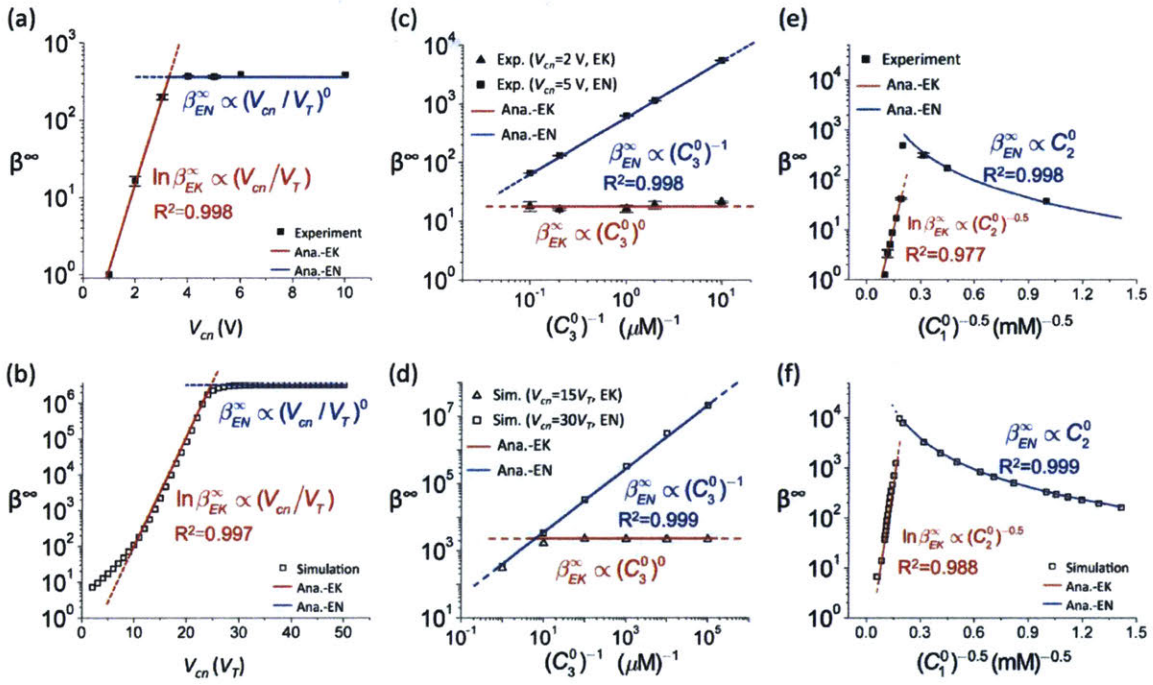


**Figure 2-5** Scaling relations between the CF and system parameters revealed by combining experiment, simulation, and theory. The red and blue lines are the fitting lines between the experimental/simulation results and the scaling laws revealed by the theoretical EK and EN limits, respectively. (a) Scaling relation between the CF and $V_{cn}$ by experiment. 1 μM fluorescent ssDNA in 10 mM KCl was used as the analyte. $V_{HL}$ was set to 10 V. (b) Scaling relation between the CF and $V_{cn}$ by simulation. 0.1 nM default particle in 1 mM KCl was used as the analyte. $V_{HL}$ was set to $20V_T$. (c) Scaling relation between the CF and the initial analyte concentration by experiment. Fluorescent ssDNA with varied initial concentrations in 10 mM KCl was used as the analyte. $V_{HL}$ was set to 10 V. (d) Scaling relation between the CF and the

initial analyte concentration by simulation. Default particle with varied initial concentrations in 1 mM KCl was used as the analyte. $V_{HL}$ was set to $20V_T$. (e) Scaling relation between the CF and the buffer concentration by experiment. 1 μM fluorescent ssDNA in KCl solutions of varied concentrations was used as the analyte. $V_{HL}$ was set to 10 V, and $V_{cn}$ was set to 5 V. (f) Scaling relation between the CF and the buffer concentration by simulation. 0.1 nM default particle in KCl solutions of varied concentrations was used as the analyte. $V_{HL}$ was set to $20V_T$, and $V_{cn}$ was set to $30V_T$.

## 2.4 Effects of experimental parameters

The CF has been reported to increase with $V_{cn}$ in the literature [23], [28], [38], [39], [57], though no explicit scaling relation between the CF and $V_{cn}$ could be determined. However, we find that the previous reports only represented one side of the coin. Fig. 2-5(a) shows the experimental dependence of the CF on $V_{cn}$ with 1 μM ssDNA in 10 mM KCl being the analyte. The CF initially increased exponentially with $V_{cn}$ and then reached a constant maximum value regardless of $V_{cn}$. Similarly, such two-phase behavior was also observed in numerical simulation (Fig. 2-5(b)), where we used an initial analyte concentration of 0.1 nM. The experimental and simulation results are clearly predicted by our analytical model. The exponential phase at relatively low $V_{cn}$'s corresponds to the EK-limited regime, in which the CF ($\beta_{EK}^{\infty}$) grows exponentially with Pe (Eq. 2.10). Because Pe is proportional to the average fluid velocity $\bar{u}$, and $\bar{u}$ increases linearly with $V_{cn}$ (see Section A1.3 of the Appendix 1), an exponential relation between the CF and $V_{cn}$ must hold. As the analyte concentration increases

with $V_{cn}$, the system will eventually enter the EN-limited regime, in which the CF ($\beta_{EN}^{\infty}$) is determined by the electroneutrality condition and hence independent of $V_{cn}$ (Eq. 2.10).

The dependence of the CF on the initial concentration of the analyte ($C_3^0$) has been controversial among different researchers. Wang *et al.*, [22] Anand *et al.* [57], Hlushkou *et al.* [35] and Song *et al.* [58] reported that higher CFs were achieved for samples with lower initial concentrations, while Hong *et al.* [59] found the CF to be independent of the initial concentration. Elucidation of the two separate operating regimes clearly concludes this controversy. In the EK-limited regime where the analyte concentration is much lower than buffer ions, the CF is determined by the electrokinetics of the system, which is not altered by the concentrating of the analyte. Therefore, the CF is theoretically independent of $C_3^0$ in the EK-limited regime (Eq. 2.10), as confirmed by the experimental result in Fig. 2-5(c) and simulation result in Fig. 2-5(d). In contrast, in the EN-limited regime where the maximum analyte concentration ($C_{EN}^{\infty}$) is a constant determined by the electroneutrality condition, the CF ($\beta_{EN}^{\infty} = C_{EN}^{\infty} / C_3^0$) is thus inversely proportional to $C_3^0$ (Eq. 2.10), as supported by Figs. 2-5(c-d). Therefore, the aforementioned discrepancy can be attributed to the different operating regimes: researchers reporting higher CFs at lower initial concentrations likely operated the devices in the EN-limited regime, while those reporting constant CFs regardless of initial concentrations likely operated the devices in the EK-limited regime.

Controversy also persists on the effect of the buffer concentration ($C_1^0$): Anand *et al.* [57] and Ko *et al.* [23] reported higher CFs in higher buffer concentrations, while it is also

commonly observed that the EMC effect vanishes in sufficiently high buffer concentrations due to the collapse of the ion depletion zone. Our study unveils the scaling relations between the CF and buffer concentration that capture both scenarios. At relatively low buffer concentrations, the ion depletion zone can be sufficiently developed due to the strong overlapping of electrical double layers in the nanochannels (i.e. strong cation-selectivity), which facilitates the effective trapping of the analyte. With the analyte almost completely trapped, the system enters in the EN-limited regime. In this case, the CF ( $\beta_{EN}^{\infty}$ ) increases proportionally with $C_1^0$ (Eq. 2.10), which directly determines the upper limit of the analyte concentration. This is confirmed by the experimental result in Fig. 2-5(e) and simulation result in Fig. 2-5(f). Further increase of $C_1^0$ compromises the ion depletion effect and brings the system from the "non-leaking" regime to the "leaking" regime, causing an abrupt drop of the CF (by nearly one order of magnitude), as shown in Figs. 2-5(e-f). The system subsequently enters the EK-limited regime at higher buffer concentrations, where the CF scales exponentially with $\bar{u}$ (Eq. 2.10). Because of the compromised ion depletion effect in this regime, the non-equilibrium EOF in the vicinity of the nanochannels is weakly developed. $\bar{u}$ is consequently dominated by the equilibrium EOF in the bulk channel, which is proportional to $(C_1^0)^{-0.5}$ [60]. Therefore, as confirmed by Figs. 2-5(e-f), the CF decreases exponentially with $(C_1^0)^{-0.5}$ at higher buffer concentrations in the EK-limited regime, i.e. $\ln\beta_{EK}^{\infty} \propto (C_1^0)^{-0.5}$.

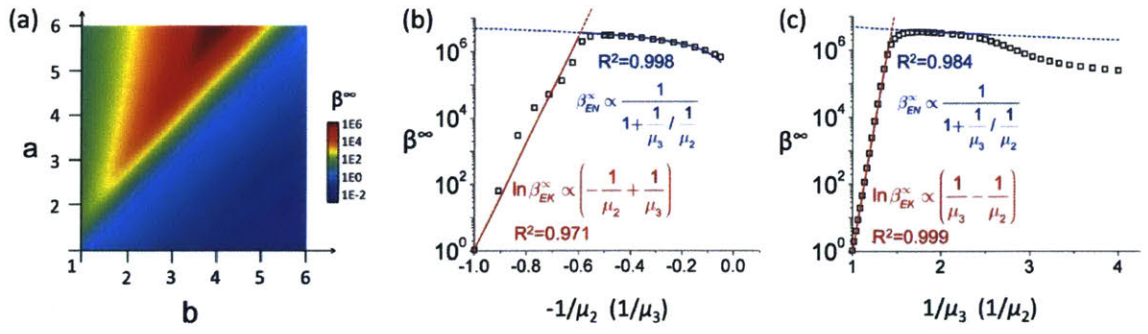


**Figure 2-6** Dependence of the CF on the electrophoretic mobility of buffer ions and the analyte. $V_{HL}$ was set to $20V_T$, and $V_{cn}$ was set to $30V_T$ in the simulation. (a) Condition for the analyte to be concentrated. The plot was computed by simulation. (b) Scaling relation between the CF and the electrophoretic mobility of buffer ions. (c) Scaling relation between the CF and the electrophoretic mobility of the analyte. The red and blue lines are the fitting lines between the experimental/simulation results and the scaling laws revealed by the theoretical EK and EN limits, respectively.

Finally, it is critical to understand how the properties of the analyte molecule and the composition of the buffer affect the CF for practical applications. However, this has been rarely known, mainly due to the lack of analyte molecules and ions with wide ranges of electrophoretic mobility for reliable parametric studies in experiments. Enabled by numerical simulation, we unveil the scaling relations between the CF and the electrophoretic mobility of the analyte and buffer ions, which are also well predicted by our analytical model. Firstly, according to Eq. 2.10, the CF is greater than 1 only when a>b, i.e. $\mu_2 > \mu_3$. This is clearly

supported by the simulation result in Fig. 2-6(a), where the CF is greater than 1 only in the region above the partition line a=b. This is because the anion is almost stationary in the upstream channel (i.e. $\overline{u} \approx \mu_2 E$, which causes $J_2 \approx 0$, see Section A1.1 of Appendix 1), and the analyte can only enter the central microchannel and be concentrated when $\overline{u} > \mu_3 E$, which requires $\mu_2 > \mu_3$. Therefore, the first rule of thumb for an analyte to be concentrated is that, the electrophoretic mobility of the analyte must be smaller than that of the anion. As $\mu_i \propto |Z_i D_i|$, we will discuss the scaling relations between the CF and the electrophoretic mobility by varying $D_i$ with fixed $Z_i$ for brevity (the result vice versa would be similar). Eq. 2.10 predicts that, the CF in the EK-limited regime obeys $\ln \beta_{EK}^{\infty} = \frac{(-Z_3)}{V_T} \cdot (\frac{1}{\mu_3} - \frac{1}{\mu_2}) \cdot \frac{\overline{u}L}{2}$, while that in the EN-limited regime obeys $\beta_{EN}^{\infty} = 2\frac{Z_2}{Z_3} \cdot \frac{1}{1 + \frac{1}{\mu_3} / \frac{1}{\mu_2}} \cdot \frac{C_1^0}{C_3^0}$. This is confirmed by the simulation result in Fig. 2-6(b), in which the CF increases proportionally with $-1/\mu_2$ in the EK-limited regime for a specific analyte, while relatively insensitive to $-1/\mu_2$ in the EN-limited regime. In other words, the CF is significantly enhanced in buffers with high ion mobility, because stronger electric field and vortical flows are generated in the ion depletion zone with ions of higher mobility (see Section A1.4 of Appendix 1), which enhances the trapping of the analyte. On the other hand, as confirmed by the simulation result in Fig. 2-6(c), for a specific buffer, the CF increases proportionally with $1/\mu_3$ in the EK-limited regime, while relatively insensitive to $1/\mu_3$ in the EN-limited regime. In other words, the CF is significantly decreased for analyte

molecules with very high electrophoretic mobility, because stronger electrophoretic velocity (leftward) prevents the analyte from entering the microchannel. It is worth noting that the analytical model (assuming $J_2^\infty \approx 0$) does not apply to the case of $J_2^\infty \gg 0$, which occurs when the electrophoretic mobility of the analyte is too small to facilitate the electrical trapping, as shown in Fig. 2-6(c).

## 2.5 Summary

In this chapter, we theoretically and experimentally elucidate the two separate operating regimes of ICP-based EMC and unveil the dramatically different scaling behaviors of the CF in the two regimes. These experimental and theoretical findings decipher the mechanism of ICP-based EMC, providing clear explanations to the controversies outstanding for over a decade. We believe that this work represents an important progress towards the scientific understanding of ICP-based EMC, and makes a stride towards the precise design and optimization of ICP-based EMC devices on demand of various applications.

## 2.6 Experimental section

### 2.6.1 Numerical simulation

In the simulation model, the central microchannel is 120 μm long and 4 μm wide, connecting two reservoirs of 60 μm long and 60 μm wide. The microchannel walls are negatively charged with a surface charge density of -5 mC/m$^2$. The nanochannel arrays are assumed to permit the passage of cations only, which is numerically implemented by setting a boundary condition of

constant cation concentration and zero anion flux [55], [61]–[63]. The default electrolyte is 1 mM KCl (diffusion coefficient: $2\times10^{-9}$ $m^2/s$) with 0.1 nM analyte. The default analyte is a divalently negatively charged particle with a diffusion coefficient 1/4 of that of $Cl^-$, i.e. a=4, b=2. The corresponding electrophoretic mobility of the default analyte is $3.87\times10^{-8}$ $m^2/Vs$, which is the typical value for short DNAs [64].

The governing equations are Eqs. 2.1-2.5, which are solved using COMSOL® (v5.2a). Transport of charged species and electric fields are implemented using the Transport of Diluted Species and Electrostatics Modules. The Poisson-Nernst-Planck (PNP) equations are solved using quadratic Lagrange interpolation functions for space discretization. Navier–Stokes (NS) and continuity equations are implemented in Creeping Flow Module. Quadratic Lagrange shape functions are used for NS equations whereas linear functions are used for the continuity equation. The boundary conditions are as follows. At the nanochannel array surfaces, it is assumed that: (1) fluxes of the anion and analyte across the nanochannels are zero; (2) the concentration of cations at the nanochannel array surfaces is 2 mM [55], [61]–[63]; (3) the electric potential at the nanochannel array surfaces is zero; (4) the nanochannel array surfaces are impermeable and no-slip to fluid (zero fluid velocity). At the microchannel walls, the boundary conditions are: (1) constant surface charge density of -5 $mC/m^2$; (2) no-slip condition for fluid velocity; (3) zero fluxes of ions and analyte. It is noted that the ICP effect changes the pH and ion concentration of the solution in the downstream channel, which in turn could affect the surface charge density. The modeling of this effect is a non-trivial task [65]. For the purpose of scaling analysis, we will simply assume a constant surface charge density, which has proved to provide good approximation of actual experimental systems by previous works [38], [39].

At the inlet boundary, the boundary conditions are: (1) the concentrations of the ions and analyte are the same as those in the inlet reservoir. (2) the electric potential is $V_H$; (3) the pressure is zero. At outlet boundary, the boundary conditions are: (1) free boundary conditions are applied for fluid flow; (2) the electric potential is $V_L$. At the reservoirs walls, the boundary conditions are: (1) no-slip condition for fluid velocity; (2) zero charge. The computational domain is meshed using quadrilateral elements. Finer grids are adopted near the charged walls, nanochannel array surfaces, inlet and outlet boundaries of the channel (see Section A1.5 of Appendix 1).

2.6.2 Experimental details

In the experiments, we used 10 mM KCl solution as the default buffer. The analyte molecule is Alexa Fluor 488-labeled 21-base ssDNA (5'-AGTCAGTCAGTCAGTCAGTCA-3') (Integrated DNA Technologies, IA). An inverted fluorescent microscope (IX71, Olympus) and a CCD camera (Sensicam qe, Cook Corp.) were used for imaging. A mechanical shutter was used to reduce the photo-bleaching effect. Micro-manager (www.micromanager.org) was used to synchronize the CCD camera and the mechanical shutter. ImageJ (National Institutes of Health, USA) was used for image analysis. A DC power supply (Stanford Research Systems, Sunnyvale, CA) was used to apply the voltages. A multi-meter (Fluke 189) was used to measure the voltages. Ag/AgCl electrodes (A-M Systems Inc.) were used as electrodes.

# Chapter 3 Specific enrichment of target biomolecules

Note: Section 3.2 is a direct reproduction of a previously published peer-reviewed journal paper (Wei Ouyang, Zirui Li, and Jongyoon Han, Anal. Chem. 2018, 90, 19, 11366-11375) with the permission of American Chemical Society. Appendix 2 is the supplementary information of this article.

Biomolecules function by binding specifically to their affinity binders. In principle, the specific enrichment of target biomolecules must be mediated by the recognition of their specific affinity binders. As discussed in Chapter 1, the specific recognition of the target DNA is realized by its complementary DNA(s), and the specific recognition of the target protein is realized by its complementary antibody (Ab). We are looking for techniques that can specifically enrich the cDNA-bound target DNA while not enriching background DNAs and specifically enrich the Ab-bound target protein while not enriching background proteins. The specific enrichment may be realized based on the differences in the sizes, surface charges, electrophoretic mobility, among others, between the cDNA-bound target DNA and background DNAs and between the Ab-bound target protein and background proteins.

In this chapter, we will first introduce the electrophoretic mobility-based spatial separation of biomolecules in the electrokinetic concentrator, and then the general principle of specific enrichment of target biomolecules using this phenomenon. Next, we will detailedly study the specific enrichment process and characterize the effects of various experimental factors.

## 3.1 General principle of specific enrichment of target biomolecules in the electrokinetic concentrator

As shown in Fig. 3-1, the electrokinetic concentrator functions as an electrical filter, in which all positively charged and neutral species simply pass and negatively charged biomolecules become concentrated. The location of concentration is the balancing point of the electrophoresis ($v_{EP}$) and electroosmosis ($v_{EOF}$), i.e. $v_{EP} = v_{EOF}$. The fluid velocity (electroosmosis, $v_{EOF}$) is constant along the channel because of the incompressibility of fluid (in the strict sense, the fluid velocity is the superposition of electroosmosis and pressure-driven flow, not just electroosmosis, as discussed in Chapter 2). Because $v_{EP} = \mu \cdot E$ ($\mu$, electrophoretic mobility; $E$, electric field), the higher the electrophoretic mobility, the lower the electric field is where the biomolecule is balanced/concentrated.

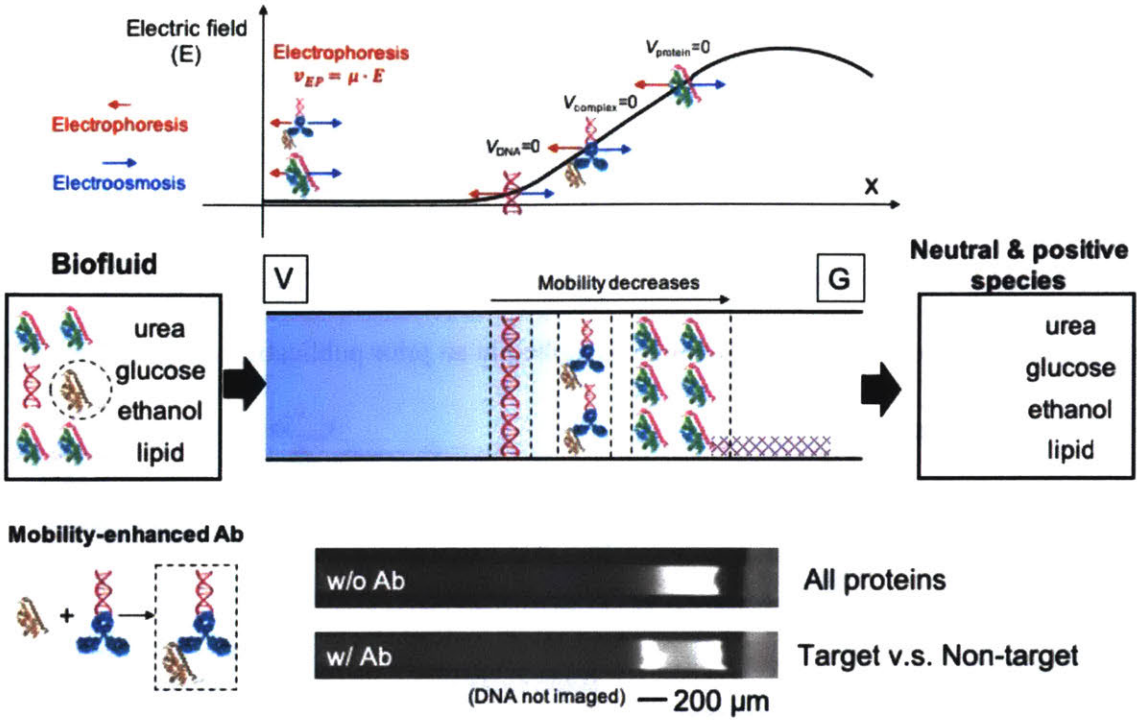


**Figure 3-1** Schematic of mobility-based separation of Ab-bound target protein and background proteins.

Based on this phenomenon, the Ab-bound target protein can be separated from the background proteins on the condition that they have different electrophoretic mobility that is resolvable by the electrokinetic concentrator. The intrinsic electrophoretic mobility of proteins (including antibody) are typically low and in a narrow range, making it difficult to directly separate the Ab-bound target protein from background proteins in the electrokinetic concentrator. We mobility-engineered the antibody by conjugating it with a DNA (high electrophoretic mobility due to highly charged backbone), thereby significantly increasing the electrophoretic mobility of the antibody (Fig. 3-1). Using the mobility-enhanced Ab, we were

able to separate the Ab-bound target protein from background proteins, as shown in Fig. 3-1. The upper fluorescence image shows the co-concentration of fluorescently labeled bovine serum albumin (BSA) and streptavidin (SA) in the same peak. After adding the BSA-specific mobility-enhanced Ab, two fluorescence peaks were resolved (lower fluorescence image), the left one being the Ab-bound BSA and the right one being the SA. The BSA-specific Ab was conjugated with a 96-base DNA (method described in an prior publication of the author [31]).

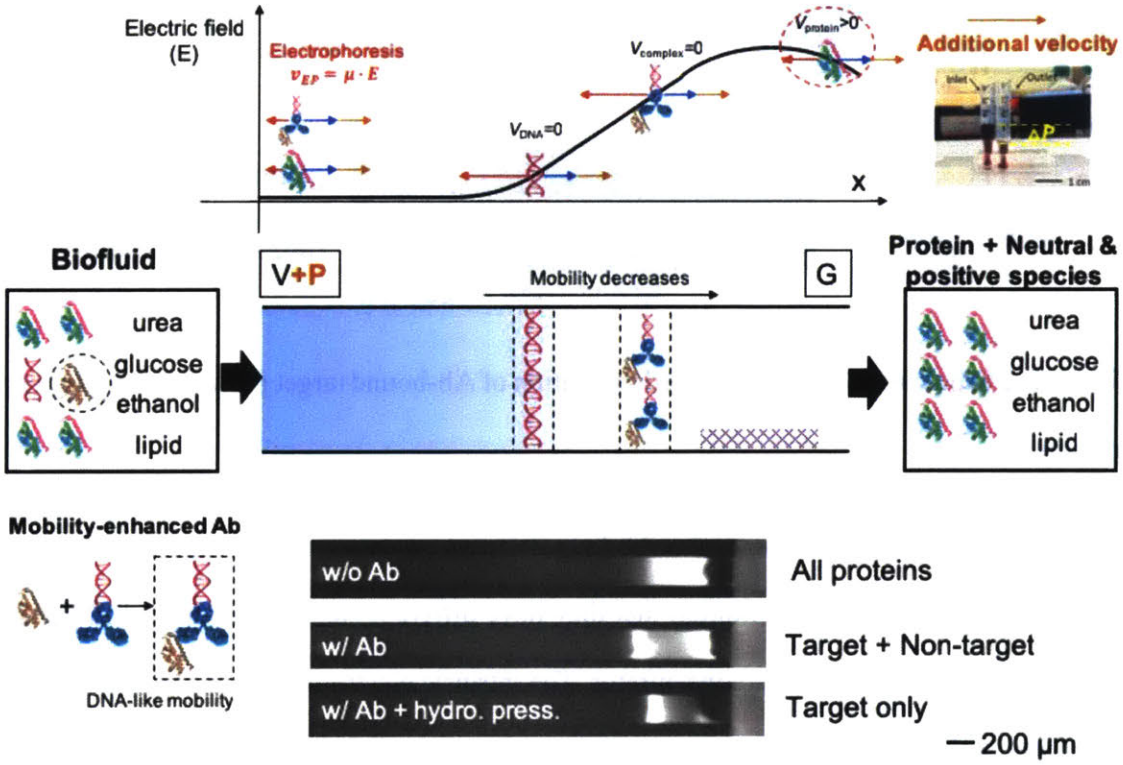


**Figure 3-2** Schematic of specifically enriching the Ab-bound target protein and simultaneous removal of the background proteins under an appropriate hydrostatic pressure.

The next question is how to selectively concentrate only the Ab-bound target protein while not enriching the background proteins. This can be realized by applying an appropriate additional velocity to the biomolecules, such that the background proteins (closest to the peak of the electric field) have enough momentum to overcome the electric field barrier while the Ab-bound target protein is still trapped in the electric field barrier, as shown in Fig. 3-2. The additional velocity can be applied and precisely controlled by the hydrostatic pressure difference between the inlet and outlet of the device.

While the mobility-based separation method works for the specific enrichment of target proteins, it cannot be directly applied to DNAs, because the cDNA-bound target DNA and background DNAs have the same electrophoretic mobility (the electrophoretic mobility of short DNAs is nearly constant). To induce mobility change of the cDNA-bound target DNA, we use a DNA analog, peptide nucleic acid (PNA), as the complementary probe. Because the PNA is charge-neutral, the PNA-DNA complex has lower electrophoretic mobility than the background DNAs, which enables the specific enrichment of the target DNA. The use of a PNA probe for specific enrichment of the target DNA is described in Chapter 5. Note that, even in DNA enrichment, it is critical not to enrich the highly abundant background proteins. Otherwise, the enriched highly abundant background proteins may cause high viscosity of samples or even aggregation, which often leads to the degradation or even failure of the devices.

In the specific enrichment of proteins, the Ab-bound target protein has high mobility similar to DNAs, which is separated from low-mobility background proteins; in the specific enrichment of DNAs, the high-mobility PNA-DNA and background DNAs are also separated from the low-mobility background proteins. In the following section, we will study the various

factors affecting the selective enrichment of DNAs (representing the high-mobility species) over proteins (representing the low-mobility species). The conclusions are applicable to the specific enrichment of DNAs and proteins, because of the similar mobility differences between the species we need to separate.

## 3.2 Characterization of the specific enrichment process and effects of various factors

### 3.2.1 Device design

As shown in Fig. 3-3(a), the device consists of a main microchannel, which is split into parallel, narrower channels in the concentration zone. The splitting of a wide channel into multiplexed narrow channels helps stabilize the concentration plugs by suppressing the electrokinetic vortices generated by ICP [66], which enables the massive scaling up of the channel dimension for high-throughput operations [67]. The cation-selective Nafion membrane (pore diameter: 4 nm [68]) is patterned on the glass slide (bottom of the channels) and bridges the upstream and downstream of the device. The inlet of the device is biased to an electric potential of $\varphi$ (>0), while the outlet is grounded (GND). As shown in Fig. 3-3(b), the main channel is 1.6 mm wide, which is split into 16 parallel channels of 100 μm wide and 10 mm long through evenly bifurcated tree structures. The parallel channels converge into a single channel of 1.6 mm wide through structures mirroring the splitting structures. All the channels are 15 μm deep. The Nafion strip is 9 mm from the entrances of the parallel channels (indicated by the blue box and shown in the inset photo in Fig. 3-3(b)). The parallel channels are sequentially numbered 1-16

as shown in Fig. 3-3(b). Fig.3-3(c) shows the side view of the device with 1 ml plastic syringe barrels as the reservoirs.

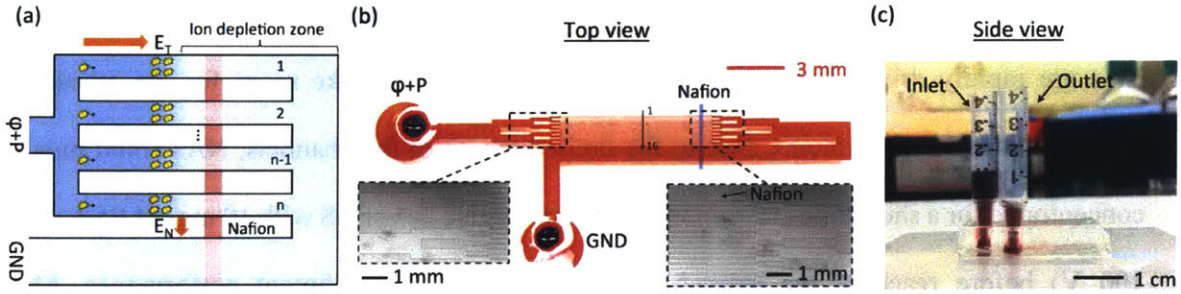


**Figure 3-3** Schematic and photos of the device. (a) Schematic of a multiplexed ICP-based ET device. (b) Top-view photo of the device fabricated by PDMS-glass bonding, and enlarged views of the device near the splitting and converging channels. (c) Side-view photo of the device.

### 3.2.2 Principle of selective concentration

Fig. 3-4 illustrates the concentration behavior in the presence of both nucleic acids (NAs) and proteins without an external pressure. As previously mentioned, negatively charged biomolecules are trapped where the electric field is $E = v_{EOF}/\mu$. Because the electrophoretic mobility of NAs is much higher than that of proteins ($\mu_{DNA} \gg \mu_{pro}$), proteins are concentrated closer to the Nafion membrane, where the electric field is stronger (Fig. 3-4(a)) [24], [31]. Under high voltages, as the concentration proceeds, the focused biomolecules (negatively charged) displace the local anions due to the electroneutrality condition until the local anion concentration becomes close to zero, at which the maximum local concentration of the focused

biomolecules is reached, namely the electroneutrality limit [69]. Because of the high concentration of proteins in human serum (60-80 mg/ml), the proteins instantly reach the electroneutrality limit, after which the concentrating of proteins could only proceed by the expanding of the protein concentration plug towards the upstream (Fig. 3-4(b)). Consequently, NAs are rapidly driven back towards the inlet reservoir to make room for the expanding concentration plug of proteins. Due to the limited length of the channels, NAs could only be concentrated for a short time (<2 min in the current device in 1×PBS with 10 mg/ml BSA under 100 V) before reaching the reservoir, resulting in poor enrichment performance. More importantly, the co-concentration of background proteins necessitates the purification of NAs with additional steps, which would otherwise significantly compromise the sensitivity and specificity of downstream assays. Additionally, the inability to stably localize the concentration plug in a specific region of the channels, such as functionalized affinity-capture surfaces, makes it difficult to couple ICP-based electrokinetic trapping with conventional surface hybridization-based assays.

To address the aforementioned challenges in enriching and purifying NAs in complex biological samples, we introduce an additional pressure-driven flow (PDF) into the system, as illustrated in Figs. 3-4(c-d). With an external pressure applied to the device, the fluid flow in the microchannels is the superposition of the EOF and PDF. In one-dimensional analysis, negatively charged biomolecules are trapped at the location where $E = (v_{EOF} + \bar{v}_{PDF})/\mu$, in which $\bar{v}_{PDF}$ is the cross-sectional average velocity of the PDF. With the addition of the PDF, biomolecules of the same electrophoretic mobility are concentrated closer to the Nafion membrane, where the electric field is stronger. As shown in Fig. 3-4(c), with the pressure

appropriately modulated, one could concentrate the proteins in the vicinity of the peak of the electric force barrier. In this scenario, the concentrated proteins could overcome the electric force barrier easily by diffusion. As a result, the concentration of proteins quickly reaches the steady state, at which the influx of proteins is offset by the leakage of proteins across the electric force barrier. As shown in Fig. 3-4(d), in pressure-modulated selective electrokinetic trapping (PM-SET), NAs are stably continuously trapped without back-propagation, while proteins are continuously leaked and removed from the concentration plug. The hydrostatic pressure is maintained constant by the replenishing of sample or buffer into the inlet and removal of waste from the outlet periodically. Finally, the sample in the inlet is replaced with clean buffer. Afterwards, the NAs remain being concentrated, while residual proteins in the upstream channel gradually leaked into the downstream, thereby realizing the both the enrichment and purification of NAs. It is noted that, in practice, when we modulated the pressure such that proteins completely overcame the electric force barrier, there might be strong leakage of NAs across the barrier, or even failure of NA concentration, due to the limited separation resolution between proteins and NAs in the device. Therefore, to ensure the efficient enrichment of NAs, we still have the proteins weakly concentrated in our implementation of PM-SET, as previously described.

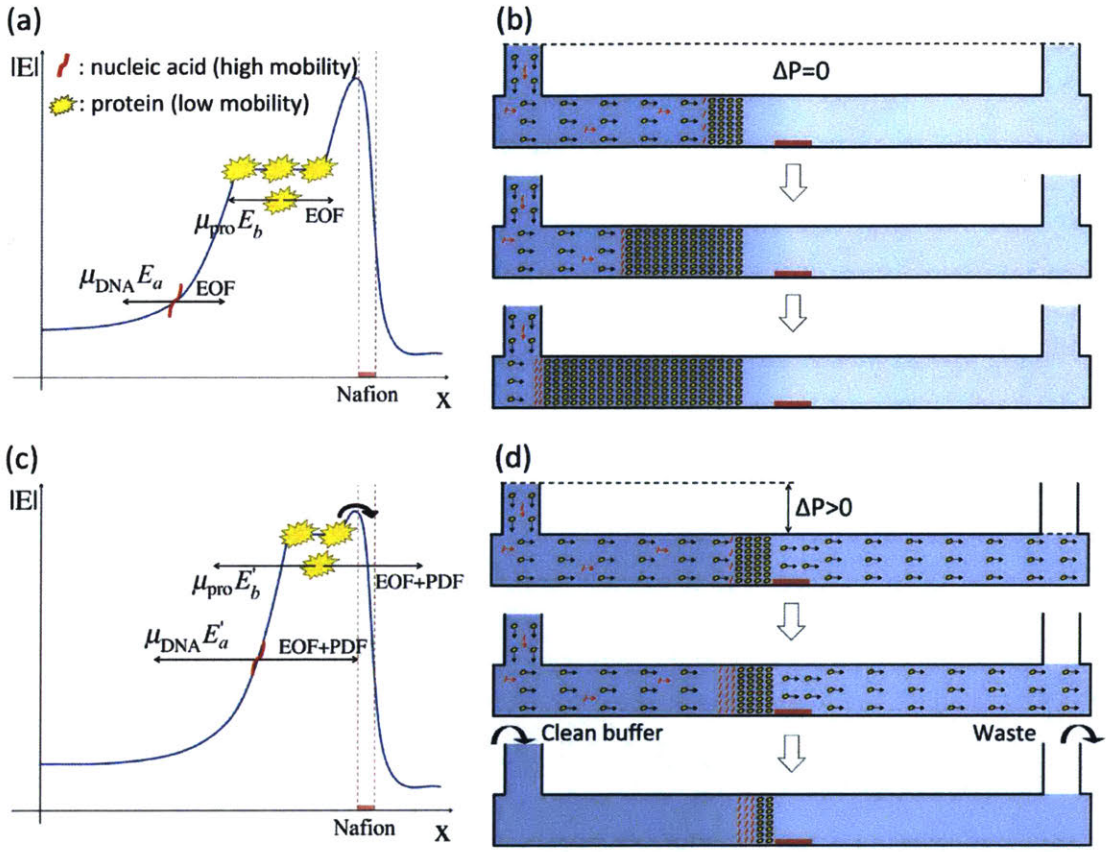


**Figure 3-4** Principle of PM-SET. (a) The electrophoretic mobility of NAs is higher than that of proteins, so NAs concentrate farther from the Nafion membrane than proteins, where the electric field is weaker. (b) The co-concentration of proteins and NAs causes the rapid back-propagation of the NAs. (c) Under an external hydrostatic pressure, proteins easily leak through the electric force barrier, while NAs are still effectively concentrated. (d) Under an external hydrostatic pressure, NAs are stably concentrated near the ion depletion zone, while the background proteins are removed, enabling the simultaneous enrichment and purification of NAs.

### 3.2.3 Optimization of Ionic Strength

We first explored the experimental conditions using BSA in PBS to simulate human serum. Fig. 3-5(a) shows the concentration plugs of the Alexa Fluor 647-labeled ssDNA under different conditions (different ionic strengths and BSA concentrations, but hydrostatic pressure was zero for all cases). The experiments were terminated when the concentration plug back-propagated beyond the entrances of the parallel channels or after 5 min, whichever happened first. In 0.1×PBS, as we increased the BSA concentration from 0 to 10 mg/ml, the DNA concentration plug significantly back-propagated due to the co-concentration of BSA. More importantly, there was strong dispersion of the DNA concentration plug (forming long tails) at 10 mg/ml BSA, causing significant loss of the DNA. We speculate that this was caused by the non-specific binding between the highly negatively charged backbone of DNA and positive amino acid residues of BSA at low ionic strengths [70]. As we increased the ionic strength from 0.1×PBS to 1×PBS, dispersion was significantly reduced even with 10 mg/ml BSA. We speculate that this may have benefitted from the effective screening of the surface charges of the DNA and BSA at high ion concentrations. In the meantime, from the perspective of the Kohlrausch regulating function in electrophoresis [71], more NAs can be concentrated and into narrower zones as the ion concentration increases, which contributes to the less dispersion at high ion concentrations. Based on this scheme, we found that DNA with background BSA concentrations of 50-100 mg/ml could be concentrated with significantly reduced dispersion in 2.5×PBS.

Based on the fitted linear relationship between the fluorescence intensity and DNA concentration (Section A2.3 of Appendix 2), the maximum DNA concentration in a

concentration plug ($c_{max}$) can be calculated by its peak fluorescence intensity. The enrichment factor of a concentration plug is defined as the ratio of the maximum DNA concentration to the initial DNA concentration ($c_0$, which is 1 nM in this work), i.e. $c_{max}/c_0$. Fig. 3-5(b) shows the enrichment factor achieved at the end of the experiments under different conditions. An enrichment factor of ~2200 was achieved in 5 min in 0.1×PBS, owing to the high velocity (~1 mm/s, see Section A2.4 of Appendix 2) of the non-equilibrium EOF generated in this device, which is ~10 times faster than conventional electroosmosis [22]. With the increment of the BSA concentrations, the enrichment factor of DNA decreased due to the loss caused by the non-specific binding to BSA. With background BSA concentrations of 50-100 mg/ml, enrichment factors of 500-1500 could be achieved in 2.5×PBS and 5×PBS in 5 min. Lastly, the electric currents of the device in high ion concentration buffers were significantly increased but still stable over time (see Section A2.5 of Appendix 2), indicating that the device could be operated in high ion concentrations.

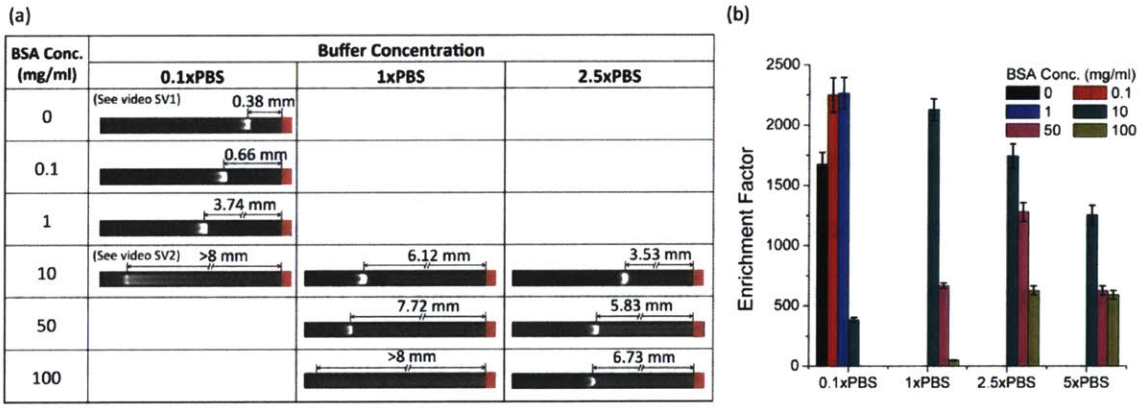


**Figure 3-5** Optimization of the ionic strength. (a) The DNA concentration behaviors at different ionic strengths and BSA concentrations without external pressures in the 9$^{th}$ channel.

The dispersion of the DNA concentration plugs at high concentrations of BSA was mitigated by high ionic strengths. The experiments were terminated after 5 min or when the concentration plugs back-propagated beyond the entrances of the parallel channels, whichever happened first. (b) The enrichment factor achieved at different ionic strengths and BSA concentrations at the end of the experiments.

### 3.2.4 Enrichment and Purification of NAs in BSA-Rich Samples by PM-SET

Using Alexa Fluor 647-labeled ssDNA with a background BSA concentration of 50 mg/ml in 2.5×PBS, we investigated the feasibility of PM-SET for the selective enrichment of NAs. The strong intrinsic fluorescence from 50 mg/ml BSA at an excitation wavelength of ~488 nm enabled us to directly image BSA in the device without fluorescence labeling. Fig. 3-6(a) shows the initial state of the device ($\varphi$=0 V). BSA concentration was uniform on the left (upstream) and right (downstream) sides of the Nafion membrane. DNA was not observable at its initial concentration (1 nM). When the hydrostatic pressure was zero (Fig. 3-6(b)), after the voltage was on for 30 s, both the DNA and BSA were trapped and concentrated at the upstream side of the Nafion membrane. Consequently, BSA was depleted at the downstream, as indicated by the vanishing of fluorescence at the downstream. On the other hand, as shown in Fig. 3-6(c), under an appropriate hydrostatic pressure (100 Pa in this case), while DNA was still effectively concentrated, BSA was only weakly concentrated. The expansion of the BSA concentration plugs under 100 Pa were much shorter than that under 0 Pa. The fluorescence intensities of BSA at the upstream and downstream were nearly the same, indicating the strong

leakage of BSA across the electric force barrier. Therefore, DNA could be selectively concentrated by PM-SET.

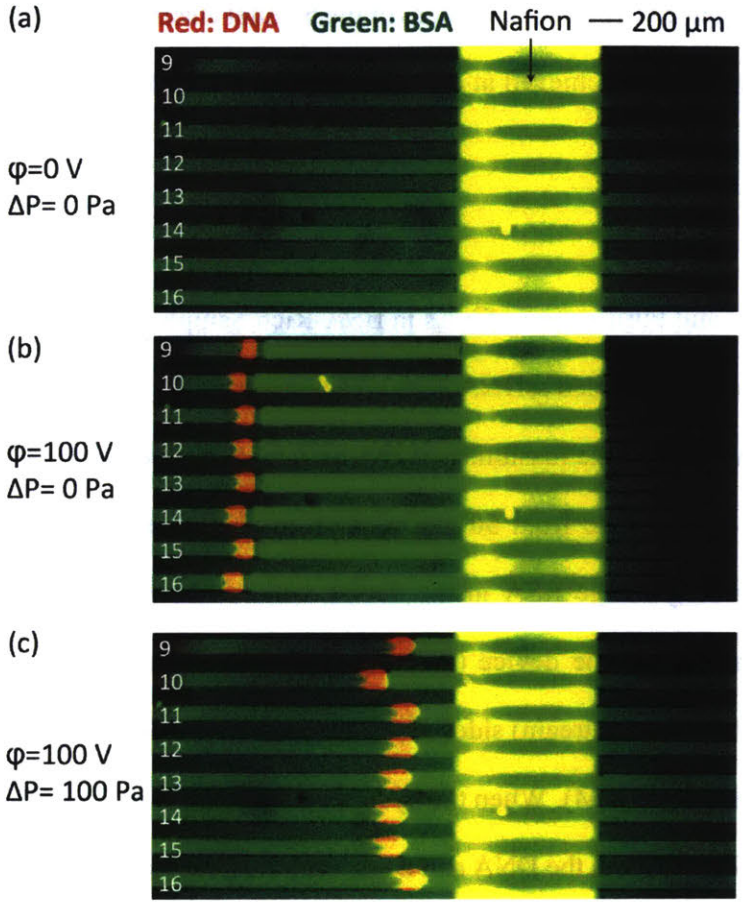


**Figure 3-6** Comparison of DNA and BSA concentration behaviors with and without a hydrostatic pressure. Fluorescently labeled DNA was imaged at an excitation wavelength of ~647 nm. The intrinsic fluorescence of BSA was imaged at an excitation wavelength of ~488 nm. The exposure time was 1000 ms. (a) The initial state of the device (φ=0 V). BSA concentration was uniform at the left (upstream) and right (downstream) sides of the channels. DNA (1 nM) was not observable. (b) DNA and BSA were co-concentrated near the Nafion

when the hydrostatic pressure was zero, resulting in the depletion of BSA downstream. The image was captured at t=30 s. (c) Under 100 Pa, DNA was still effectively concentrated, while BSA significantly leaked to downstream, indicated by the fact that the BSA fluorescence in the downstream was as strong as that in the upstream. The image was captured at t=30 s.

We next studied the temporal behavior of PM-SET. As shown in Fig. 3-7(a), without an external pressure, both the DNA and BSA were concentrated, causing the rapid back-propagation of the DNA concentration plug. In contrast, under 100 Pa (Fig. 3-7(a)), due to the leakage of BSA across the electric force barrier, the concentrating of BSA reached the steady state within a few seconds, after which the BSA concentration zone no longer expanded. Meanwhile, DNA was continuously concentrated adjacent to the BSA concentration zone without back-propagation. After 5 minutes' concentration, a washing step was performed to further purify the background of the concentrated DNA by replacing the sample in the inlet with 2.5×PBS. As the device continued to operate, residual BSA in the upstream channel escaped to the downstream channel across the electric force barrier. As shown in Fig. 3-7(a) (480 s), the BSA concentration zone also shrank, because BSA in the concentration zone continuously leaked to downstream, but the influx of BSA from the upstream gradually vanished after buffer replacement. The concentration behaviors under 70 Pa and 120 Pa are shown in Section A2.6 of Appendix 2.

As shown in Figs. 3-7(b), the selectivity of DNA and BSA concentration was dependent on the magnitude of the pressure applied. Under 70 Pa, the leakage rate of BSA was not

sufficient to offset the influx of BSA from the upstream, which still allowed the continuous concentrating of BSA but with a slower speed compared to that under 0 Pa, as inferred from the propagation distances of the DNA concentration plugs. Under 100 Pa, the leakage rate of BSA matched the influx of BSA from the upstream, thereby establishing the steady state of BSA concentrating. Further increase of the pressure to 120 Pa would enable the escape of both the DNA and BSA, resulting in the failure of concentration. The enrichment factor of the DNA increased with the pressure owing to the increased influx of the DNA at higher flow rates (Fig. 3-7(c)), until the failure of concentration under too high pressures. An enrichment factor of ~2400 was achieved for the DNA in 5 min under 100 Pa.

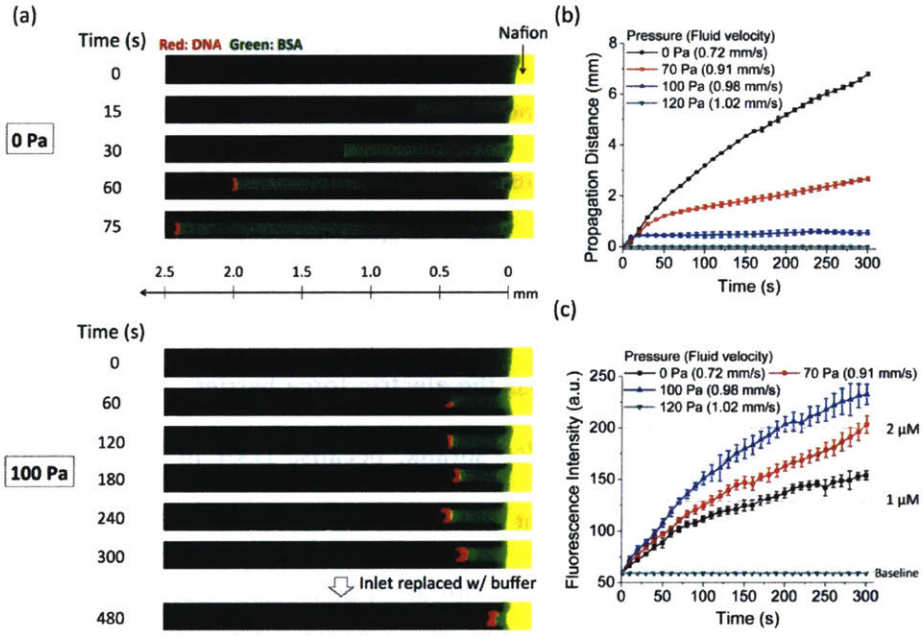


**Figure 3-7** Temporal behavior of selective NA enrichment and purification in BSA-rich samples by PM-SET. (a) Overlapped fluorescence images showing the co-concentration of the DNA and BSA under 0 Pa and 100 Pain the 9$^{th}$ channel. Fluorescently labeled DNA was

imaged at an excitation wavelength of ~647 nm. The intrinsic fluorescence of BSA was imaged at an excitation wavelength of ~488 nm. (b) The back-propagation distances of the DNA concentration plugs under different pressures. The average fluid velocities corresponding to the pressures are labeled in the legend (see Section A2.4 of Appendix 2). (c) The temporal evolution of the fluorescence intensities of the DNA concentration plugs under different pressures. The reference DNA concentrations are marked by the dashed lines. The average fluid velocities corresponding to the pressures are labeled in the legend.

### 3.2.5 Application of PM-SET to NAs in Human Serum

We next implemented PM-SET to directly enrich and purify NAs in human serum. Fig. 3-8(a) shows the concentration behaviors of the fluorescently labeled DNA spiked in human serum under different ionic strengths and hydrostatic pressures. DNA in native serum could barely be concentrated due to the strong non-specific binding between the DNA and background proteins. In native serum, the serum protein concentration plugs propagated to the entrances of the parallel channels (~8 mm) in a minute, while the NA concentration plugs were not observable. As we increased the ionic strength to 2.5×PBS, the serum protein concentration plugs reached the entrances of the parallel channels in ~75 s, yet the NA concentration plugs were still not resolved. The dispersion problem was mitigated by the increment of the ionic strength to 5×PBS, at which a sharp concentration plug of the DNA was formed. However, the co-concentration of serum proteins caused the rapid back-propagation of the DNA concentration plug, which reached the inlet reservoir in ~5 min (Fig. 3-8(b)). With an external

pressure of 100 Pa, the leakage of serum proteins across the electric force barrier did not fully offset the influx of serum proteins from the inlet, resulting in the slower but non-zero back-propagation of the DNA concentration plug. Under 200 Pa, the concentrating of serum proteins reached the steady state, while the DNA was selectively concentrated with minimal back-propagation (~1 mm from the Nafion membrane). With the optimal condition of 5×PBS and 200 Pa, an enrichment factor of ~4800 was achieved for the spiked DNA in human serum in 15 min (Fig. 3-8(c)).

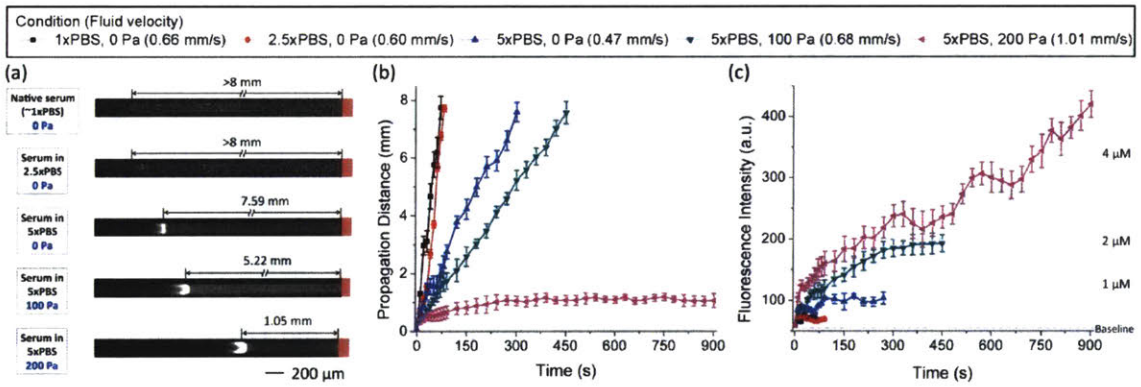


**Figure 3-8** Application of PM-SET to NAs in human serum. (a) Optimization of the ionic strength and pressure to realize selective enrichment of the DNA. The fluorescence images represent the 9$^{th}$ channel, and were taken at an excitation wavelength of ~647 nm. Fluorescence images for native serum and serum in 2.5×PBS were taken when the concentration plugs back-propagated beyond the entrances of the 9$^{th}$ channel. Fluorescence images for serum in 5×PBS were taken after 5 minutes' concentration. The average fluid velocities corresponding to different conditions are labeled in the legend (see Section A2.4 of Appendix 2). (b) The back-propagation distances of the NA concentration plugs under different conditions. (c) The

temporal evolution of the fluorescence intensities of the DNA concentration plugs under different conditions. Experiments were terminated when the concentration plug back-propagated beyond the entrances of the channels or after 15 min, whichever happened first. The reference DNA concentrations are marked by the dashed lines.

### 3.2.6 Experimental section

#### *3.2.6.1 Reagents and chemicals*

20×Phosphate Buffered Saline (PBS) and distilled water were purchased from Thermo Fisher Scientific (Waltham, MA). 0.1×PBS, 1×PBS, 2.5×PBS and 5×PBS solutions were prepared by diluting 20×PBS with distilled water to desired concentrations. Albumin from bovine serum (BSA) was purchased from Sigma-Aldrich (St. Louis, MO). 100 mg/ml BSA solutions in 0.1×PBS, 1×PBS, 2.5×PBS, and 5×PBS were prepared by dissolving 100 mg BSA in 1 ml PBS buffers of the corresponding concentrations. Human serum was purchased from MilliporeSigma (Burlington, MA). Human serum samples (native ionic strength: ~1×PBS) in 2.5×PBS and 5×PBS were prepared by spiking 0.086×volume and 0.267×volume of 20×PBS into 1×volume of native human serum, respectively. Nafion resin (20 wt % solution in lower aliphatic alcohol/$H_2O$ mix) was purchased from Sigma-Aldrich (St. Louis, MO). Single-stranded DNAs (ssDNAs) were synthesized and fluorescently labeled by Integrated DNA Technologies (Coralville, IA). A 22-base ssDNA (5'-GTA GGC GAA CCC TGC CCA GGT C-3') with 3' labeled by Alexa Fluor 647 was used for the demonstration of NA enrichment. In the DNA detection experiment, the target DNA was an unlabeled 67-base ssDNA (fragment

of Mycobacterium tuberculosis IS6110 gene) with the sequence of 5'- ACC AGC ACC TAA CCG GCT GTG GGT AGC AGA CCT CAC CTA TGT GTC GAC CTG GGC AGG GTT CGC CTA C-3' [72]. The probe for DNA detection was a complementary 22-base MO oligo (5'-GTA GGC GAA CCC TGC CCA GGT C-3') labeled by fluorescein at 3' (Gene Tools, LLC, Philomath, OR). BODIPY FL fluorescence dye was purchased from Life Technologies (Carlsbad, CA). Tygon non-DEHP microbore tubing (inner diameter: 0.020 inch, outer diameter: 0.060 inch) was purchased from Cole-Parmer (Vernon Hills, IL). 1 mL plastic syringe was purchased from Becton, Dickinson and Company (Franklin Lakes, NJ). Ag/AgCl electrodes (diameter: 0.008 inch) were purchased from A-M Systems (Sequim, WA).

*3.2.6.2 Device fabrication*

The microchannels were fabricated using polydimethylsiloxane (PDMS) (Sylgard 184, Dow Corning Inc., Midland, MI). First, the desired design was patterned on a silicon wafer using SU-8 photoresist (MicroChem, Westborough, MA) to obtain the master mold, which was subsequently treated with trichlorosilane (Sigma-Aldrich, St. Louis, MO) in a vacuum desiccator overnight to prevent adhesion to PDMS. Next, PDMS was poured onto the master mold. After being cured in an oven at 65°C for 3 hours, the PDMS was peeled off from the master. Access holes of 2 mm in diameter were punched in the PDMS at the inlet and outlet. The Nafion strip was patterned on a glass slide by the micro-flow patterning technique using microchannels of 400 μm wide and 50 μm deep, which has a final thickness of 1.5-1.8 μm [23]. The PDMS chip was irreversibly bonded to the Nafion-patterned glass slide by plasma bonding using the Femto Science Covance Plasma Cleaner (Hwaseong-Si, Gyeonggi-Do, Korea).

*3.2.6.3 Microfluidic experiments*

The hydrostatic pressure ($\Delta P$) was determined by the height differences ($\Delta H$) between the liquid levels in the inlet and outlet, which was controlled by the volume differences ($\Delta V$) between the samples loaded into the reservoirs ($\Delta P=4\rho g\Delta V/\pi D^2$, where $\rho$ is the density of water,$g$ is the gravitational acceleration, and $D$=4.78 mm is the diameter of the syringe barrels). In this work, hydrostatic pressures of 70, 100, 120, 200 Pa were generated by volume differences of 126, 180, 216, 360 μL between the inlet and outlet, respectively. For applications where the sample volumes are small (*e.g.* <100 μL), an alternative packaging scheme of the device is provided in Section A2.1 of Appendix 2 that allows the control of the hydrostatic pressure regardless of the sample volume (by adjusting the height of the tubing connected to the outlet).

For the demonstration of NA enrichment by PM-SET, the fluorescently labeled DNA was spiked into BSA-rich buffers and human serum samples to a final concentration of 1 nM. In the DNA detection experiment, the MO probe and target DNA were spiked into human serum in 5×PBS to a final MO probe concentration of 1 nM and final target DNA concentrations of 1 pM to 100 nM. The MO-DNA mixtures in serum were incubated for 10 min on a vortex mixer before being loaded into the chip.

Before the experiments, the microchannels were passivated with 1% BSA in 1×PBS for 10 min, and flushed with 1×PBS afterwards. Ag/AgCl electrodes (diameter: 0.008 inch) were inserted into the reservoirs and connected to a DC power supply (Stanford Research Systems, Sunnyvale, CA). 100 V was applied in all the experiments. The washing step in PM-SET was performed as follows: first, the sample was pipetted out of the inlet; Immediately afterwards,

buffer solution of the same ionic strength and volume was pipetted into the inlet; finally, the device ran for 3 min, after which the concentrated NA could be used for potential subsequent assays. The voltage was kept on during the washing. The concentration plugs would be flushed towards the inlet by the reversed hydrostatic pressure when the sample was pipetted out of the inlet, but they would flow back and be restored near the Nafion a few seconds after the buffer solution was pipetted into the inlet.

Fluorescence images were acquired using an inverted fluorescence microscope (IX71, Olympus, Tokyo, Japan) and a CCD camera (Sensicam qe, Cooke Corp., Romulus, MI). The exposure time is 100 ms unless otherwise specified. A mechanical shutter was used to reduce the photobleaching effect, which was synchronized with the CCD camera by the open source software Micro-manager.

*3.2.6.4 Data processing*

The data processing procedure is described in detail in Section A2.2 of Appendix 2. Briefly, raw fluorescence micrographs were opened in ImageJ, in which the fluorescence profiles of the channels were measured. Based on the fluorescence profiles, the peak fluorescence intensities and the distances between the peak and Nafion membrane in the channels were extracted in Excel 2010 for Mac. Due to the limited field of view of the fluorescence microscope, we could only image no more than 13 channels in our time-lapse imaging. Because the concentration behaviors were highly uniform among the 16 channels [67], we used data from the $9^{th}$-$16^{th}$ channels (the lower half) to represent the performance of a device (discussed in Section A2.2 of Appendix 2). Each experimental condition was tested three times using three different devices. We used the grand mean (mean of all 3×8 points) and the total

standard deviation (of all 3×8 points) for each data point and the corresponding error bar (discussed in Section A2.2 of Appendix 2), respectively.

# Chapter 4 Billion-fold enrichment of target biomolecules

Note: This Chapter is a partial direct reproduction of a previously published peer-reviewed journal paper (Wei Ouyang, and Jongyoon Han, Proceedings of the National Academy of Sciences Aug 2019, 116 (33) 16240-16249) with the permission of National Academy of Sciences. Appendix 3 is the supplementary information of this article.

In the past two decades, a number of microfluidic techniques have been developed for biomolecule enrichment, such as field amplified sample stacking [17], isoelectric focusing [73], electric field gradient focusing [18], dielectrophoretic trapping [74], isotachophoresis [75], and electrokinetic trapping [22]. Being physical methods, microfluidic enrichment techniques are naturally immune to the issues of chemical amplification and are applicable to both nucleic acids and proteins. However, despite the significant efforts on improving the enrichment performance by optimization of experimental conditions, operation protocols, and device design [33], [57], [75], existing microfluidic enrichment techniques could only achieve $10^2$- to $10^6$-fold enrichment of biomolecules in an hour [33], [75], which is essentially limited by the small sample volumes (~microliters) microfluidic devices can process in a reasonable amount of time (considering mass conservation). With performance far below that of PCR, existing microfluidic enrichment techniques cannot meet the needs of clinical diagnostics. Here we report a Hierarchical NanOfLuidic Molecular Enrichment System, termed HOLMES, that is capable of achieving billion-fold enrichment of biomolecules within 30 min. Unlike previous works that focused on the optimization of individual concentrators, we propose the paradigm

of hierarchical concentration, in which massively parallel nanofluidic concentrators are simultaneously operated to concentrate biomolecules from milliliters of samples and subsequently the concentrated biomolecules are reconcentrated into a single microfluidic zone by hierarchical cascading structures, thereby dramatically increasing the concentration throughput and speed. Besides its record-breaking performance that far exceed conventional techniques, HOLMES also remarkably features the ability to selectively enrich target biomolecules and simultaneously deplete non-targets directly from raw clinical samples, thereby enormously increasing the signal-to-noise ratio of detection. Furthermore, HOLMES is fabricated by the low-cost polydimethylsiloxane (PDMS) and operated simply by DC voltages and gravitational flows, making it ideal for point-of-care settings.

## 4.1 Principle and design of HOLMES

HOLMES has a hierarchical architecture with vertically stacked massively parallel microchannels in the first stage and a single microchannel in the final stage, between which the numbers of microchannels are scaled down by 10- to 100-fold per stage (Fig. 4-1(A)). Each stage has an input port from the main inlet or prior stage, an output port to the latter stage or final outlet, and valved side outlets. Within each stage, a perpendicularly patterned nanochannel network bridges the parallel microchannels and side buffer channels at the bottom. The nanochannel network is made by the cation-selective membrane Nafion (pore diameter: ~4 nm [68]) in this work to enrich negatively charged biomolecules (nucleic acids and most proteins at the neutral pH). Positively charged biomolecules can be enriched by use of anion-selective membranes. When a stage is activated, the input is biased to a positive DC

voltage (V), the side outlet(s) are opened and grounded (G), and the buffer channels are grounded (G) (Fig. 4-1(B)).

Under this configuration, a tangential electric field ($E_T$) is induced along the microchannels, and a normal electric field ($E_N$) is induced along the Nafion nanochannel network. Driven by $E_N$, cations in the microchannels are preferentially transported through the highly conductive cation-selective nanochannel network to the buffer channels, inducing ion depletion zones with significantly amplified electric fields near the micro-nanochannel junctions (Fig. 4-1(B)) [34]. Meanwhile, under $E_T$, biomolecules enter the microchannels with the fluid flow induced by the electric field (electroosmosis, EO), but are also subject to counter-directional electric force (electrophoresis, EP), which is proportional to the magnitude of the electric field. As biomolecules enter the ion depletion zones, the electrophoretic velocity grows as strong as the electroosmotic velocity (net velocity becomes zero), resulting in the electrokinetic trapping of biomolecules (Fig. 4-1(B)). Accompanying the continuous electroosmotic injection of samples into the microchannels, biomolecules become concentrated at the trapping points [34], [69]. Biomolecules concentrated in massive parallel microchannels are released and reconcentrated into the second stage with fewer microchannels by closing the side outlets of the first stage and opening those of the second stage (Figs. 4-1(C) and Section A3.1 of Appendix 3), which is repeated stage by stage until biomolecules are reconcentrated into the single microchannel in the final stage. Through reconcentration, the concentration performance is dramatically increased.

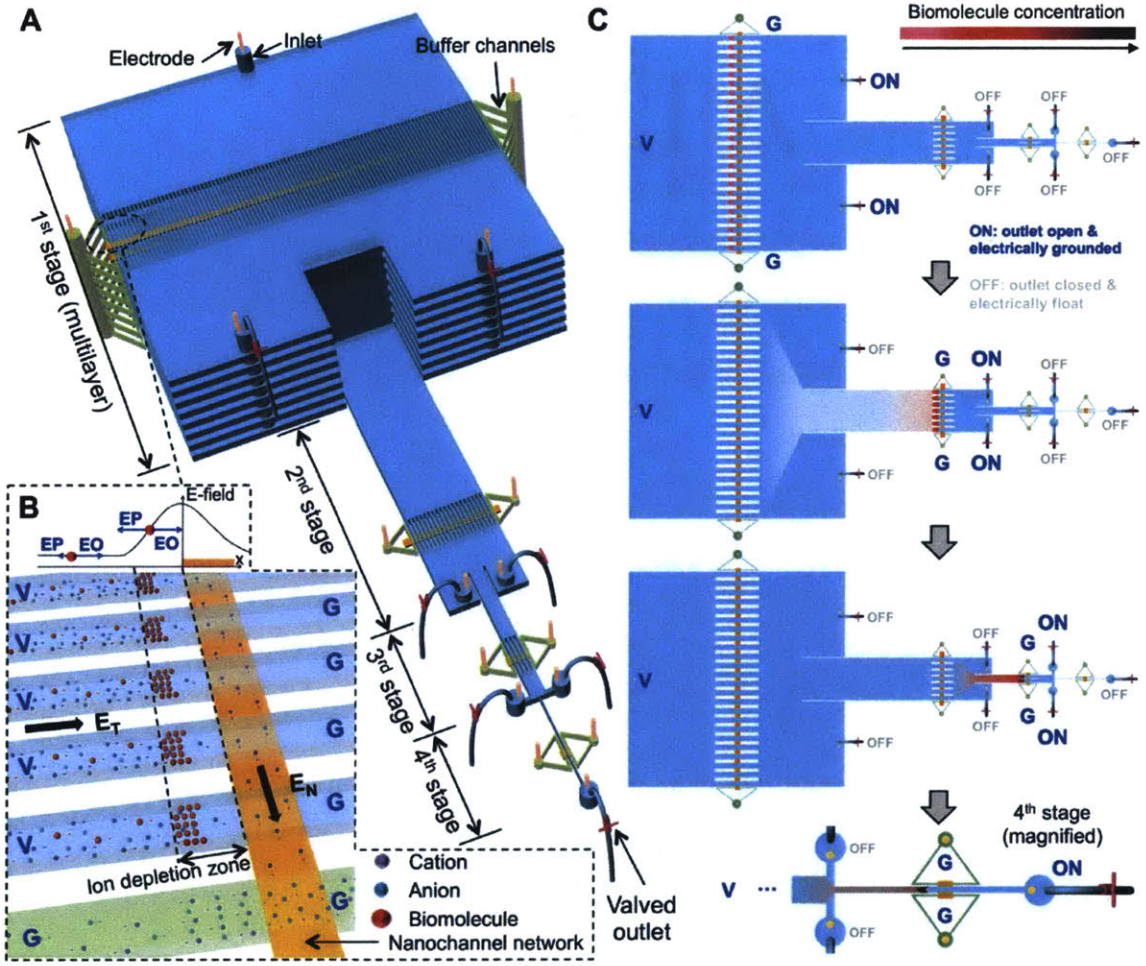


**Figure 4-1** Principle of HOLMES. (A) Schematic of HOLMES with hierarchical multi-stages. At each stage, parallel microchannels and buffer channels are bridged by a thin nanochannel network patterned on the bottom of the microchannels. (B) Schematic of nanofluidic biomolecule concentration in massively parallel channels. Under the electrical configuration shown, biomolecules are electroosmotically injected into the parallel channels and electrokinetically concentrated in the ion depletion zones induced near the micro-nanochannel

junctions. (C) Schematic of relayed reconcentration of biomolecules from massively parallel microchannels into a single microchannel to dramatically boost the concentration performance.

We designed devices with different enrichment capacities to suit the needs of various applications (Fig. 4-2(A)). The 640- (Fig. 4-2(B)), 3200- (Fig. 4-2(C)), and 38400-plex (Fig. 4-2(D)) devices comprise 64, 320, and 3840 channels of 200 μm wide in the first stage and a single channel of 20 μm wide in the final stage (all channels are 15 μm deep), with equivalent channel width ratios of 640, 3200, and 38400, respectively. The 640-, 3200-, and 38400-plex devices can concentrate biomolecules from ~0.2, ~1.0, and ~10.0 mL of samples in 0.1× phosphate buffered saline (PBS) in 15 min in the first stage, respectively, which ultimately converge into a concentration zone (~10 pL) in the final stage. Based on mass conservation, one could expect concentration of biomolecules by $10^7$-, $10^8$-, and $10^9$-fold, respectively. The 38400-plex device consists of 12 plasma-bonded PDMS layers in the first stage to accommodate all the microchannels (Fig. 4-2(E) and Section A3.2 of Appendix 3). The devices were operated at an electric field of 80-200 V/cm to achieve rapid and efficient concentration of biomolecules (Section A3.3 of Appendix 3). During the transfer of biomolecules between stages, gravitational flows were superposed on the electroosmotic flows to increase the flow rates by adjustment of the heights of the outlet tubings (Section A3.4 of Appendix 3).

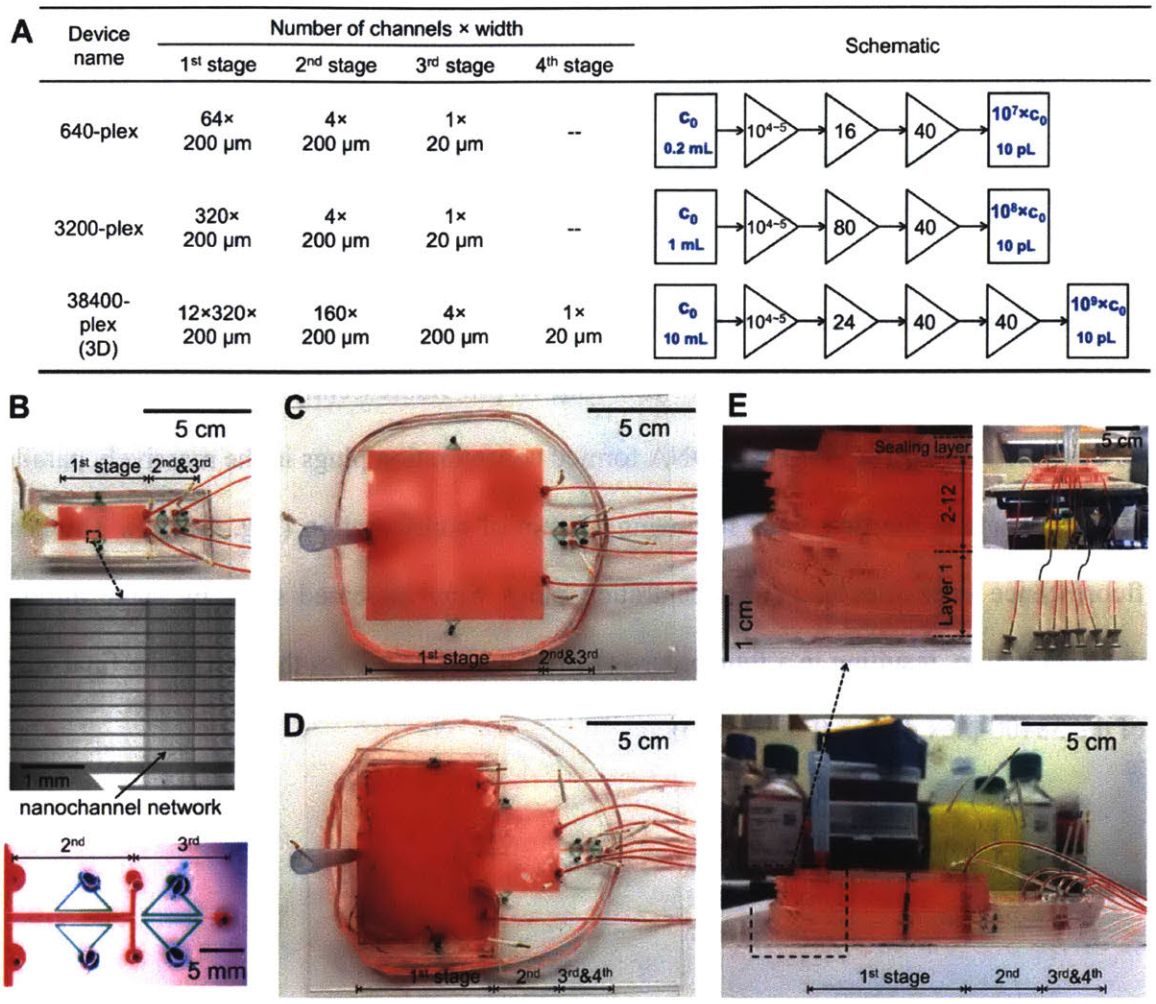


**Figure 4-2** Design of HOLMES devices. (A) The dimensions of the 640-, 3200-, and 38400-plex devices. The 640-, 3200-, and 38400-plex devices can concentrate biomolecules from 0.2, 1.0, 10.0 mL of samples (15 mM ion concentration) into a concentration zone of ~10 pL, corresponding to concentration factors of $10^7$, $10^8$, and $10^9$ based on mass conservation, respectively. (B) Photo of the 640-plex device fabricated by PDMS, micrograph of the first stage, and magnified view of the 2nd and 3rd stages. (C) Photo of the 32000-plex device. (D) Photo of the 38400-plex device. (E) Side view of the 38400-plex device, magnified view of

the vertically stacked multiple layers, and side view of the device showing the tubings of the side outlets turned on and off by the insertion and removal of push pins. In the photos, the devices were loaded with red food dye solution to better visualize the fluidic structures.

### 4.2 Enrichment performance of HOLMES

We visualized the workflow of HOLMES with 10 pM fluorescently labeled single stranded DNA (ssDNA) in 0.1×PBS. The ssDNA formed concentration plugs in the massively parallel microchannels in the first stage following 15 min of concentration (Fig. 4-3(A)). The peak fluorescence intensities of the concentration plugs were increased stage by stage through reconcentration, resulting in a four-orders-of-magnitude boost from the first to the final stage of the 38400-plex device (Fig. 4-3(B)).

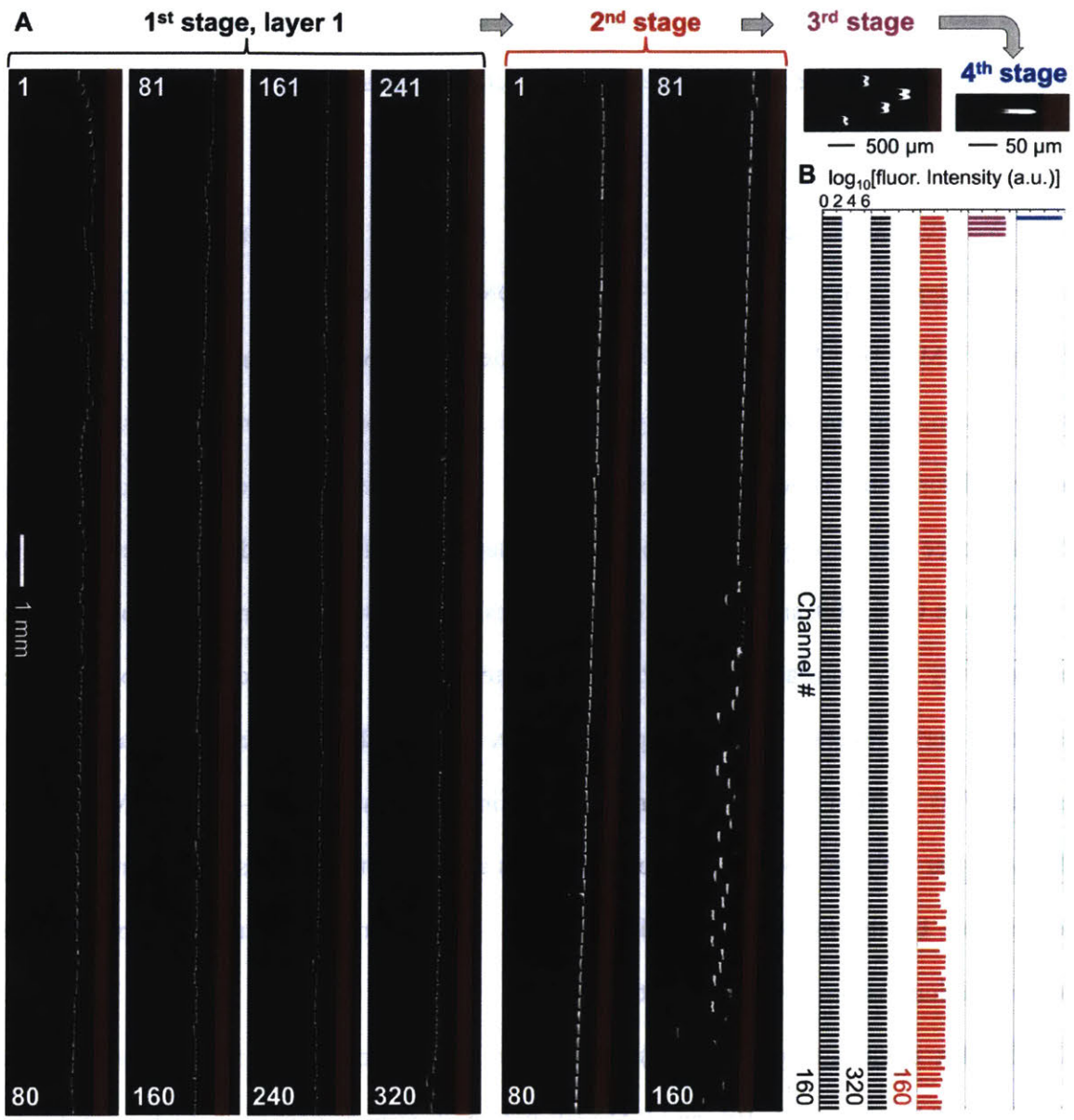


**Figure 4-3** Working process of HOLMES in a 38400-plex device. (A) The fluorescence images of the ssDNA concentration plugs in the parallel microchannels of different stages. Due to the limited field of view of the microscope, the fluorescence images were taken frame by

frame and stitched together. (B) The fluorescence intensities of the concentration plugs in individual microchannels of different stages, which increase stage by stage logarithmically.

We evaluated the concentration factors (ratio of peak concentration to initial concentration) achieved by HOLMES using ssDNA in 0.1×PBS with initial concentrations from $10^{-10}$ M to $10^{-17}$ M. The fluorescence intensities of the concentration plugs increased with time as concentration proceeded (Figs. 4-4(A-C)). While concentration plugs could only be observed for initial concentrations no less than 1 pM in the first stage (using conventional fluorescence microscopy), the reconcentration steps gradually lowered the detection limits, which were 1000, 100, and 10 aM at the final stages of the 640-, 3200-, and 38400-plex devices, respectively. By translating the fluorescence intensities to ssDNA concentrations using a standard curve (Section A3.5 of Appendix 3), we calculated the concentration factors at all stages (Figs. 4-4(D-F)). The concentration factor in the first stage was ~$10^4$ at 1 pM, which is higher (near $10^5$) for lower initial concentrations according to previous studies (not directly observable by the microscope used) [57], [76]. Subsequent reconcentrations boosted the concentration factors by approximately $3\times10^2$-, $10^3$-, and $10^4$-fold in the 640-, 3200-, and 38400-plex devices (Figs. 4-4(D-F)), leading to record-breaking maximum concentration factors of $0.76\times10^7$, $0.73\times10^8$, and $0.55\times10^9$ within 30 min, respectively. Tests with bovine serum albumin (BSA) suggest comparable concentration performance on proteins (Section A3.6 of Appendix 3).

We then amplified DNA solutions by the gold standard quantitative PCR (qPCR, amplicon length: 96 base pairs), which detected 10 aM as HOLMES did but took much longer time (75 min v.s. 30 min) (Fig. 4-4(G)). It is noteworthy that qPCR showed false positive in the no-template control because of non-specific amplification, while HOLMES was naturally immune to this problem as a non-amplification method. Furthermore, given the same total run time (not even counting the lengthy sample preparation time of qPCR), we compared the amplification/concentration factors of the two techniques (Fig. 4-4(H)). We calculated the amplification factor of qPCR based on ideal exponential duplication, and the concentration factor of HOLMES by varying the concentration time of the first stage and fixing the reconcentration protocol in the latter stages (Section A3.7 of Appendix 3). Overall, even excluding the sample preparation time of qPCR, HOLMES is still more efficient than qPCR where as high as billion-fold enrichment of nucleic acids is needed. Yet more crucially, HOLMES works on proteins while PCR does not.

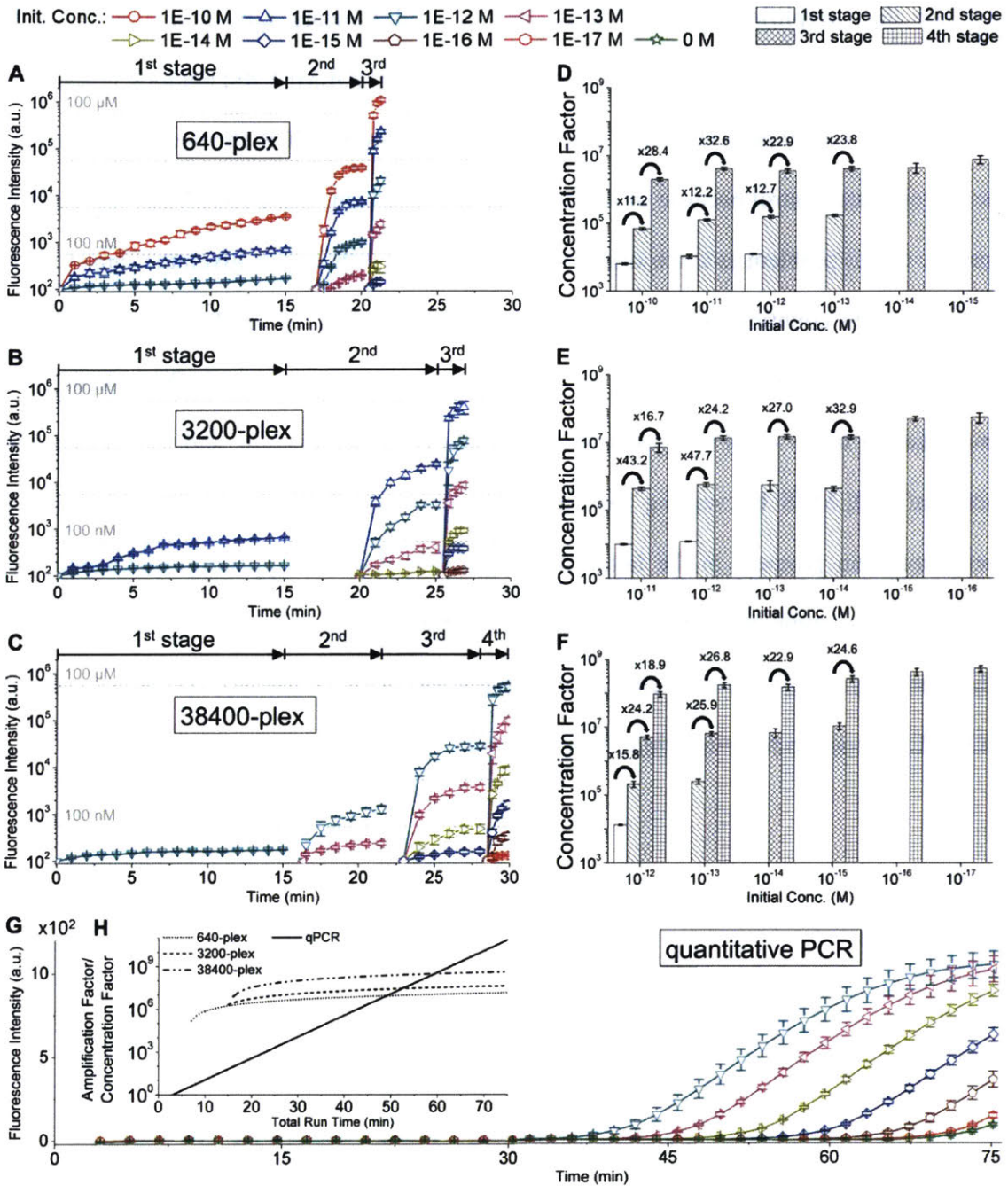
Init. Conc.: 1E-10 M 1E-11 M 1E-12 M 1E-13 M
1E-14 M 1E-15 M 1E-16 M 1E-17 M 0 M
1st stage 2nd stage
3rd stage 4th stage
A
1st stage
2nd
3rd
100 µM
640-plex
100 nM
Fluorescence Intensity (a.u.)
Time (min)
B
3200-plex
C
38400-plex
D
Concentration Factor
x11.2
x28.4
x12.2
x32.6
x12.7
x22.9
x23.8
Initial Conc. (M)
E
x43.2
x16.7
x47.7
x24.2
x27.0
x32.9
F
x15.8
x24.2
x18.9
x25.9
x26.8
x22.9
x24.6
G
x10^2
H
640-plex
3200-plex
38400-plex
qPCR
Amplification Factor/
Concentration Factor
Total Run Time (min)
quantitative PCR

**Figure 4-4** Enrichment performance of HOLMES. The temporal evolution of the average peak fluorescence intensities of the concentration plugs at the active stages in the (A) 640-, (B) 3200-, and (C) 38400-plex devices. Concentration factors at different stages and different initial concentrations in the (D) 640-, (E) 3200-, and (F) 38400-plex devices. During experiments, we imaged the microchannels at the center of the corresponding stages in one field of view of the microscope (12 microchannels in the first and second stages, and full views of the third and fourth stages). Only imaged microchannels were used for data processing. (G) The temporal evolution of fluorescence intensities in qPCR amplifying a DNA of the same intial concentrations (amplicon length: 96 base pairs). 2 μL sample is added into 20 μL reagent mixture for each reaction. (H) Comparison of the concentration factor of HOLMES and amplification factor of qPCR. Each data point represents the mean and standard deviation of triplicate runs.

## 4.3 Experimental section

### 4.3.1 Device fabrication

Device designs were patterned on 6-inch silicon wafers using SU-8 2015 photoresist (MicroChem, Westborough, MA). The thickness of the SU-8 patterns were ~15 μm. The patterned silicon wafers were treated with trichlorosilane (Sigma-Aldrich, St. Louis, MO) in a vacuum desiccator overnight to prevent adhesion to PDMS. (1) Fabrication of the 640- and 3200-plex devices. PDMS was poured onto the silicon mold and cured at 65°C for 3 hours. Then the PDMS was peeled off from the mold, and access holes were punched. The Nafion

nanochannel networks were patterned on a glass slide by the micro-flow patterning technique using Nafion resin (20 wt % solution in lower aliphatic alcohol/$H_2O$ mix, Sigma-Aldrich, St. Louis, MO) [34]. Finally, the microchannel-patterned PDMS and the nanochannel network-patterned glass slide were treated with oxygen plasma (Femto Science, Gyeonggi-Do, Korea), and irreversibly bonded under a stereo microscope. (2) Fabrication of the 38400-plex device. The 38400-plex device contained a bottom layer with all the four stages and eleven upper layers with only the first stage. The fabrication of the bottom layer was the same as that of the 640- and 3200-plex devices, except that connecting holes for upper layers were punched at the entrance of the $2^{nd}$ stage. The eleven upper layers were fabricated separately by the following process: PDMS was poured on the silicon mold and spin-coated at 200 rpm for 1 min (POLOS spin coater 150i, Germany), followed by heating at 120°C for 3 min; the cured PDMS was then peeled off from the mold (~1 mm thick); access holes and connecting holes to the bottom layers were punched on the PDMS; the nanochannel networks were patterned on a transparent silicone sheet (0.01 inch thick, Green Rubbers Company, Woburn, MA) by micro-flow patterning; the microchannel-patterned PDMS was bonded with the nanochannel network-patterned silicone sheet by oxygen plasma. After fabrication of the eleven layers, they were bonded onto the bottom layer one by one by oxygen plasma. The silicone sheets provided strong bonding between the PDMS layers. After fabrication of the devices, pellet Ag/AgCl electrodes (A-M systems, Sequim, WA) were inserted into all the reservoirs and Tygon non-DEHP microbore tubings were inserted into the outlets. Next, a sealing PDMS layer was bonded to the device to seal the outlets. Finally, uncured PDMS was poured on the sealing

layers near the electrodes and tubings as glue, followed by baking at 65°C for 1 hour to form tight sealing.

### 4.3.2 Device operation

Before all the experiments, the devices were passivated with 10 mg/ml BSA in PBS for 10 min and then flushed by PBS to prevent non-specific binding of biomolecules to the PDMS. A 22-base ssDNA (GTA GGC GAA CCC TGC CCA GGT C, labeled by Alexa Fluor 647 at 5') synthesized by Integrated DNA Technologies (Coralville, IA) was used to characterize the enrichment performance of HOLMES on nucleic acids. BSA (Sigma-Aldrich, St. Louis, MO) home-labeled by Alexa Fluor 555 was used to characterize the enrichment performance of HOLMES on proteins. The voltages at the inlet, buffer channels, and outlets were applied by a DC voltage source (Stanford Research Systems, Sunnyvale, CA) via a homemade voltage splitter. The gravitational flows were applied by controlling the hydrostatic pressures through adjusting the heights of the tubings. When a stage was in active concentration mode, its outlets were turned on and electrically grounded, and the corresponding buffer channels were electrically grounded; in other inactive stages, outlets were turned off and electrically floated, and the corresponding buffer channels were electrically floated. The operation flow was: concentration at the first stage, fast transfer of concentrated biomolecules to the entrance of the second stage by gravitational flow and electroosmosis, reconcentration at the second stage, and repeat until biomolecules were reconcentrated at the final stage. The operation sequences of the three devices were as follows: (1) 640-plex device: ($1^{st}$, 320 V, 0 Pa, 15 min), (transfer, 200 V, 1500 Pa, 2 min), ($2^{nd}$, 200 V, 0 Pa, 3 min), (transfer, 200 V, 1500 Pa, 0.5 min), ($3^{rd}$,

200 V, 0 Pa, 1 min). (2) 3200-plex device: ($1^{st}$, 640 V, 0 Pa, 15 min), (transfer, 200 V, 5000 Pa, 5 min), ($2^{nd}$, 200 V, 0 Pa, 5 min), (transfer, 200 V, 1500 Pa, 0.5 min), ($3^{rd}$, 200 V, 0 Pa, 1 min). (3) 38400-plex device: ($1^{st}$, 450 V, 0 Pa, 15 min), (transfer, 360 V, 5000 Pa, 1.5 min), ($2^{nd}$, 360 V, 0 Pa, 5 min), (transfer, 200 V, 5000 Pa, 1.5 min), ($3^{rd}$, 200 V, 0 Pa, 5 min), (transfer, 200 V, 1500 Pa, 0.5 min), ($4^{th}$, 200 V, 0 Pa, 1 min).

4.3.3 Fluorescence imaging and data analysis

Fluorescence images were acquired using an inverted fluorescence microscope (IX71, Olympus, Tokyo, Japan) and a CCD camera (Sensicam qe, Cooke Corporation, Romulus, MI). A mechanical shutter was used to reduce the photobleaching effect, which was synchronized with the CCD camera by Micromanager. The fluorescence images were analyzed by ImageJ. Because the pixel intensities of the fluorescence images had a range of 0-4095, which could only quantify fluorophore concentrations of three orders of magnitude. To quantify the nine-orders-of-magnitude concentrations without pixel saturation, we used 10 ms, 100 ms, 1000 ms, and 8000 ms exposure times depending on the concentrations of the fluorophores. In the processing of each image, after subtraction of the dark pixel intensity, the fluorescence intensity was normalized to an exposure time of 8000 ms based on the linear relationship between fluorescence intensity and exposure time [77]. Finally, to facilitate log-scale plotting, we added 100 a.u. to the fluorescence intensities of all data of log-scale plots.

4.3.4 qPCR

All the DNAs and reagents were ordered from Integrated DNA Technologies (Coralville, IA). The template was a 210-base-pair dsDNA with the sequence of CTG ATC CGG CCA CAG CCC GTC CCG CCG ATC TCG TCC AGC GCC GCT TCG GAC CAC CAG CAC CTA ACC GGC TGT GGG TAG CAG ACC TCA CCT ATG TGT CGA CCT GGG CAG GGT TCG CCT ACG TGG CCT TTG TCA CCG ACG CCT ACG CTC GCA GGA TCC TGG GCT GGC GGG TCG CTT CCA CGA TGG CCA CCT CCA TGG TCC TCG ACG CGA TCG. The sequences of the forward and reverse primers were GGACCACCAGCACCTAAC and GTAGGCGTCGGTGACAAA, respectively. The sequence of the probe was /6-FAM/TGT GGG TAG /ZEN/ CAG ACC TCA CCT ATG T/IABkFQ/, which was labeled by 6-FAM dye at 5', ZEN quencher in the middle, and IABkFQ quencher at 3'. The amplicon length was 96 base pairs. Each reaction was performed in 20 μL containing 500 nM primers, 250 nM probe, 1×MasterMix, and 2 μL template DNA solution. Each concentration of the template DNA was amplified in triplicates. The qPCR was performed with the Bio-Rad C1000 Thermal Cycler. The program of thermal cycling is 3 min initial heating, followed by 40 cycles of 16 s temperature ramp-up, 15 s denaturation at 95°C, 16 s temperature ramp-down, 60 s annealing and extension, and 10 s plate reading.

# Chapter 5 Integrated universal amplification-free molecular diagnostics using the next-generation biomolecule enrichment technique

Note: This Chapter is a partial direct reproduction of a previously published peer-reviewed journal paper (Wei Ouyang, and Jongyoon Han, Proceedings of the National Academy of Sciences Aug 2019, 116 (33) 16240-16249) with the permission of National Academy of Sciences. Appendix 3 is the supplementary information of this article.

So far, the engineered electrokinetic concentrator has realized the core functionality of the next-generation biomolecule enrichment technique – the capability of specifically enriching the Ab-bound target protein among the pool of background proteins by billion-fold and the cDNA-bound target DNA among the pool of background DNAs. Next, we will demonstrate the HOLMES as an integrated, stand-alone platform for universal amplification-free molecular diagnostics.

## 5.1 Nucleic acid detection by HOLMES

We went on to demonstrate that HOLMES could maintain high concentration performance in clinical samples and enable the detection of ultralow-abundance molecular biomarkers. In clinical samples, the much more abundant cell-free DNAs (*e.g.* ~100 ng/ml in human serum

[78]) and proteins (*e.g.* ~100 mg/ml in human serum [79]) would present significant noises for the sensitive and specific detection of targets and also suppress the concentration of targets (Section A3.8 of Appendix 3). HOLMES uses affinity probes to recognize the targets and modulate their electrophoretic mobility, which enables the selective enrichment of targets and simultaneous depletion of interfering background biomolecules.

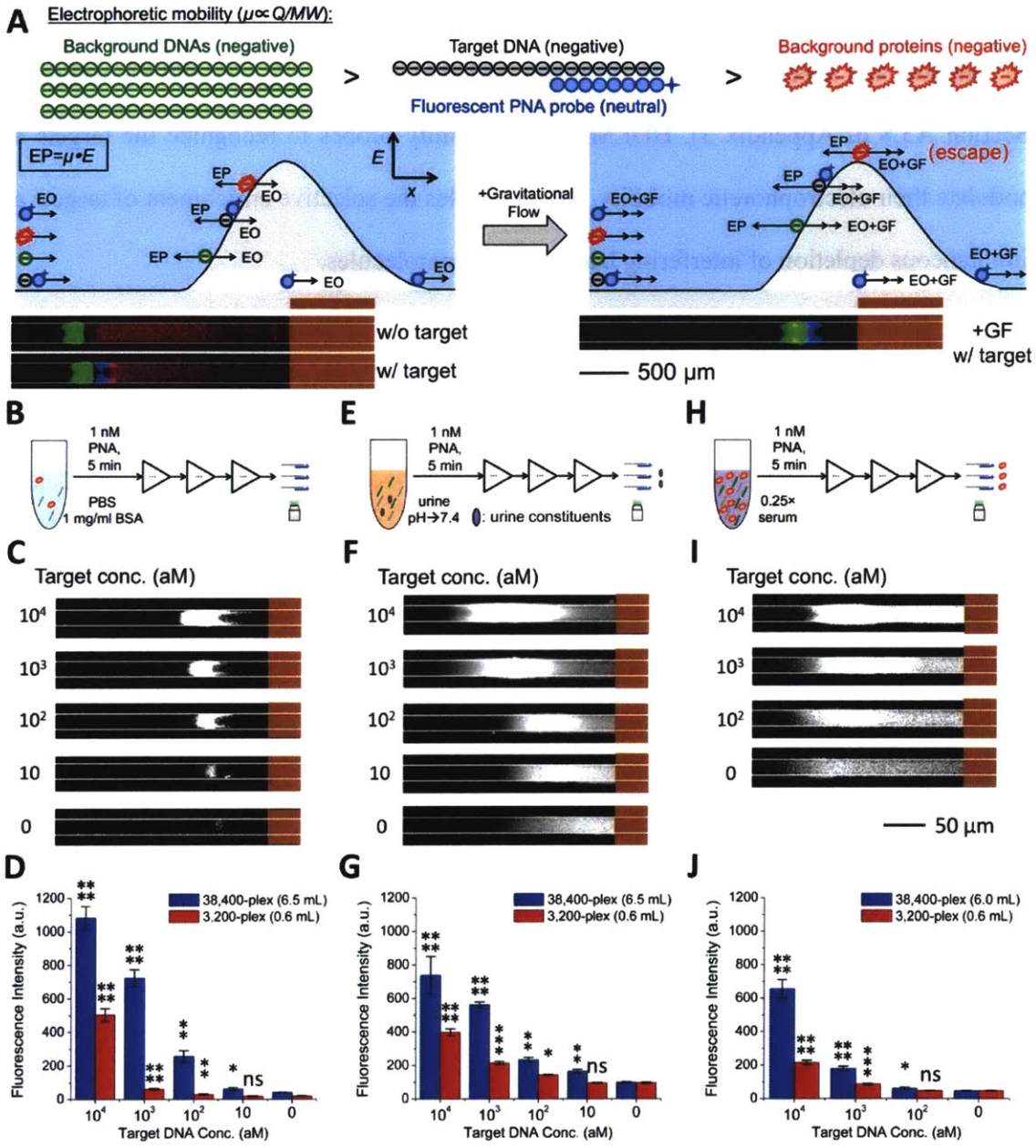


**Figure 5-1** Nucleic acid detection by HOLMES. (A) Schematic of selective nucleic acid enrichment. The concentration behaviors of biomolecules of different electrophoretic mobility within the electric field barrier are illustrated. The addition of gravitational flow enables

proteins to escape from the peak of the electric field barrier, thereby not being concentrated. The fluorescence images show concentration of 100 ng/ml fluorescently labeled DNA (green peak) and 10 mg/ml BSA (native fluorescence, red peak) in the detection of 1 nM target DNA by PNA (blue peak) in HOLMES. (B) Workflow, (C) fluorescence images, and (D) corresponding peak fluorescence intensities of DNA detection in PBS. (E) Workflow, (F) fluorescence images, and (G) corresponding peak fluorescence intensities of DNA detection in human urine. (H) Workflow, (I) fluorescence images, and (J) corresponding peak fluorescence intensities of DNA detection in human serum. Each data point represents the mean and standard deviation of triplicate runs. ns=not significant.

In nucleic acid detection, we used a fluorescently labeled complementary peptide nucleic acid (PNA) probe, which is a charge-neutral DNA analogue with higher affinity and specificity (even capable of distinguishing single-base mismatch) [80], [81]. The electrophoretic mobility of the hybridized DNA-PNA is between that of the background DNAs and proteins (Fig. 5-1(A)). The charge-neutral PNA probe is not subject to electric forces and hence directly passes the electric field barrier without being concentrated (not manifesting fluorescence), while the negatively charged DNA-PNA complex is concentrated (left panel, Fig. 5-1(A)), the fluorescence of which quantifies the concentration of the target DNA.

As previously mentioned, negatively charged biomolecules are concentrated where electrophoresis (velocity$\propto \mu \cdot E$, $\mu$ is electrophoretic mobility, $E$ is electric field) and electroosmosis are balanced. Because of the different mobility, the background DNAs, DNA-

PNA complex, and background proteins form separate concentration zones within the electric field barrier, with background proteins closest to the peak of the electric field barrier (left panel, Fig. 5-1(A)). By imposition of appropriate additional fluid drag force on the biomolecules with a pressure-driven flow (specifically, gravitational flow (GF) in this work), the total fluid drag force (EO+GF) exceeds the maximum electrophoretic force that can be exerted on the background proteins by electric field barrier (at its peak), thereby allowing the escape of the background proteins from the electric field barrier (right panel, Fig. 5-1(A)) [82]. Meanwhile, the total fluid drag force cannot overcome the maximum electrophoretic effect exerted on the background DNAs and DNA-PNA complex due to their higher mobility, which allows them to remain concentrated (right panel, Fig. 5-1(A)) [82]. By filtering out the background proteins and concentrating background DNAs in a separate zone, HOLMES could minimize the interference of background biomolecules. We visualized the selective enrichment using multi-wavelength fluorescence imaging with 100 ng/ml fluorescently labeled DNA (green peak) and 10 mg/ml BSA (native fluorescence, red peak) in the detection of 1 nM target DNA by PNA (blue peak). The left panel fluorescence images (Fig. 5-1(A)) indicate the co-concentration of different species in separate zones, and the right panel fluorescence image shows the filtration of proteins under an additional gravitational flow.

We demonstrate the detection of a fragment of M. tuberculosis IS6110 genomic DNA (96-base long) spiked in various biofluids under the selective enrichment mode (seeExperimental section and Section A3.9 of Appendix 3) [72], with sample-to-answer time of ~35 min. In PBS (Figs. 5-1(B-D) and Section A3.10 of Appendix 3), HOLMES was able to detect 100 aM target DNA from 0.6 mL samples using the 3200-plex device and 10 aM from

6.5 mL samples using the 38400-plex device. Urine contains few DNAs and proteins but many intrinsically fluorescent constituents (*e.g.* flavins, porphyrins, bilirubin) that are weakly charged [83]. These low-mobility fluorescent constituents were filtered like proteins, though trace remnants concentrating near the nanochannel network were observed under long exposure time (8000 ms) (Figs. 5-1(E-G) and Section A3.10 of Appendix 3). Nonetheless, HOLMES was able to distinguish 10 aM target DNA in urine, owing to the minimal interfering biomolecular background of urine. For samples in 0.25×serum (Figs. 5-1(H-J) and Section A3.10 of Appendix 3), we similarly observed the fluorescent peak of the DNA-PNA complex and remaining proteins near the nanochannel network. HOLMES was able to directly detect 100 aM target DNA in 0.25×serum.

### 5.2 Protein detection by HOLMES

Detection of ultralow-abundance protein biomarkers (<~1 fM or ~$10^{-4}$ ng/ml) in blood-derived samples below the currently clinically achieved level (~1 pM or ~$10^{-1}$ ng/ml) is of intense interests for the early diagnosis of diseases [1]. In protein detection, we used a high-mobility capture antibody (Ab) conjugated by fluorescently labeled ssDNAs (total length: 400 bases) and a capture Ab to capture the target protein, forming a DNA-Ab-target complex with higher mobility than the background proteins (Fig. 5-2(A)). Based on the mobility difference, the complex (and excess high-mobility capture Ab) could be selectively enriched under a gravitational flow. The selectively concentrated DNA-Ab-target complex was collected onto the surface of a microbead (diameter: 10 μm) via a detection Ab (Figs. 5-2(B-C)), which functioned as an additional mechanism of molecular enrichment and affinity recognition. After

washing out the excess capture Ab, the DNA-Ab-target-Ab sandwiches on the microbead were detected by fluorescence. We investigated the performance of the proposed assay by detecting the HIV p24 protein in the 3200-plex device, except that the microchannel in the final stage was widened to 100 μm to accommodate the microbead trapping structure. The assay was first performed without target concentration, which had a detection limit of 10 pM both in PBS with 10 mg/ml BSA and 0.25×serum (Fig. 5-2(D)). With target concentration from ~0.6 mL samples, fluorescence signals could be detected above the negative control for as low as 10 aM in PBS and 10-100 aM in 0.25×serum, which is nearly six-orders-of-magnitude enhancement over the assay without concentration. Compared to the gold standard ELISA (detection limit~1 pM) [7], HOLMES detected protein concentrations of about five-orders-of-magnitude lower with significantly shorter time (60 min v.s. several hours to over a day).

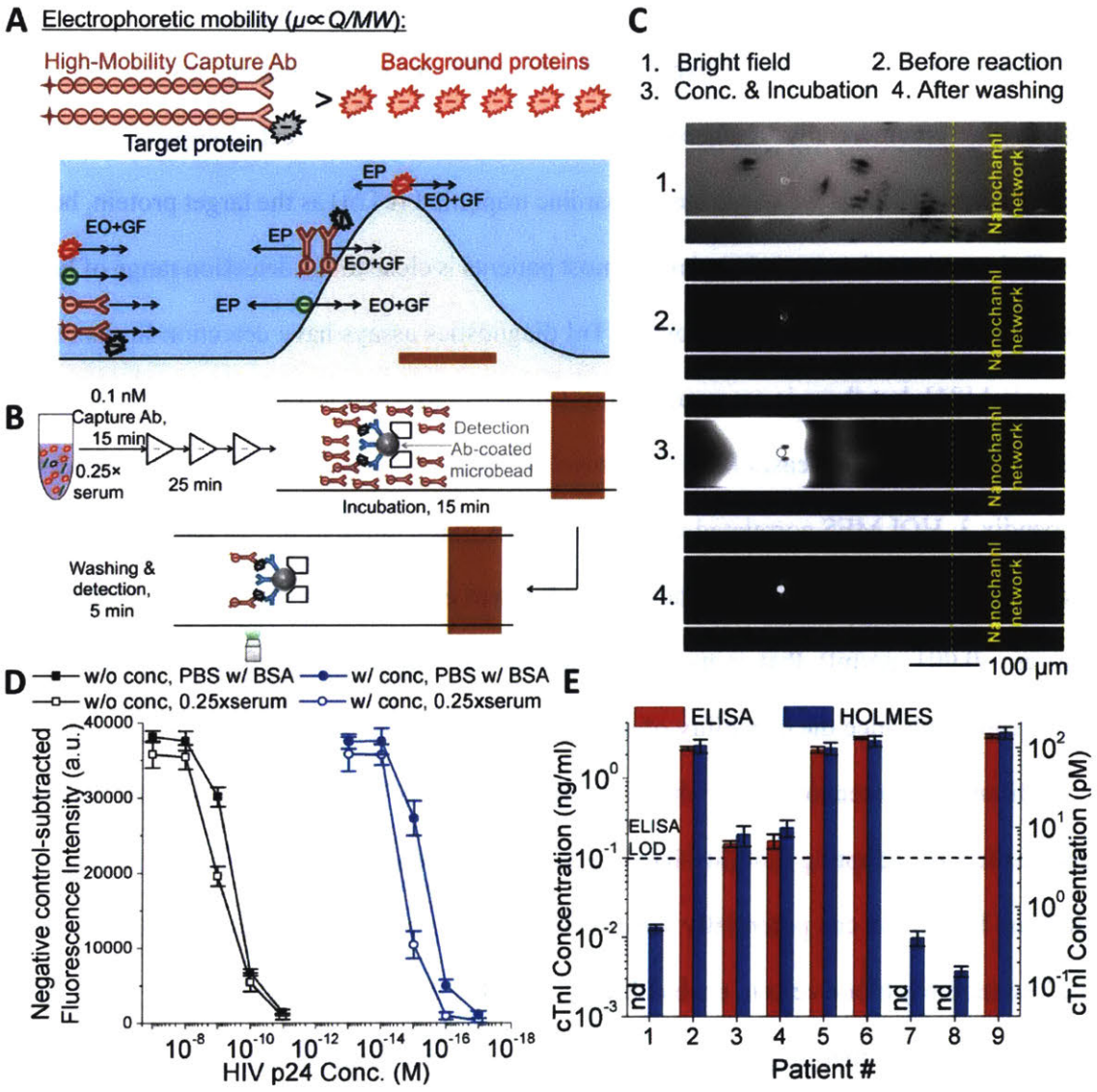


**Figure 5-2** Protein detection by HOLMES. (A) Schematic of selective protein enrichment in HOLMES. (B) Schematic and (C) micrographs of protein detection by HOLMES. (D) Detection of HIV p24 protein by HOLMES. (E) Correlation of HOLMES and ELISA in the detection of human cardiac troponin I in patient plasma samples. Each data point represents the mean and standard deviation of triplicate runs. LOD=limit of detection. nd=not detected.

Next, we validated the reliability of HOLMES by comparing its results with well-established commercially available ELISA. To enable the direct comparison between HOLMES and ELISA, we chose human cardiac troponin I (cTnI) as the target protein, because the cTnI concentration (pg/ml~ng/ml) in most patients is close to the detection range of ELISA. Most commercial ELISA kits and other cTnI diagnostics assays have detection limits of 0.01-0.1 ng/ml [84], but there is emerging interest in detecting even lower levels of cTnI for early prediction of cardiac diseases [85]. As shown in Fig. 5-2(E) and Sections A3.11 and A3.12 of Appendix 3, HOLMES correlated well with ELISA in the range of 0.1-10 ng/ml in 6 patients. Moreover, HOLMES was able to detect much lower concentrations of cTnI in 3 patients (as low as ~0.001 ng/ml) that were not detectable by ELISA. Therefore, HOLMES could significantly advance the capability of protein-based diagnosis.

Biomarker detection from whole blood is the focus of the next-generation molecular diagnostics. By adopting mobility-based selective enrichment demonstrated in this paper, we envision HOLMES can potentially selectively enrich high-mobility biomolecules and remove the low-mobility blood cells to enable direct biomarker detection in whole blood. Additionally, many current and emerging methods enable rapid and simple blood cell removal to reduce the interference of the high-density red blood cells (RBCs) on device operation. For example, RBC lysis can be performed on whole blood (taking <1 min using saponin [86]) before it is loaded into the device, after which biomolecules of interest are selectively enriched and protein released from RBCs (hemoglobin) is filtrated by HOLMES (as shown in this paper). Therefore,

our system can still be readily applied to whole-blood biomarker detection with minor modification/sample preparation.

## 5.3 Summary

In this chapter, we have demonstrated that HOLMES achieves billion-fold enrichment of nucleic acids and proteins within 30 min and enables direct detection of attomolar biomolecules in clinical samples within an hour with minimal sample preparation. HOLMES may significantly advance molecular diagnostics in comparison with the state of the art: (1) PCR requires stringent and complex isolation and purification of nucleic acids, and the amplification process is subject to many pitfalls previously mentioned. HOLMES directly enriches nucleic acids in clinical samples by selectively collecting them into a microfluidic space, which greatly simplifies the workflow and avoids many issues of PCR. Remarkably, HOLMES naturally enables unbiased enrichment of multiple sequences, which is very important in nucleic acid studies but highly challenging for PCR. (2) In the domain of protein analysis, HOLMES is in an unparalleled position, which is the only technique providing PCR-comparable performance for proteins. Not being able to amplify proteins, the gold standard ELISA and other signal amplification-based protein assays do not essentially solve the challenges in detecting ultralow-abundance proteins. With unprecedented capability of enriching proteins by billion-fold, HOLMES may unleash rapid and ultra-sensitive protein analysis that had not been possible.

We would like to clearly express that we are not competing with the exciting developments of nanoscale biosensors and novel diagnostic platforms like CRISPR-based

diagnostics [87], but we are complementary to them. By solving the fundamental problems of slow mass transport and weak reaction kinetics in the detection of ultralow-abundance molecular biomarkers and removing the interfering strong background noises in biofluids, HOLMES can be universally integrated with nanoscale biosensors to significantly enhance their detection sensitivity and improve the speed and statistical reliability of detection. Similarly, for diagnostic platforms like CRISPR that rely on chemical amplification, HOLMES can play an important role in avoiding the common pitfalls of chemical amplification. HOLMES could also have far-reaching impacts on many fields of biological science and engineering to meet the ubiquitous needs of sensitive and accurate biomolecule analysis, such as genetic studies, sequencing, mass spectrometry, proteomics, and biomarker discovery.

## 5.4 Experimental section

### 5.4.1 Selective enrichment mode

The operation protocols of the selective concentration mode were the same as those described in the Device operation section, except that gravitational flows were added in the concentration steps to "push" proteins across the electric field barrier. The operation sequences of the three devices under the selective concentration mode were as follows: (1) 640-plex device: ($1^{st}$, 320 V, 450 Pa, 15 min), (transfer, 200 V, 1500 Pa, 2 min), ($2^{nd}$, 200 V, 300 Pa, 3 min), (transfer, 200 V, 1500 Pa, 0.5 min), ($3^{rd}$, 200 V, 240 Pa, 1 min). (2) 3200-plex device: ($1^{st}$, 640 V, 900 Pa, 15 min), (transfer, 200 V, 5000 Pa, 5 min), ($2^{nd}$, 200 V, 300 Pa, 5 min), (transfer, 200 V, 1500 Pa, 0.5 min), ($3^{rd}$, 200 V, 240 Pa, 1 min). (3) 38400-plex device: ($1^{st}$, 450 V, 600 Pa, 15

min), (transfer, 360 V, 5000 Pa, 1.5 min), (2nd, 360 V, 500 Pa, 5 min), (transfer, 200 V, 5000 Pa, 1.5 min), (3rd, 200 V, 315 Pa, 5 min), (transfer, 200 V, 1500 Pa, 0.5 min), (4th, 200 V, 290 Pa, 1 min). Due to the high viscosity of serum, the hydrostatic pressures were increased for selective enrichment in serum: (1) 640-plex device: (1st, 320 V, 550 Pa, 15 min), (transfer, 200 V, 1800 Pa, 2 min), (2nd, 200 V, 375 Pa, 3 min), (transfer, 200 V, 1800 Pa, 0.5 min), (3rd, 200 V, 300 Pa, 1 min). (2) 3200-plex device: (1st, 640 V, 11000 Pa, 15 min), (transfer, 200 V, 6000 Pa, 5 min), (2nd, 200 V, 375 Pa, 5 min), (transfer, 200 V, 1800 Pa, 0.5 min), (3rd, 200 V, 300 Pa, 1 min). (3) 38400-plex device: (1st, 450 V, 750 Pa, 15 min), (transfer, 360 V, 6000 Pa, 1.5 min), (2nd, 360 V, 625 Pa, 5 min), (transfer, 200 V, 6000 Pa, 1.5 min), (3rd, 200 V, 400 Pa, 5 min), (transfer, 200 V, 1800 Pa, 0.5 min), (4th, 200 V, 330 Pa, 1 min).

5.4.2 Nucleic acid detection

The sequence of the target DNA was CGA GCG TAG GCG TCG GTG ACA AAG GCC ACG TAG GCG AAC CCT GCC CAG GTC GAC ACA TAG GTG AGG TCT GCT ACC CAC AGC CGG TTA GGT GCT GGT (Integrated DNA Technologies, Coralville, IA). The sequence of the PNA probe was TCA CCT ATG TGT CGA ACT GG with 5' labeled by Cy5 dye (PNA Bio, Newbury Park, CA). Pooled human urine was ordered from Lee BioSolutions (Maryland Heights, MO). The pH of the urine was adjusted to 7.4 using 1 M sodium hydroxide (Sigma-Aldrich, St. Louis, MO). Human serum was ordered from Millipore Sigma (Burlington, MA). Different concentrations of the target DNA were spiked into PBS with 10 mg/ml BSA, urine, and 0.25×serum (diluted by PBS). The PNA probe was added to the samples to a final concentration of 1 nM, followed by 5 min incubation. Next, the samples were processed by the

devices under the selective concentration mode, which took about 30 min. Finally, fluorescence images of the microchannels of the final stages were taken and analyzed. Each sample was tested three times using three devices.

5.4.3 DNA-antibody conjugation

The ssDNA was 96-base long with the sequence of AGC TAG CTA GCT AGC TAG CTA GCT AGC TAG CTA GCT AGC TAG CTA GCT AGC TAG CTA GCT AGC TAG CTA GCT AGC TAG CTA GCT AGC TAG CTA GCT AGC TAG CTA GCT, which was labeled with an amine group at 5' and a 6-FAM dye at 3'. The manufacturer of the capture antibody is described in the Protein detection section. The conjugation kit was ordered from SoluLink (San Diego, CA). Basically, the amine-DNA was modified with succinimidyl-4-formylbenzamide (S-4FB) crosslinker, and the capture antibody was modified with succinimidyl 6-hydrazinonicotinate acetone hydrazone (S-HyNic) crosslinker, which were finally linked by the crosslinker pair. The DNA was resuspended to a concentration of 0.5 $OD_{260}/\mu L$, mixed with S-4FB at a 1:20 molar ratio, and incubated for 2 hours. The mixture was purified with the Zeba desalting column (Thermo Fisher Scientific, Waltham, MA) three times to remove excess free S-4FB. The capture antibody was reconstituted to 1 mg/ml in PBS, mixed with S-HyNic at a 1:20 molar ratio, and incubated for 2.5 hours. The mixture was purified with the Zeba desalting column three times to remove excess free S-HyNic. The S-HyNic-modified antibody and S-4FB-modified DNA were mixed at a molar ratio of 1:7. 1/10 volume of TurboLink catalyst (SoluLink, San Diego, CA) was added to the mixture. The mixture was then incubated overnight. Finally, the mixture was purified to remove excess DNA and exchanged to PBS buffer using the Zeba desalting

column. The resulted DNA-antibody conjugate contained approximately four DNA molecules on one antibody molecule.

### 5.4.4 Microbead functionalization and trapping

The SuperAvidin™-coated microbead (10 μm in diameter) was ordered from Bangs Laboratory (Fishers, IN). The manufacturer of the detection antibody is described in the Protein detection section. 5 μL microbead suspension (10 mg/ml) was washed in PBS three times by centrifugation at 2500 g for 5 min. The detection antibody was biotinylated with EZ-Link™ NHS-PEG4-Biotin (Thermo Fisher Scientific, Waltham, MA). 10 μL 1 mg/ml biotinylated antibody was mixed with the washed microbeads, and incubated on a rotator for 15 min at room temperature. Finally, the microbeads were washed in PBS five times by centrifugation at 2500 g for 5 min to remove excess antibodies. The antibody-coated microbead suspension was stored at 1 mg/ml at 4°C and used within three days. Upon experiments, 2 μL microbead suspension was diluted by 1000 times in PBS. The diluted microbead suspension was pipetted into the microchannel of the final stage through the final outlet. Then a syringe was used to suck the microbead suspension back to the final outlet, during which the microbeads back-flowed and one microbead became trapped between the PDMS pillars. Finally, PBS was loaded into the device through the main inlet to wash excess microbeads remaining in the final stage.

### 5.4.5 Protein detection

The HIV p24 antibody pair and recombinant HIV p24 protein were from the HIV-1 Gag p24 DuoSet ELISA kit (R&D Systems, Minneapolis, MN). The Magic™ human cTnI antibody

pair (Creative Diagnostics, Shirley, NY) was used for the detection of cTnI (clone TPC102 as the capture antibody and clone TPC110 as the detection antibody). Recombinant human cTnI protein was ordered from Abcam (Cambridge, MA). (1) HIV p24 detection: different concentrations of recombinant HIV p24 protein were spiked into PBS with 10 mg/ml BSA and 0.25×serum (diluted by PBS). The DNA-conjugated high-mobility capture antibody was added to the samples to a final concentration of 0.1 nM, followed by 15 min incubation. Next, the samples were processed by the 3200-plex device under the selective concentration mode, which took about 25 min. The DNA-capture Ab-p24 complex was concentrated in a region trapped with a detection Ab-coated microbead. The voltage was turned off and the final outlet was turned off, such that the concentration plug remained in the microbead-trapped region. After 15 min of incubation, the final outlet was turned on and the concentration plug was washed out. Finally, fluorescence images of the microbead were taken and analyzed. Each sample was tested three times using three devices. (2) cTnI detection: The standard curve of cTnI detection in the 3200-plex device was established following the same protocol as HIV p24 detection. The nine patient plasma samples for cTnI detection were de-identified diagnostic remnants ordered from Discovery Life Sciences (Los Osos, CA), which were collected through HHS/OHRP and HIPAA-compliant practices.

### 5.4.6 ELISA

All the materials and reagents (except antibodies and protein standard) were from the DuoSet® Ancillary Reagent Kit 2 (R&D Systems, Minneapolis, MN). The reagent diluent was PBS with 10 mg/ml BSA and 0.2% Triton™ X-100. The washing buffer was PBS with 0.05% Tween

20. The working concentrations of the capture antibody and detection antibody were 2 μg/ml (in PBS) and 100 ng/ml (in reagent diluent), respectively. The samples were diluted by 4 times in the reagent diluent. 100 μL capture antibody solution was loaded into each well of the 96-well microplate and incubated overnight at room temperature. Then each well was washed with 400 μL washing buffer for three times, followed by blocking with 300 μL reagent diluent for 1 hour. After washing of the microplate as previously mentioned, 100 μL sample or standard solution was loaded into each well, and incubated for 2 hours. After washing, 100 μL detection antibody solution was loaded into each well and incubated 2 hours at room temperature. After washing, 100 μL streptavidin-horseradish peroxidase conjugate (40-fold diluted from stock) was loaded into each well and incubated 20 minutes at room temperature. After washing, 100 μL substrate solution ($H_2O_2$ and tetramethylbenzidine mixture) was loaded into each well and incubated 20 minutes at room temperature. Finally, 50 μL stop solution (2N $H_2SO_4$) was loaded into each well and thoroughly mixed. Finally, the absorbance of the wells was measured by a microplate reader (Varioskan Flash Spectral Scanning Multimode Reader, Thermo Fisher Scientific) at 450 nm.

# Chapter 6 Interfacing the next-generation biomolecule enrichment technique with standard analytics

Note: Section 6.1 is a direct reproduction of a journal paper under peer review (Wei Ouyang, and Jongyoon Han, "Microfluidic-Integrated One-Step Nucleic Acid Purification and Noise-Resistant PCR by Hierarchical Selective Electrokinetic Concentration for Ultralow-Abundance Nucleic Acid Detection").

Hierarchical selective electrokinetic concentration owns the unique capability of specifically enriching the target biomolecules by billion-fold and simultaneous removal of background biomolecules, thereby greatly enhancing the signal-to-noise ratio for downstream analytics. This technique not only can be a self-contained, stand-alone platform for molecular diagnostics as described in Chapter 5, but also may, in whole or in part, serve as a sample preparation module for standard analytics. Examples of commonly used standard analytics are mass spectrometry, microarray, next-generation sequencing, quantitative PCR (qPCR), surface plasmon resonance, high-performance liquid chromatography, and capillary electrophoresis. Going beyond simply measuring the abundance of a small number of biomolecular biomarkers (as in molecular diagnostics), standard analytics provides comprehensive analyses of both the single biomolecule properties (*e.g.* affinity, size, oxidation, methylation, phosphorylation, glycosylation) and collective signatures of biofluids/biomolecule mixtures (*e.g.* genome, proteome, transcriptome, peptidome) for system-level understanding of the human body, which are not likely to be achieved by lab-on-a-chip devices in the near future. Aside from its

unprecedented capability of target enhancement and background depletion for the enhancement of the sensitivity and specificity of standard analytics, the values of the electrokinetic concentrator in sample preparation for standard analytics also lie in its simple device fabrication, ease of operation, and short operation time in achieving this capability, which may greatly simplify the workflow of standard analytics.

In this chapter, we will describe the interfacing of the electrokinetic concentrator with two standard analytical techniques: (1) qPCR, which is conventionally used more than just as an amplification technique but also as analytics for nucleic acid quantitation; (2) The NanoString nCounter® for high-throughput quantitation and profiling of nucleic acids of interest.

### 6.1 Interfacing with qPCR

Nucleic acid amplification tests (NAATs) play a crucial role in the analysis of low-abundance nucleic acids (NAs) for early diagnosis of diseases [7], [88], [89]. NAATs mainly rely on the gold-standard polymerase chain reaction (PCR) [90], though emerging isothermal amplification techniques like loop-mediated isothermal amplification (LAMP) [8] and recombinase polymerase amplification (RPA) [91] have attracted increasing interests [89]. Despite being highly powerful, NAATs generally suffer from the following major issues. (1) Lengthy design and optimization: Non-specific amplification is the most common problem that persists in NA amplification. A major source of non-specific amplification is the primer dimerization and subsequent elongation due to non-optimal primer design, reagent composition, and reaction conditions (*e.g.* temperature) [92]–[94]. It often takes iterative optimizations to eliminate primer dimers, which is particularly challenging and lengthy for

isothermal amplification techniques because of the low amplification temperatures that favor primer dimerization and the less established design methodologies [89], [95], [96]. (2) Complex workflows: Before amplification, NAs typically need to be extracted and stringently purified to remove amplification inhibitors (*e.g.* proteins and salts) from clinical samples, which is especially important for PCR. The mainstream technique for NA purification is the solid phase extraction (SPE), in which NAs are captured by silica membranes using chaotropic salts, washed with ethanol, and finally eluted from silica membranes (Fig. 6-1(a)) [97]–[99]. SPE is complex, time-consuming, labor-intensive, and relies on equipment and amplification-inhibitive chemicals. Moreover, SPE has limited recovery efficiency and is susceptible to cross-contamination, which limits the sensitivity and specificity of detection.

Fully integrated NAATs on microfluidic chips with sample-to-answer capability have attracted significant interests in recent years, which can potentially be implemented at the point of care without the need for trained personnel and centralized labs [90], [100]–[105]. However, existing works toward fully integrated NAATs still have several major limitations. First, the amplification chemistry for integrated NAATs is typically obtained following the design and optimization processes for bench-top NAATs, which is too lengthy and sophisticated for emergency situations (*e.g.* outbreaks of new pathogens) and point-of-care applications. Second, on-chip NA purification still relies on the SPE following the bind-wash-elute procedure (in a miniaturized format), which requires complicated fluidic/valving structures and complex operation protocols [97], [106]–[109]. The dependence on miniaturized SPE makes NAATs difficult to automate, time-consuming, and less robust. Alternatively, isotachophoresis (ITP) has been demonstrated as a non-solid-phase method for NA purification with simpler

operations [110], [111], which, however, has rarely been interfaced with on-chip NA amplification for fully integrated NAATs. Third, the miniaturization of NAATs on microfluidic chips is often accompanied by the significant decrease of sample processing throughput (<10 μL) [90], which disallows the capture of sufficient copies of ultralow-abundance NAs (<1 copy/μL) [112] for subsequent detection, thereby fundamentally limiting the detection sensitivity. Taken together, in order to detect ultralow-abundance NAs rapidly and reliably, it is important to develop integrated NAATs with short design cycles, simple NA purification methods, and high sample processing throughputs.

Here we report an integrated NAAT using hierarchical selective electrokinetic concentration with three key features: one-step NA purification, high sample processing throughputs, and PCR resistant to non-specific amplification ("noise-resistant") even with non-optimal designs. First, we realize one-step NA purification using selective electrokinetic (EK) concentration. In an EK concentration device, biomolecules are electroosmotically injected into a microfluidic channel and subsequently trapped by the locally amplified electric field in the ion depletion zone induced by an ion-selective membrane, leading to the continuous stacking/concentration of biomolecules [22], [24], [41], [69], [113], [114]. More recently, we demonstrated selective EK concentration by superposing an appropriate pressure-driven flow with electroosmosis, which enabled proteins (low electrophoretic mobility) to escape the ion depletion zone yet still kept NAs (high electrophoretic mobility) trapped, thereby selectively concentrating NAs [82]. In this work, we propose that selective EK concentration can be used as "EK purification" to purify NAs and effectively remove unwanted biochemical species for subsequent PCR. Compared to the conventional bind-wash-elute approach, EK purification is

a liquid-phase, physical method performed in one step by simply applying a DC voltage and a hydrostatic pressure, eliminating the needs for complex device design, multi-step operations, and PCR-inhibitive chemicals. Compared to ITP in which NAs continuously drift along the microfluidic channels, EK purification is a drift-less (or minimally drifting) method in which NAs are localized in the microfluidic channels and easily manipulated for subsequent amplification. Second, we achieve high sample processing throughputs by massive parallelization of electrokinetic concentrators, which can process 0.1-10 mL samples in 15 min depending on the number of parallel concentrators as we demonstrated recently [115]. Third, we use a hierarchical electrokinetic concentration architecture to re-concentrate purified NAs from massively parallel concentrators into a single concentrator, which are subsequently delivered into a microfluidic chamber for PCR. By concentrating NAs and performing PCR in a microfluidic chamber with a small volume of reagents (~0.1 μL), we keep the same number of the target template but dramatically decrease the number of primer dimers compared to that in conventional tube-based PCR (~20 μL), thereby greatly enhancing the signal-to-noise ratio. Also, increasing the concentration of the target template will exhaust the reagents at earlier cycles, thereby suppressing the amplification of primer dimers that typically occur at large cycle numbers. In sum, by combining hierarchical selective EK concentration and microfluidic PCR (HSEC-PCR) as shown in Fig. 6-1(b), we can create an integrated NAAT platform with one-step NA purification and noise-resistant PCR for the rapid and reliable detection of ultralow-abundance NAs. By testing spiked *M. tuberculosis* (MTB) genomic DNA in human urine and serum, we demonstrate that HSEC-PCR achieved a detection limit of 5 target DNA copies, which was better than the 50 copies achieved by the standard method using bench-top

SPE and PCR. In the case of non-optimal PCR designs, we demonstrate the suppression of non-specific amplification in HSEC-PCR, which enhanced the detection limit by three orders of magnitude compared to that of the standard method. This platform solves the universal limitations of NAATs, which can be directly used for isothermal amplifications and other amplification techniques.

### 6.1.1 Design of the HSEC-PCR device

Fig. 6-1(c) and Fig. 6-1(d) show the schematic and photo of the HSEC-PCR device, respectively. The device consists of two stages. In the first stage, there are 64 parallel microchannels (200 μm wide) and 1 buffer channel (200 μm wide) on each side, all of which are 13 μm deep. A cation-selective Nafion membrane strip (~1 μm thick) patterned on the glass slide crosses the microchannels perpendicularly at the bottom of the microchannels, which is used to generate the EK concentration effect under an appropriate DC voltage configuration. The right end of the first stage has 1 microchannel in the middle connecting to the second stage and 2 outlets. The second stage consists of 1 microchannel of 800 μm wide and 13 μm deep, 1 PCR chamber of 1 mm long, 1 mm wide, and 80 μm deep, and 1 Nafion membrane strip for the generation of the EK concentration effect. Having a deep PCR chamber is important for reducing the water evaporation through the highly permeable PDMS, owing to the lower surface-area-to-volume ratio than a shallow PCR chamber [116]. Four pneumatic valves are used for the manipulation (isolation, transfer, and mixing) of the concentrated NAs. Fig. 6-1(e) shows the device placed on the MiniPCR™ thermal cycler during qPCR. Figs. 6-1(f)-(h) show the bright-field micrographs of the first stage, intersection between the first and second stages,

and the second stage, respectively. Supporting pillar arrays are used to prevent the collapsing of the microfluidic channels.

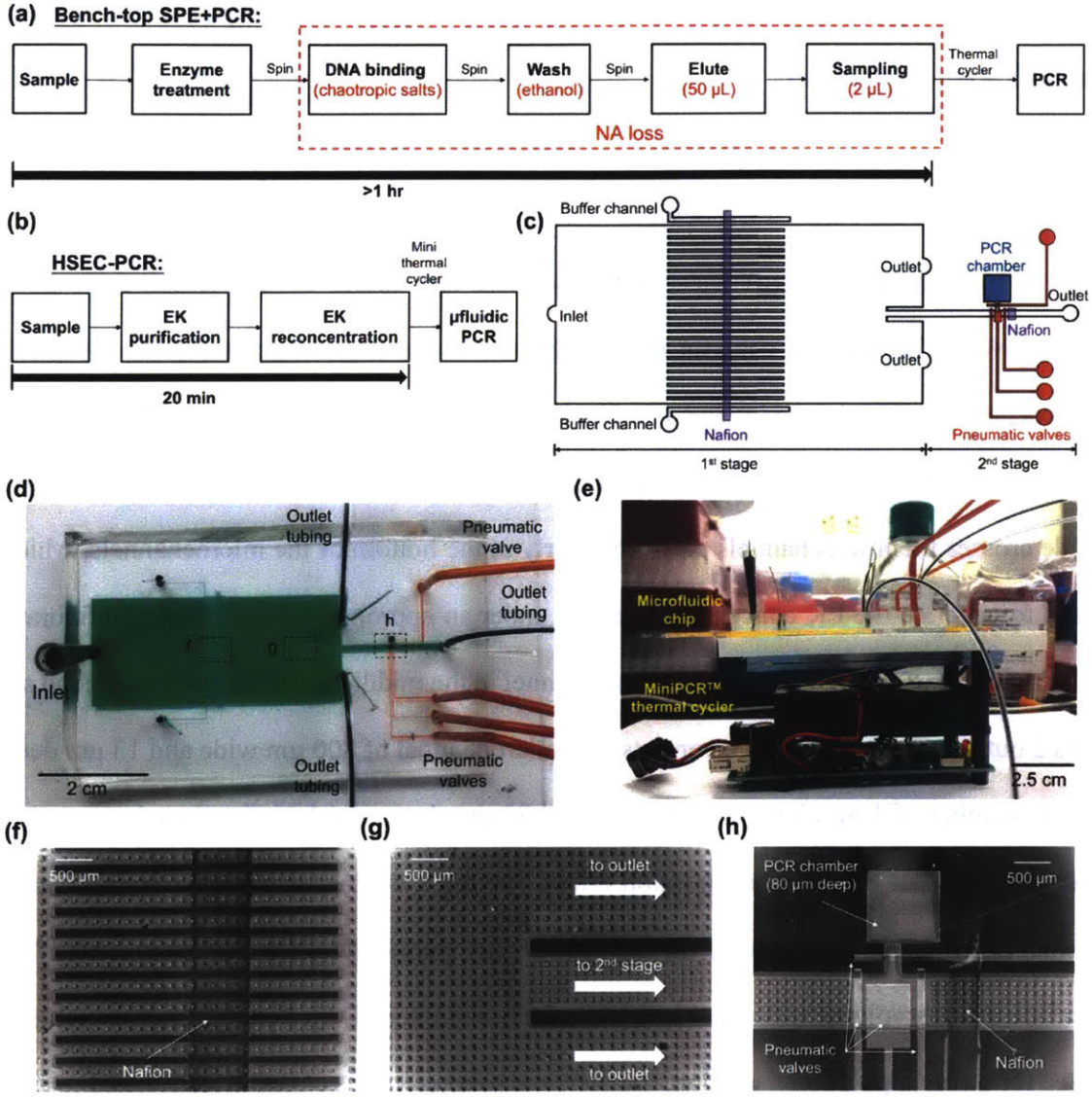


**Figure 6-1** Schematic and photos of the HSEC-PCR device. (a) Workflow of the standard bench-top SPE+PCR. (b) Workflow of HSEC-PCR. (c) Schematic of the HSEC-PCR device.

(d) Photo of the HSEC-PCR device. (e) Photo of the device placed on the MiniPCR$^{TM}$ thermal cycler. (f) Micrograph of the first stage. (g) Micrograph of the intersection between the first and second stages. (h) Micrograph of the second stage.

### 6.1.2 Principle and operation procedures of HSEC-PCR

Fig. 6-2 shows the principle and operation procedures of HSEC-PCR. In EK purification, the inlet is set to a positive voltage $V$, and the outlets and side buffer channels are grounded. A hydrostatic pressure $P$ is applied by the control of the liquid level difference between the inlet and outlet tubings [82]. The principle of EK purification is explained as follows. Under the aforementioned electrical configuration, the electric potential difference between the parallel microchannels and the side buffer channels induces selective transport of cations through Nafion from the parallel microchannels to the side buffer channels, leading to the generation of ion depletion zones in the parallel microchannels near Nafion (left side). The electric field is significantly amplified in the ion depletion zone, which functions as an electric force barrier (Fig. 6-2(a)). The biomolecules (mainly NAs and proteins) enter the microchannels with the fluid flow induced by electroosmosis (EO) and pressure-driven flow (PDF) [32], which has a velocity of $v_{EO} + v_{PDF}$ (rightward). At the same time, biomolecules are subject to an electrophoretic force that generates an electrophoresis (EP) velocity of $v_{EP} = \mu \cdot E$ (leftward), where $\mu$ is the electrophoretic mobility of the biomolecules and $E$ is the amplitude of electric field. The biomolecules continuously enter the microchannels because $v_{EO} + v_{PDF} > v_{EP}$ in the bulk of the microchannels. As the biomolecules enter the ion depletion zones with the

amplified electric field, $v_{EP}$ gradually increases with $E$ until it becomes as great as $v_{EO} + v_{PDF}$ ($v_{EO} + v_{PDF} = v_{EP}$), leading to the electrokinetic trapping and continuous stacking of the biomolecules, i.e. the EK concentration effect. However, if the maximum $v_{EP}$ in the ion depletion zones (at the peak of the electric force barrier $E_{max}$) is still less than $v_{EO} + v_{PDF}$, i.e. $v_{EO} + v_{PDF} > v_{EP\_max} = \mu \cdot E_{max}$, the biomolecules will overcome the electric force barrier and not be concentrated. Given that the electrophoretic mobility of NAs is much greater than that of proteins (and other unwanted biochemical species) ($\mu_{NA} \gg \mu_{protein}$) [31], [111], it can be satisfied that $v_{EP\_max}(NA) > v_{EO} + v_{PDF} > v_{EP\_max}(protein)$ by appropriate modulation of the pressure-driven flow ($v_{PDF}$), thereby only concentrating NAs and simultaneously removing proteins. We optimized the conditions of EK purification by using human urine spiked with 100 nM Alexa Fluor 647-labeled DNA as the sample. The native fluorescence of proteins and metabolites in urine can be imaged using the green fluorescence setup (excitation wavelength ~490 nm) at a long exposure time of 1000 ms. A voltage of 250 V was applied to the device. As shown in Fig. 6-2(a) (right), both the DNA (shown in green) and proteins and metabolites (shown in red) were concentrated under a zero hydrostatic pressure; however, only the DNA was concentrated and the proteins and metabolites were removed under a hydrostatic pressure of 400 Pa, which was the condition used for subsequent experiments.

As shown in Fig. 6-2(b), after EK purification, the outlets of the first stage are closed, and that of the second stage is opened and grounded. The conditions of the inlet remain $V$=250 V and $P$=400 Pa. Under this configuration, the NAs concentrated in the parallel microchannels in the first stage are flushed toward the second stage, and reconcentrated near the Nafion in the

second stage. Finally, the reconcentrated NAs are isolated by the pneumatic valves and transferred into the PCR chamber (pre-loaded with PCR reagents) for amplification.

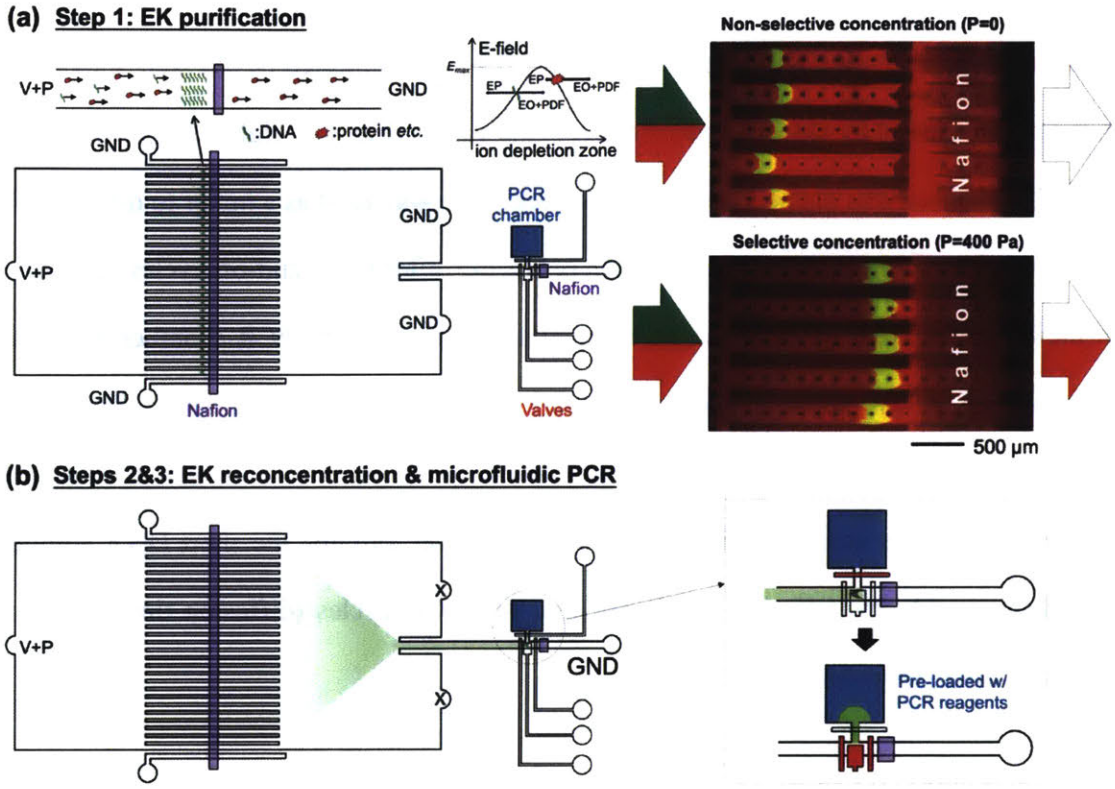


**Figure 6-2** Principle and operation procedures of HSEC-PCR. (a) EK purification of NAs in the first stage. (b) EK reconcentration of NAs in the second stage and transfer of NAs into the PCR chamber for amplification.

We next visualized the whole workflow of HSEC-PCR using MTB genomic DNA (target sequence concentration: 5 copies/μL), 10 mg/ml BSA, and 100 nM fluorescently labeled DNA spiked in human urine. As shown in Fig. 6-3 (left images), the DNAs were first selectively

concentrated in the 64 parallel microchannels in the first stage. A volume of ~150 μL was processed in 15 min. Next, the device was reconfigured as previously mentioned to transfer the concentrated DNAs into the second stage (Fig. 6-3, middle). The DNAs were almost fully reconcentrated in the second stage within 3 min. The reconcentrated DNAs were then isolated in the microchannel by closing a pair of pneumatic valves (Fig. 6-3, right). Next, the valve for the PCR chamber was opened, and the large-area valve was used as a mixer to drive the fluid and DNAs into the PCR chamber. As shown in Fig. 6-3, after 15 on-and-off cycles, the majority of the DNAs entered the PCR chamber. Finally, the valve for the PCR chamber was closed, followed by qPCR through thermal cycling. The fluorescence intensity (using green fluorescence setup) of the PCR chamber increased as qPCR proceeded. Note that, although the genomic DNA was not fully mixed in the PCR chamber initially, the short DNA amplicons mixed thoroughly by diffusion within the first few PCR cycles (diffusion time is ~15 min according to a previous study [116]).

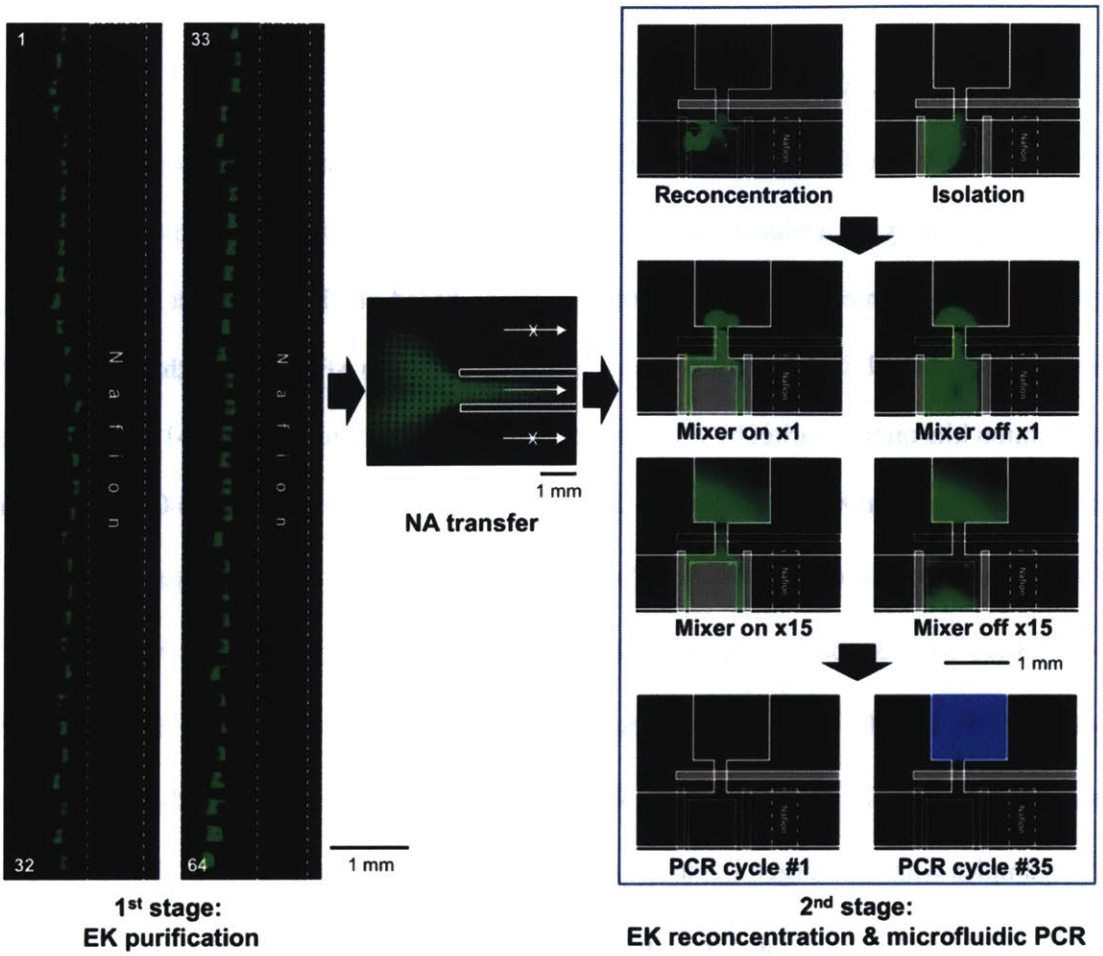


**Figure 6-3** The workflow of HSEC-PCR visualized by fluorescently labeled DNA. The left images showed the EK-concentrated DNAs in the parallel microchannels in the first stage during EK purification. The middle image is at the intersection of the first and second stages, which shows the transfer of the concentrated DNAs from the first stage to the second stage. In the right images, the reconcentrated DNAs were isolated and transferred into the PCR chamber by pneumatic valves. Finally, qPCR was performed in the PCR chamber, the fluorescence of which increased as qPCR proceeded.

6.1.3 Performance of HSEC-PCR

We compared the performance of HSEC-PCR with that of the standard bench-top SPE+PCR method by amplifying a highly specific sequence in the IS6110 region of the MTB genome (16 copies per genome) using a well-optimized probe-based qPCR (primer set A and probe A). First, we established the benchmark using standard bench-top SPE+PCR with the leading NA purification kits on the market by following the procedures outlined in Fig. 6-1(a). The Norgen Urine DNA Isolation Kit could process 2 mL urine per spin column, and the Qiagen QIAamp DNA Blood Mini Kit could process 0.2 mL serum per spin column. We spiked $3\times10^4$, $3\times10^3$, $3\times10^2$, $3\times10^1$, 3, 0.3, and 0 copies of the MTB genome (corresponding to $5\times10^5$, $5\times10^4$, $5\times10^3$, $5\times10^2$, $5\times10^1$, 5, and 0 copies of the target DNA) into 2 mL human urine, yielding target DNA concentrations of 400, 40, 4, 0.4, 0.04, 0.004, and 0 aM. We then purified the spiked human urine samples with the Norgen Urine DNA Isolation Kit, which took 100 min. We spiked $3\times10^4$, $3\times10^3$, $3\times10^2$, $3\times10^1$, 3, 0.3, and 0 copies of the MTB genome (corresponding to $5\times10^5$, $5\times10^4$, $5\times10^3$, $5\times10^2$, $5\times10^1$, 5, and 0 copies of the target DNA) into 0.2 mL human serum, yielding target DNA concentrations of 4000, 400, 40, 4, 0.4, 0.04, and 0 aM. We then purified the spiked human serum samples with the Qiagen QIAamp DNA Blood Mini Kit, which took 65 min. Fig. 6-4(a) and Fig. 6-4(b) show the amplification curves of the purified DNAs at different total spiked copy numbers in urine and serum using a bench-top thermal cycler, respectively. The target DNA was detectable when the total spiked copy number of the target DNA was as low as 50 copies, both for urine and serum. The main factor limiting the detection of lower copy

numbers is that, as a conventional practice, only a small fraction of the eluate (2 μL in this work) from the total 50 μL eluate (1/25) could be used for PCR, because of the high cost and slow thermal conduction of large-volume PCR [117]. The corresponding $C_q$ values of the qPCR were compared in Fig. 6-4(c). The $C_q$ values were very similar for the same total spiked DNA copy numbers in urine and serum, though the concentrations were different by one order of magnitude. This observation indicates that the recovery of the DNA purification kits is largely independent of the DNA concentration. The efficiencies of PCR for DNAs purified from urine and serum were both ~95% (calculated from the slopes of the fitted lines), indicating good removal of PCR inhibitors by the purification kits.

We next used HSEC-PCR for integrated purification, amplification, and detection of the target DNA. As previously mentioned, the device was able to process 150 μL samples in 15 min. We spiked $3\times10^2$, $3\times10^1$, 3, 0.3, and 0 copies of the MTB genome (corresponding to $5\times10^3$, $5\times10^2$, $5\times10^1$, 5, and 0 copies of the target DNA) into 150 μL human urine, yielding target DNA concentrations of 55, 5.5, 0.5, 0.05, and 0 aM. We spiked $3\times10^2$, $3\times10^1$, 3, 0.3, and 0 copies of the MTB genome (corresponding to $5\times10^3$, $5\times10^2$, $5\times10^1$, 5, and 0 copies of the target DNA) into 37.5 μL human serum, yielding target DNA concentrations of 220, 22, 2.2, 0.2, and 0 aM. The spiked serum samples were diluted to 150 μL with 1×PBS, which was necessary for stable EK concentration of the DNAs [115]. As shown in Fig. 6-4(d) and Fig. 6-4(e), HSEC-PCR could detect as low as 5 copies of the target DNA in both urine and serum, indicating the good recovery of the DNAs by HSEC. At very low copy numbers (50 and 5), the variances between the $C_q$ values of different runs were significantly greater than those of

higher copy numbers. This can be attributed to the potential incomplete collection of NAs into the PCR chamber during the reconcentration, isolation and mixing process, which generates more significant variances at very low copy numbers statistically. Although HSEC-PCR achieved the detection of lower copy numbers (5 v.s. 50) than standard SPE+PCR, the corresponding lowest detectable DNA concentrations were similar (0.05 v.s. 0.04 aM in urine and 0.2 v.s. 0.4 aM in serum), because the current HSEC-PCR device had lower throughputs than the SPE spin columns did (0.15 v.s. 2 mL for urine and 37.5 μL v.s. 200 μL for serum). We can increase the number of parallel microchannels in the first stage of the device to increase the throughput (up to 10 mL) and hence detect much lower concentrations, as we have demonstrated elsewhere [115]. Finally, as shown in Fig. 6-4(f), the efficiencies of HSEC-PCR were 87.1% and 79.1% for urine and serum, respectively, which were lower than those of standard bench-top SPE+PCR. This is commonly observed in microfluidic PCR systems, which can be attributed to a number of reasons, such as non-optimal thermal cycling conditions and the adsorption of polymerase on the PDMS surfaces of the PCR chamber [118], [119].

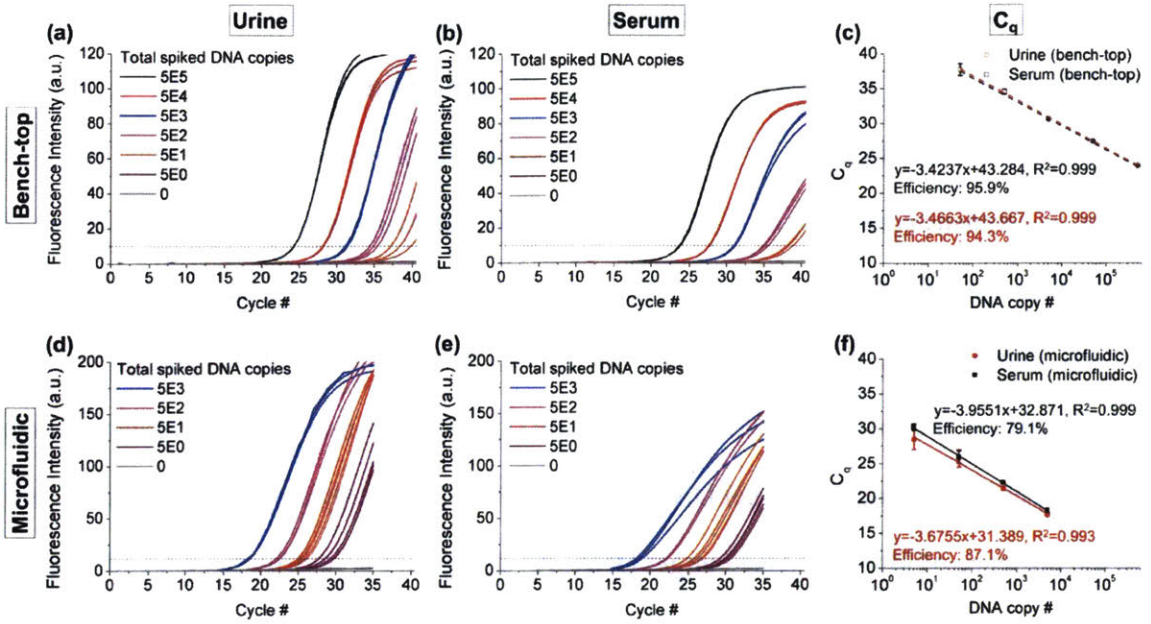


**Figure 6-4** Performance of standard bench-top SPE+PCR and HSEC-PCR for detecting DNA spiked in human urine and serum using probe-based qPCR (primer set A and probe A). Amplification curves of the target DNA purified from (a) urine and (b) serum, and (c) the corresponding $C_q$ values for different total spiked DNA copy numbers using standard bench-top SPE+PCR. Amplification curves of the target DNA purified from (d) urine and (e) serum, and (f) the corresponding $C_q$ values for different total spiked DNA copy numbers using HSEC-PCR.

### 6.1.4 Suppression of non-specific amplification by HSEC-PCR

We next tested the SYBR Green-based qPCR with primer set B (as listed in Table 1) [72] using the standard bench-top SPE+PCR and analyzed the PCR products using gel electrophoresis. SYBR Green is a commonly used intercalating dye for the real-time quantification of PCR by

binding non-specifically to double-stranded DNA, which avoids the use of expensive qPCR probes. As shown in Fig. 6-5(a), only a band of the 130-bp amplicon was observed from the PCR product of the target DNA ($10^5$ spiked copies) purified from 2 mL human urine. However, in the no-template control with only DI water, multiple bands of non-amplicons were observed, indicating non-specific amplification due to primer dimers. The gel electrophoresis result clearly indicates that PCR is a competition for reagents between specific and non-specific amplifications: the specific amplification strongly suppressed non-specific amplification in the presence of high-abundance target DNA, while the non-specifically amplified products prevail in the presence of low-abundance target DNA. As shown in Fig. 6-5(b), in standard bench-to SPE+PCR, 500 or fewer copies of the target DNA could not be distinguished from 0 copy of the target DNA due to strong non-specific amplification, indicating a detection limit of 5000 copies. A PCR efficiency of 107.88% (Fig. 6-5(c)) in bench-top PCR indicates that DNAs were generated faster than a standard 2-fold replication per cycle (100%), which was caused by the additional fluorescence signal from non-specific amplification (especially at low target DNA concentrations). In HSEC-PCR, the target DNA molecules were concentrated into a microfluidic chamber (~0.1 μL), in which there were much fewer primer dimers than a conventional tube (~20 μL). With the all the DNAs collected into the microfluidic chamber but with much fewer primer dimers, the signal-to-noise ratio is greatly enhanced, thereby enabling the detection of lower copy numbers of the target DNA. Also, increasing the concentration of the target DNA will exhaust the reagents at earlier cycles, thereby suppressing the amplification of primer dimers that typically occur at large cycle numbers. As shown in Fig. 6-5(d), although non-specific amplification was still observed in HSEC-PCR using primer

set B, as low as 5 copies of the target DNA was distinguishable from 0 copy of the target DNA, indicating the effective suppression of non-specific amplification. HSEC-PCR was able to detect 5 copies of the target DNA even using a non-optimal PCR design, which is three orders of magnitude better than that achieved by the standard bench-top PCR. A PCR efficiency of 74.6% was achieved by HSEC-PCR (Fig. 6-5(e)), which was attributed to similar factors discussed previously. This result suggests that HSEC-PCR can significantly shorten the development cycle of NAATs by skipping the lengthy optimization process for primer dimer elimination and still achieving good detection sensitivity with non-optimal PCR designs.

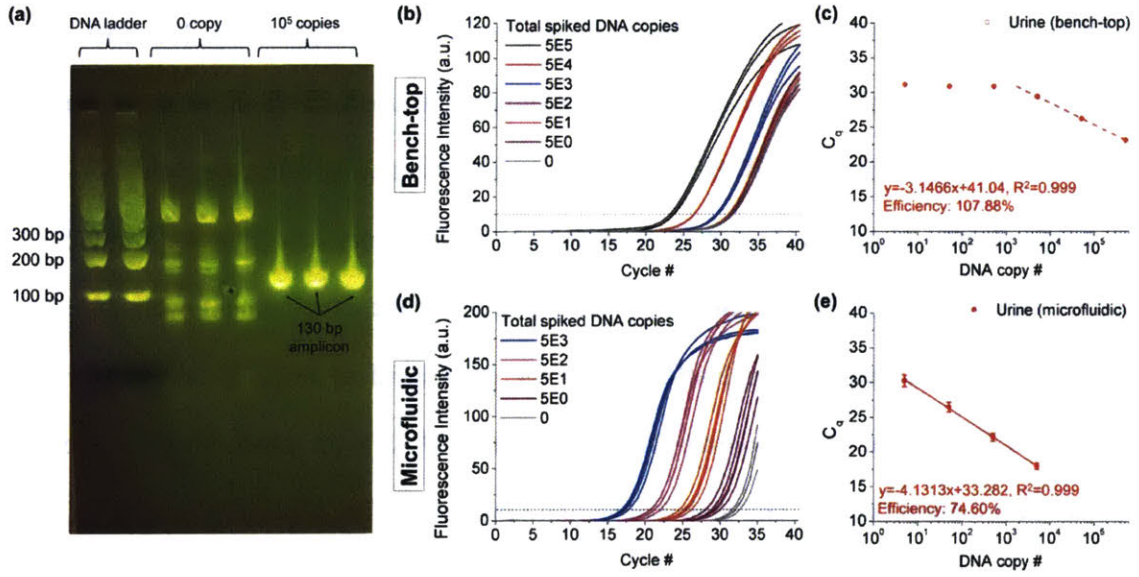


**Figure 6-5** Performance of standard bench-top SPE+PCR and HSEC-PCR for detecting DNA spiked in human urine using a non-optimal PCR design (primer set B). (a) Gel electrophoresis result of PCR products using standard bench-top SPE+PCR. (b) Amplification curves for different total spiked DNA copy numbers using standard bench-top SPE+PCR. (c) $C_q$ values for different total spiked DNA copy numbers using standard bench-top SPE+PCR. (d)

Amplification curves for different total spiked DNA copy numbers using HSEC-PCR. (e) $C_q$ values for different total spiked DNA copy numbers using HSEC-PCR.

### 6.1.5 Summary

In this paper, we have demonstrated HSEC-PCR as an integrated platform with one-step NA purification and noise-resistant quantitative PCR for rapid and reliable detection of ultralow-abundance NAs in real biofluids. Compared to conventional SPE-based NA purification methods (bench-top or microfluidic format), EK purification is a one-step, liquid-phase, non-binding approach with the advantages of short processing time (20 min), low cost, simple device design and operation protocols, and avoiding the use of PCR-inhibitive chemicals. Unlike standard bench-top PCR, HSEC-PCR is resistant to non-specific amplification caused by primer dimers in non-optimal PCR designs and retains a very low detection limit (5 DNA copies, equaling 0.3 MTB cell), thereby greatly shortening the development cycle of NAATs. Although we demonstrated our platform with the gold-standard PCR, it can be universally applied to isothermal amplification-based and other NAATs for much simpler operation, shorter development cycles, and higher detection sensitivity. The future directions of this work include: (1) Further integration of the system by using portable or smart-phone-based fluorescence microscopes for qPCR imaging and portable valve controllers, (2) further shortening the amplification time by ultra-fast thermal cycling using infrared/laser or high-power Peltier elements, (3) increasing the sample processing throughput of the device to detect

lower concentrations of DNAs by scaling up the number of parallel microchannels, and (4) evaluating the performance of HSEC-PCR for different sample types (*e.g.* saliva, blood).

### 6.1.6 Experimental section

#### *6.1.6.1 Materials and reagents*

Phosphate-buffered saline (PBS) and PCR-grade water were purchased from Thermo Fisher Scientific (Waltham, MA). Bovine serum albumin (BSA), Tween 20, mineral oil, and Nafion resin (20 wt % solution in lower aliphatic alcohol/$H_2O$ mix) were purchased from Sigma-Aldrich (St. Louis, MO). Ag/AgCl electrodes (diameter: 0.008 in.) were purchased from A-M Systems (Sequim, WA). Tygon non-DEHP microbore tubing (inner diameter: 0.020 in., outer diameter: 0.060 in.) was purchased from Cole-Parmer (Vernon Hills, IL). A 96-base ssDNA (5'-AG CGA GCT AGC GAG CTA GCG AGC TAG CGA GCT AGC GAG CTA GCG AGC TAG CGA GCT AGC GAG CTA GCG AGC TAG CGA GCT AGC GAG CTA GCG AGC T-3') with 5'-labeled Alexa Fluor 647 (Integrated DNA Technologies, Coralville, IA) was used for the visualization of the electrokinetic concentration phenomenon. Mycobacterium tuberculosis (strain H37Rv) genomic DNA was purchased from ATCC (Manassas, VA). Human urine was purchased from Lee Biosolutions (Maryland Heights, MO). Human serum was purchased from Millipore Sigma (Burlington, MA). In standard SPE, MTB genomic DNA spiked in human urine was purified using the Urine DNA Isolation Kit from Norgen Biotek (Thorold, ON, Canada); MTB genomic DNA spiked in human serum was purified using the QIAamp DNA Blood Mini Kit from Qiagen (Hilden, Germany).

*6.1.6.2 Microfluidic device fabrication*

Microfluidic devices were fabricated using multi-layer soft lithography. The silicon mold for the control layer was fabricated using the SU-8 2025 photoresist (MicroChem, Westborough, MA), on which the valve features were defined (30 μm deep). The silicon mold for the flow layer was fabricated with two photolithography steps, on which the microfluidic structures were defined. First, the major microfluidic channels (except for the PCR chamber) were fabricated using the AZ4620 photoresist (MicroChemicals GmbH, Ulm, Germany). The AZ4620 patterns were baked at 200°C for 1 hour to round the microfluidic channels that facilitated the complete closing of the pneumatic valves and to prevent the erosion of the AZ4620 photoresist during the addition of the subsequent layer. The microfluidic channels were 13 μm deep after hard bake. Second, the PCR chamber was patterned onto the silicon mold using the SU-8 2050 photoresist (MicroChem, Westborough, MA), which was 80 μm deep.

The microfluidic devices were cast from the silicon molds using Polydimethylsiloxane (PDMS) (Dow Chemical Company, Midland, MI). The PDMS base and curing agent were mixed at a weight ratio of 10:1. First, the uncured PDMS mixture was spin-coated on the flow-layer silicon mold at 1200 rpm for 30 s, which was then baked at 120°C for 2 min. Second, the uncured PDMS mixture was poured on the control-layer silicon mold, which was then baked at 95°C for 60 min. After baking, the PDMS of the control layer was peeled off from the silicon mold and cut into units. Third, the control-layer PDMS units were bonded onto the flow layer using oxygen plasma bonding (Femto Science Covance Plasma Cleaner, Gyeonggi-Do, Korea)

and baked at 60°C for 60 min. Finally, the two-layer bonded monolithic PDMS units were peeled off from the flow-layer silicon mold. Access holes were punched on the PDMS units.

Two Nafion strips were patterned on a glass slide using the Nafion resin by the microflow-patterning technique with microchannels of 400 μm wide and 50 μm deep [23]. Each PDMS unit was bonded with a Nafion-patterned glass slide using oxygen plasma bonding.

*6.1.6.3 qPCR design*

6.1.6.3.1 Probe-based qPCR

The probe-based qPCR targets a highly specific sequence in the IS6110 region of the MTB genome. There are 16 copies of the target DNA per genome of the MTB strain H37Rv [120]. The probe-based qPCR assay (primer set A and probe A) is listed in Table 6-1 [121]. The probe-based qPCR assay was synthesized and pre-mixed by Integrated DNA Technologies (Coralville, IA) and then reconstituted with PCR-grade water, in which the concentrations of the forward primer, reverse primer, and probe were 5 μM, 5 μM, and 2.5 μM, respectively. PrimeTime Gene Expression Master Mix from Integrated DNA Technologies (Coralville, IA) was used as the master mix for probe-based qPCR. Depending on the number of reactions, different volumes of reagent mix were prepared using the following recipe: every 450 μL reagent mix contained 250 μL master mix, 25 μL probe-based qPCR assay, 50 μL 1% Tween 20, 125 μL PCR-grade water. In bench-top PCR, each reaction (20 μL) used 18 μL reaction mix and 2 μL purified DNA template. The thermal cycling program was 95°C for 3 min (initial activation) followed by 40 cycles of 95°C for 15 s (denaturation) and 60°C for 60 s (annealing and extension) using LightCycler 480 Real-Time PCR System (Roche Life Science).

6.1.6.3.2 SYBR Green-based qPCR

SYBR Green is a commonly used intercalating dye for the real-time quantification of PCR by binding non-specifically to double-stranded DNA. The SYBR Green-based qPCR (primer set B) also targets a highly specific sequence in the IS6110 region of MTB genome, which is listed in Table 6-1 [72]. Each primer was reconstituted with PCR-grade water to a concentration of 5 μM. SYBR Green PCR Master Mix (2x) from Thermo Fisher Scientific (Waltham, MA) was used as the master mix for SYBR Green-based qPCR. Depending on the number of reactions, different volumes of reagent mix were prepared using the following recipe: every 450 μL reagent mix contained 250 μL master mix, 25 μL forward primer, 25 μL reverse primer, 50 μL 1% Tween 20, 100 μL PCR-grade water. In bench-top PCR, each reaction (20 μL) used 18 μL reaction mix and 2 μL purified DNA template. The thermal cycling program was 95°C for 10 min (initial activation) followed by 40 cycles of 95°C for 15 s (denaturation) and 60°C for 60 s (annealing and extension) using LightCycler 480 Real-Time PCR System (Roche Life Science). The gel electrophoresis analysis of PCR products was performed using the blueGel™ Electrophoresis System (Amplyus, Cambridge, MA).

***Table 6-1*** *Sequences of qPCR primers and probe.* In Probe A, 6-FAM is the fluorescence dye at 5' and ZEN™ and IABkFQ™ (Iowa Black FQ) are the double fluorescence quenchers (Integrated DNA Technologies, IA).

| Name | Sequence (5'→3') |
|---|---|
| Forward primer A | CGA TGT GTA CTG AGA TCC CCT ATC CG |

| | |
|---|---|
| Reverse primer A | GGC CTT TGT CAC CGA CGC C |
| Probe A | /56-FAM/ AAC GTC TTT /ZEN/ CAG GTC GAG TAC GCC TT /3IABkFQ/ |
| Forward primer B | ACC AGC ACC TAA CCG GCT GTG G |
| Reverse primer B | CAT CGT GGA AGC GAC CCG CCA G |

*6.1.6.4 Device operation and system setup*

A 200 μL pipette tip was inserted into the inlet as the reservoir. Tygon tubings were inserted into the outlets. Ag/AgCl electrodes were inserted into the inlet and outlets and connected to a DC power supply (Stanford Research Systems, Sunnyvale, CA). The pneumatic valves were filled with mineral oil to prevent gas permeation into the microfluidic channels. The pneumatic valves were opened and closed using a home-made gas controller. The qPCR reaction mix was injected into the device until it completely filled the PCR chamber. Then the valve for the PCR chamber was closed. Next, the microfluidic channel walls were passivated with 1% BSA in 1×PBS for 10 min to prevent the non-specific binding of biomolecules and flushed with 1×PBS afterward. The microfluidic device was placed on a miniaturized thermal cycler MiniPCR™ (Amplyus, Cambridge, MA) for thermal cycling during PCR. The thermal cycling program of the microfluidic PCR was 95°C for 3 min (probe-based qPCR) or 10 min (SYBR Green-based qPCR) followed by 35 cycles of 95°C for 10 s (denaturation) and 60°C for 30 s (annealing and extension). Fluorescence imaging of the microfluidic operation and qPCR was performed with a fluorescence microscope (IX71, Olympus, Tokyo, Japan) and a CCD camera (Sensicam qe,

Cooke Corporation, Romulus, MI). Fluorescence images were analyzed using the ImageJ software. The average fluorescence intensity of the PCR chamber was used to plot the qPCR curve.

### 6.2 Interfacing with NanoString nCounter®

NanoString nCounter® is a non-amplification platform for the direct counting of up to 800 nucleic acids per run using target-specific, color-coded probe pairs [122], [123]. Because it is a non-amplification method, enrichment of target biomolecules is critical for enhancing the detection sensitivity of NanoString nCounter®. We demonstrate the application of the electrokinetic concentrator for enhancing the sensitivity of NanoString nCounter® in the context of detecting the bacterial 16s ribosomal RNA (16s rRNA), which is highly abundant and species-specific for bacteria identification [124].

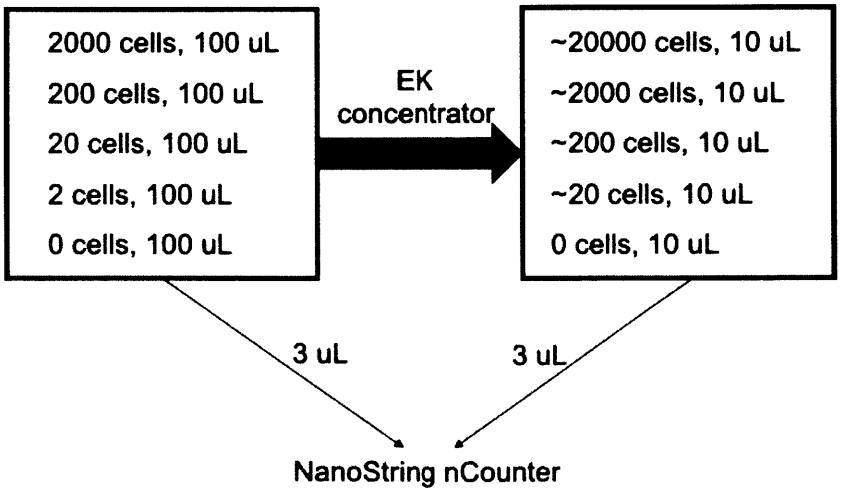

**Figure 6-6** Experimental flow of using the electrokinetic concentrator for enhancing the detection sensitivity of Staph. aureus by NanoString nCounter.

As shown in Fig. 6-5, we spiked different numbers of Staph. Aureus cells (2000, 200, 20, 2, 0) in 100 μL of 0.1×PBS and lyse the bacterial cells with bead beating. The sample preparation step was performed by Peijun Ma and Lorrie He of Prof. Deborah Hung's group at the Broad Institute. Next, the lysates were processed by the first stage of the 320-plex concentrator, during which the nucleic acids were enriched and proteins were removed. After enrichment, the enriched nucleic acids were flushed to the outlets to a total volume of 10 μL. Finally, 3 μL of the unconcentrated (original) lysates and 3 μL of the concentrated lysates for each number of bacteria were loaded into NanoString nCounter® for the measurement of the Staph. aureus-specific 16s rRNA, respectively.

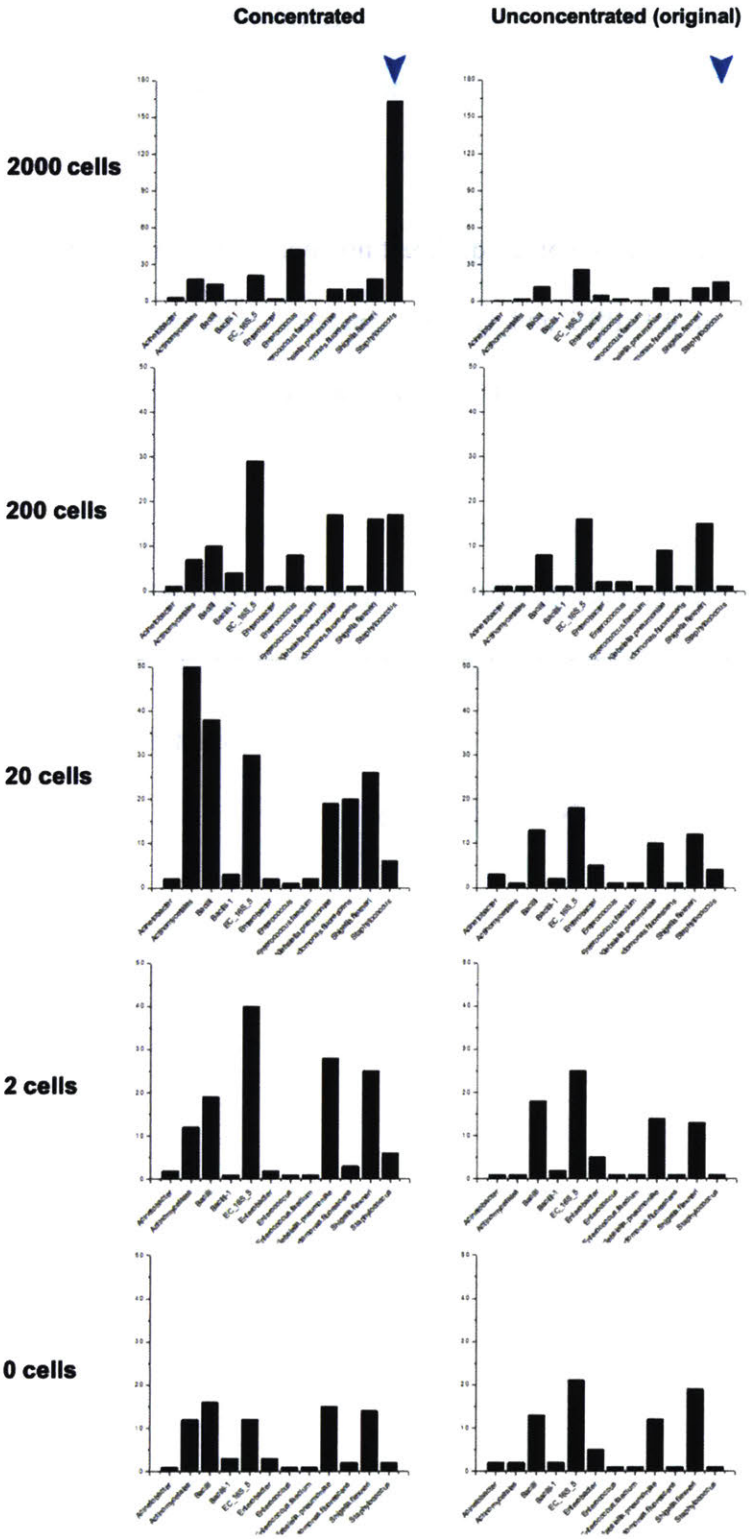
Concentrated
Unconcentrated (original)
2000 cells
200 cells
20 cells
2 cells
0 cells

**Figure 6-7** Results of Staph. aureus detection by NanoString nCounter with and without concentration. The y-axis is the counts of the target rRNA. The x-axis is the species-specific probes, among which the right most probe is specific to Staph. aureus.

As shown in Fig. 6-6, with concentration, NanoString nCounter® was able to detect as low as 2 cells, compared to the detection limit of ~20 cells without concentration. In this experiment, the lysates were concentrated from 100 μL to 10 μL, corresponding to a maximum enrichment factor of 10 according to mass conservation. The detection limit can be lowered to sub-single cell by collecting larger volumes (>100 μL) of samples (such as plasma, urine, milk infected with bacteria) and concentrating them into volumes of 10 μL or smaller in real applications.

# Chapter 7 Conclusions and outlooks

In this dissertation, we have developed the hierarchical selective electrokinetic concentration technique as a universal next-generation biomolecule enrichment technique for molecular diagnostics and many more fields of biology and medicine. We established an analytical model that precisely describes the biomolecule concentration behaviors in this nonlinear, multi-physics system, which enables rational design and optimization of relevant devices. By coupling the mobility-based selective concentration mode and molecular modification of affinity binders, we realized the specific enrichment of only the target biomolecules, which resembles the specific amplification of PCR. By massive parallelization and hierarchical cascading of unit electrokinetic concentrators, we realized the billion-fold enrichment of target biomolecules within 30 min, which universally applies to DNA, protein, and other biomolecules. With specific enrichment and billion-fold enrichment, we demonstrated amplification-free detection of disease-relevant nucleic acids and proteins to the aM level within an hour, which is unparalleled by existing techniques in many aspects. We finally demonstrated that hierarchical selective electrokinetic concentration could function as a one-step nucleic acid purification technique and significantly suppress non-specific amplification caused by non-optimal PCR design, thereby greatly shortening the development cycle and simplifying the workflow of nucleic acid amplification tests. Our next-generation biomolecule enrichment technique may unleash fundamental studies in omics and molecular biology as well as practical applications in molecular diagnostics, environment monitoring, and food analytics. The most valuable future research directions of this technique include the follows: (1) Novel

device design to make the device simpler and more robust to fabricate and operate; (2) systematic implementation and evaluation in clinical tests with large patient populations to establish the sensitivity, specificity, and other metrics of this platform for various diseases; (3) integration of this platform with next-generation sequencing, mass spectrometry, and other standard analytics to enhance their analytical performance.

# Appendix 1. Details of the analytical model and numerical simulation of electrokinetic concentration

## A1.1. Derivation of the EK limit

Because the electrophoretic force is co-directional with the fluid drag force for the cation and counter-directional for the anion and analyte particle, the fluxes of charged species satisfy $J_1^\infty \gg J_2^\infty$, $J_1^\infty \gg J_3^\infty$, as supported by the simulation data in Fig. A1-1-1.

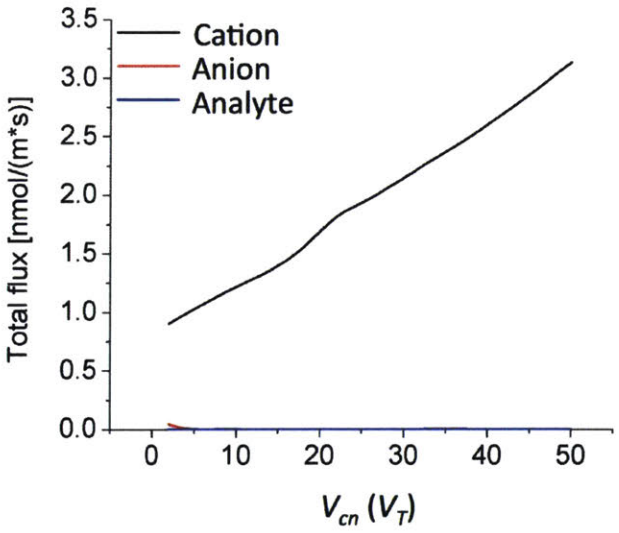


**Fig. A1-1-1.** The fluxes of the cation, anion and analyte particle at the steady state at different $V_{cn}$'s.

In this derivation, we will only consider symmetric binary electrolytes (e.g. KCl) as the buffer, i.e. $D_1 = D_2$, $Z_1 = -Z_2$, $C_1^0 = C_2^0$. The electroneutrality is generally obeyed except in the space charges layers in the ion depletion zone, so we can approximate that $C_1^\infty \approx C_2^\infty$ for $x<L/2$.

By approximating $J_2^\infty \approx 0$ and $J_3^\infty \approx 0$, the fluxes of the cation, anion, and analyte can be written as,

$$J_1^\infty = -D_1 \frac{dC_1^\infty}{dx} + (\bar{u} + \mu_1 E) C_1^\infty = J_C , \qquad \text{A1.1.1}$$

$$J_2^\infty = -D_2 \frac{dC_2^\infty}{dx} + (\bar{u} - \mu_2 E) C_2^\infty \approx 0 , \qquad \text{A1.1.2}$$

$$J_3^\infty = -D_3 \frac{dC_3^\infty}{dx} + (\bar{u} - \mu_3 E) C_3^\infty \approx 0 , \qquad \text{A1.1.3}$$

where $J_C$ is constant with respect to $x$ ($x$<$L$/2) at the steady state, and $\bar{u}$ is independent of $x$ due to the incompressibility of fluid.

Subtracting Eq. A1.1.2 from Eq. A1.1.1 yields that,

$$\mu_2 E C_2^\infty \approx J_C / 2 . \qquad \text{A1.1.4}$$

Substituting Eq. A1.1.4 to Eq. A1.1.2 yields that,

$$-D_2 \frac{dC_2^\infty}{dx} + \bar{u} C_2^\infty - \frac{J_C}{2} \approx 0 . \qquad \text{A1.1.5}$$

At the inlet ($x = 0$), $\frac{dC_2^\infty}{dx}|_{x=0} \approx 0$ and $C_2^\infty (x = 0) = C_2^0$, which leads to,

$$J_C \approx 2\bar{u} C_2^0 . \qquad \text{A1.1.6}$$

Substituting Eq. A1.1.6 to Eq. A1.1.5 yields that,

$$-D_2 \frac{dC_2^\infty}{dx} + (C_2^\infty - C_2^0)\bar{u} \approx 0 . \qquad \text{A1.1.7}$$

Therefore, $C_2^\infty (x) \approx C_2^0 + A e^{\frac{\bar{u}}{D_2} x}$, where $A$ is a constant.

We define the downstream anion concentration (after depletion) as $C_2^d$. At the nanochannel arrays ( $x = L/2$ ), we have $C_2^\infty(x=\frac{L}{2}) = C_2^d$, which leads to,

$$C_2^\infty(x) \approx \left(1 - \Psi e^{\mathrm{Pe}\frac{x}{L/2}}\right) \cdot C_2^0, \quad (x < L/2) \qquad \text{A1.1.8}$$

where $\Psi = (1 - \frac{C_2^d}{C_2^0}) e^{-\mathrm{Pe}}$ and $\mathrm{Pe} = \frac{\bar{u}(L/2)}{D_2}$, with Pe being the Péclet number of the system.

Substituting Eq. A1.1.6 and Eq. A1.1.8 to Eq. A1.1.4 yields that,

$$E(x) \approx \frac{\bar{u}}{\mu_2} \cdot \frac{1}{1 - \Psi e^{\mathrm{Pe}\frac{x}{L/2}}}. \qquad \text{A1.1.9}$$

Up to this point, the distributions of buffer ions and the electric field have been solved.

Next, by substituting Eq. A1.1.9 to Eq. A1.1.3 and applying the boundary condition $C_3^\infty(x=0) = C_3^0$, one can obtain the distribution of the analyte concentration along the x-axis as,

$$C_3^\infty(x) \approx \left(\frac{1 - \Psi e^{\mathrm{Pe}\frac{x}{L/2}}}{1 - \Psi}\right) \cdot e^{(1-\frac{b}{a})\mathrm{Pe}\frac{x}{L/2}} \cdot C_3^0. \qquad \text{A1.1.10}$$

At the concentration peak ( $C_{EK}^\wedge$ ), $\frac{dC_3^\infty(x)}{dx} = 0$, from which one can obtain that,

$$C_{EK}^\wedge \approx \left[\frac{1}{\Psi}(1 - \frac{\mu_3}{\mu_2})\right]^{\frac{D_2}{D_3}(1-\frac{\mu_3}{\mu_2})} \left(\frac{1}{1-\Psi}\frac{\mu_3}{\mu_2}\right)^{\frac{D_2}{D_3}\frac{\mu_3}{\mu_2}} C_3^0. \qquad \text{A1.1.11}$$

Under conditions of $C_2^0 \gg C_2^d$ (due to the ion depletion effect) and $e^{\mathrm{Pe}} \gg 1$ ( $e^{\mathrm{Pe}}$= 609 and 35614 for $V_{cn}$=2$V_T$ and $V_{cn}$=15$V_T$, respectively.), Eq. A.1.11 can be simplified to,

$$C_{EK}^{\wedge} \approx \left(1-\frac{\mu_3}{\mu_2}\right)^{\frac{D_2}{D_3}\left(1-\frac{\mu_3}{\mu_2}\right)} \cdot \left(\frac{\mu_3}{\mu_2}\right)^{\frac{D_2\mu_3}{D_3\mu_2}} \cdot \left(e^{\mathrm{Pe}}\right)^{\frac{D_2}{D_3}\left(1-\frac{\mu_3}{\mu_2}\right)} \cdot C_3^{(}. \qquad \text{A1.1.12}$$

Defining $a=\frac{D_2}{D_3}$, $b=\frac{Z_3}{Z_2}$, $\frac{b}{a}=\frac{\mu_3}{\mu_2}$, Eq. A1.1.12 can be re-written as,

$$C_{EK}^{\infty} \approx a^{-a} b^{b} (a-b)^{(a-b)} \cdot e^{(a-b)\cdot \mathrm{Pe}} \cdot C_3^0. \qquad \text{A1.1.13}$$

## A1.2. Derivation of the EN limit

At the steady state, the fluxes of all charged species are constant along the $x$-axis ($x<L/2$). Considering the inlet and the concentration plateau, one can have $J_1^{\infty}(\text{in}) = J_1^{\infty}(\text{p})$, $J_2^{\infty}(\text{in}) = J_2^{\infty}(\text{p}) \approx 0$, $J_3^{\infty}(\text{in}) = J_3^{\infty}(\text{p}) \approx 0$, where "in" denotes the inlet, and "p" denotes the concentration plateau. These equations can be expanded to,

$$-D_1\frac{dC_1^{\infty}(\text{in})}{dx} + (\bar{u} + \mu_1 E_{\text{in}})C_1^{\infty}(\text{in}) = -D_1\frac{dC_1^{\infty}(\text{p})}{dx} + (\bar{u} + \mu_1 E_{\text{p}})C_1^{\infty}(\text{p}), \quad \text{A1.2.1}$$

$$-D_2\frac{dC_2^{\infty}(\text{in})}{dx} + (\bar{u} - \mu_2 E_{\text{in}})C_2^{\infty}(\text{in}) = -D_2\frac{dC_2^{\infty}(\text{p})}{dx} + (\bar{u} - \mu_2 E_{\text{p}})C_2^{\infty}(\text{p}) \approx 0, \quad \text{A1.2.2}$$

$$-D_3\frac{dC_3^{\infty}(\text{in})}{dx} + (\bar{u} - \mu_3 E_{\text{in}})C_3^{\infty}(\text{in}) = -D_3\frac{dC_3^{\infty}(\text{p})}{dx} + (\bar{u} - \mu_3 E_{\text{p}})C_3^{\infty}(\text{p}) \approx 0. \quad \text{A1.2.3}$$

At the inlet, the concentrations of all charged species equal the initial concentration, and the concentration gradients can be considered zero. At the concentration plateau, the concentration gradients of all charged species are zero. Therefore, $C_i^{\infty}(\text{in}) = C_i^0$, $\frac{dC_i^{\infty}(\text{in})}{dx} = 0$, $\frac{dC_i^{\infty}(\text{p})}{dx} = 0$, $i$=1, 2, 3. Eqs. A1.2.1-A1.2.3 can be reduced to,

$$(\bar{u} + \mu_1 E_{\text{in}})C_1^0 = (\bar{u} + \mu_1 E_{\text{p}})C_1^{\infty}(\text{p}), \quad \text{A1.2.4}$$

$$(\bar{u} - \mu_2 E_{\text{in}})C_2^0 = (\bar{u} - \mu_2 E_{\text{p}})C_2^{\infty}(\text{p}) \approx 0, \quad \text{A1.2.5}$$

$$(\bar{u} - \mu_3 E_{\text{in}})C_3^0 = (\bar{u} - \mu_3 E_{\text{p}})C_3^{\infty}(\text{p}) \approx 0. \quad \text{A1.2.6}$$

In Eq. A1.2.5, the total flux is zero, and $C_2^0$ is much greater than zero, one can have,

$$\bar{u} \approx \mu_2 E_{\text{in}}. \quad \text{A1.2.7}$$

In Eq. A1.2.6, the total flux is zero, and $C_3^{\infty}(\text{p})$ is much greater than zero, one can have,

$$\bar{u} \approx \mu_3 E_p \,. \qquad \text{A1.2.8}$$

From Eq. A1.2.7 and Eq. A1.2.8, one can have,

$$E_p \approx \frac{\mu_2}{\mu_3} E_{in} \,. \qquad \text{A1.2.9}$$

Substituting Eq. A1.2.7 and Eq. A1.2.9 to Eq. A1.2.4 yields that,

$$C_1^{\infty}(\mathrm{p}) \approx \frac{\mu_1/\mu_2 + 1}{\mu_1/\mu_3 + 1} C_1^0 \,. \qquad \text{A1.2.10}$$

At the concentration plateau, $C_2^{\infty}(\mathrm{p}) \approx 0$, so the electroneutrality condition requires that,

$$Z_1 C_1^{\infty}(\mathrm{p}) + Z_3 C_3^{\infty}(\mathrm{p}) \approx 0 \,. \qquad \text{A1.2.11}$$

Combining Eq. A1.2.10 and Eq. A1.2.11 gives that,

$$C_{EN}^{\infty} = C_3^{\infty}(\mathrm{p}) \approx -\frac{Z_1}{Z_3} \cdot \frac{\mu_1/\mu_2 + 1}{\mu_1/\mu_3 + 1} \cdot C_1^0 \,. \qquad \text{A1.2.12}$$

Note that this equation is generally applicable to arbitrary binary electrolytes. For symmetric electrolytes, Eq. A1.2.12 can be reduced to,

$$C_{EN}^{\infty} \approx \frac{2}{a+b} \cdot C_1^0 \,. \qquad \text{A1.2.13}$$

## A1.3. The relation between $\bar{u}$ and $V_{cn}$

The velocity profile of the system is shown in Fig. A1-3-1. The action of a tangential electric field upon the induced space charges near the nanochannel arrays induces a non-equilibrium electroosmotic flow, which is named the electroosmosis of the second kind (EOF2) by Dukhin *et al* [125]. This electroosmotic slip is much faster (>10x) than the primary electroosmosis (EOF1) in the bulk channel. Consequently, a pair of vortices is generated near the nanochannel arrays to satisfy the incompressibility of fluid. At the same time, a pressure-driven flow is induced in the bulk channel that speeds up the net fluid velocity ($\bar{u}$), as indicated by the parabolic flow profiles at higher $V_{cn}$'s.

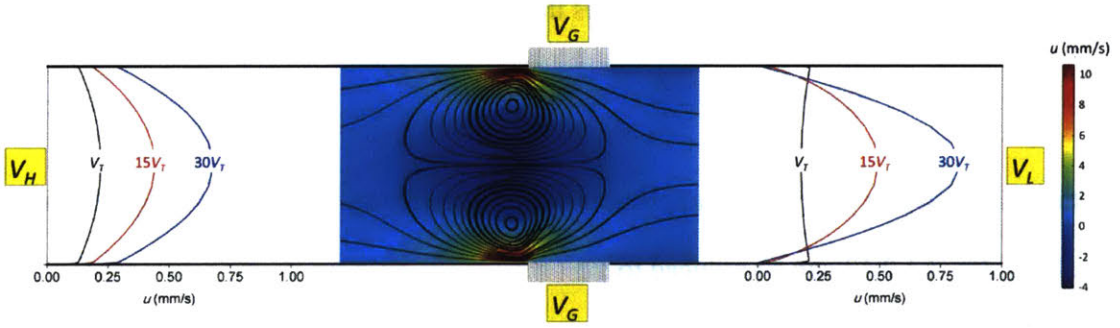


**Fig. A1-3-1** Fluid velocity profiles in the central microchannel. The electrical configuration is $V_{HL}=20V_T$, with $V_{cn}$ labeled on each curve. The color map represents the x-direction velocity ($u$) at $V_{cn}=20V_T$.

Theoretical modeling of the fluid flow of the system is challenging, as it involves the coupling of EOF1 and EOF2. Rubinstein *et al.* [47], [53], [126], [127] and Kim *et al.* [46] studied the symmetric case of the system ($V_H=V_L$) , in which there is no net tangential fluid

flow ($\bar{u}=0$). According to their studies, the EOF2 slip velocity ($u_{s2}$) near the nanochannel surfaces is proportional to the square or cube of $V_{cn}$, depending on the magnitude of the electric field applied. This nonlinear dependence is observed in our model by setting $V_H$=$V_L$, as shown in Fig. A1-3-2.

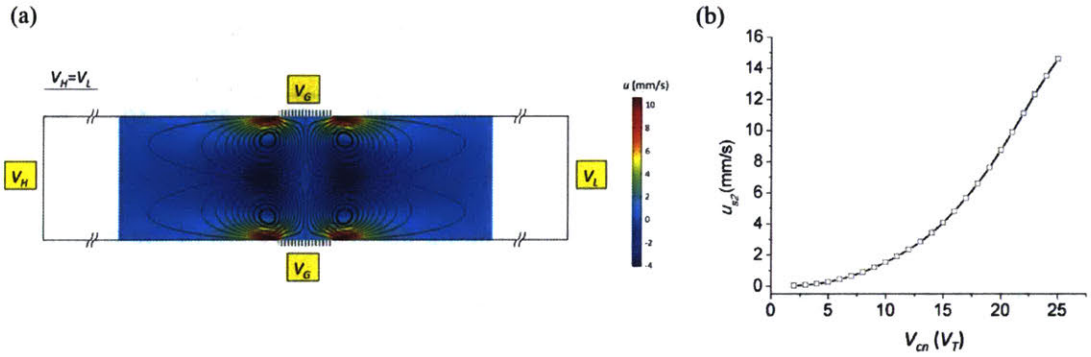


**Fig. A1-3-2.** (a) Velocity streamlines and velocity magnitude in a symmetric system. The color map represent the x-direction velocity ($u$) at $V_{cn}$=21$V_T$. (b) The EOF2 slip velocity ($u_{s2}$) in the vicinity of the nanochannel arrays (x=59 μm).

However, when the symmetry is broken ($V_{HL}=V_H-V_L>0$), EOF2 contributes to the net tangential fluid flow. Fig. A1-3-3(a) shows the velocity profiles along the cross-section of the channel in the vicinity of the nanochannel arrays (x=59 μm) at different $V_{cn}$'s. We take the maximum velocity as the EOF2 slip velocity ($u_{s2}$). As shown in Fig. A1-3-3(b), $u_{s2}$ is proportional to $V_{cn}$, which is clear departure from the scaling relation in the symmetric scenario. The detailed mechanism calls for further theoretical studies.

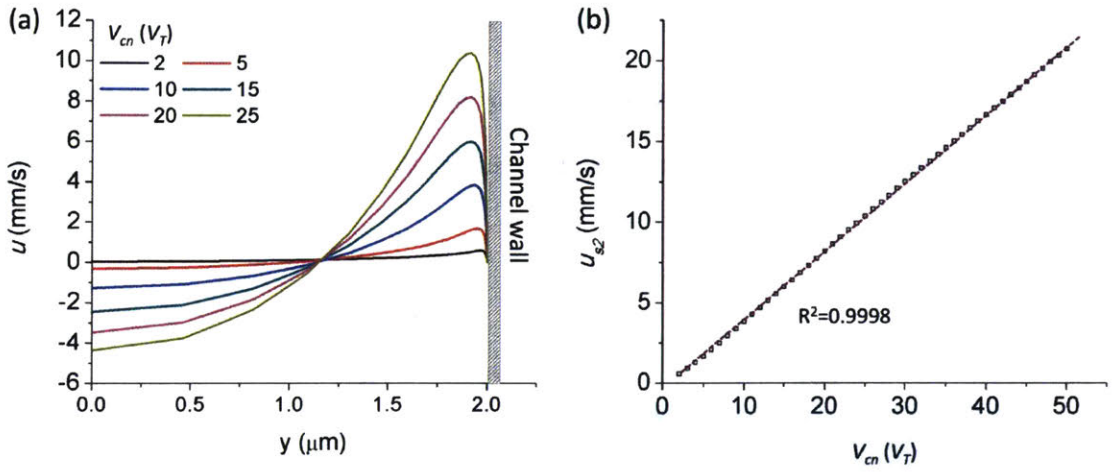


**Fig. A1-3-3.** (a) The x-direction velocity ($u$) profiles along the cross-section of the channel in the vicinity of the nanochannel arrays (x=59 μm) at different $V_{cn}$'s at $V_{HL}$=15$V_T$. (b) Dependence of the EOF2 slip velocity ($u_{s2}$) on $V_{cn}$ at $V_{HL}$=15$V_T$.

Fig. A1-3-4 shows the dependence of $\bar{u}$ on $V_{cn}$ and $V_{HL}$. When $V_{cn}$ is relatively low compared to $V_{HL}$, the system is dominated by the tangential electric field set up by $V_{HL}$. In this regime, $\bar{u}$ is mainly determined by EOF1, because EOF2 is relatively low due to the weak ion depletion effect. Consequently, $\bar{u}$ increases approximately linearly with $V_{cn}$ at a small slope, as lowering $V_n$ also increases the upstream tangential electric field that drives EOF1. As $V_{cn}$ further increases, the system becomes dominated by the electric field set up by $V_H$ and $V_n$. In this regime, $\bar{u}$ is mainly determined by EOF2. Because EOF2 is linear with $V_{cn}$ as aforementioned and EOF2 is much faster than EOF1, $\bar{u}$ increases linearly with $V_{cn}$ with a large slope. Lastly, the higher $V_{HL}$ is, the higher $V_{cn}$ is needed to enter the EOF2-dominated regime.

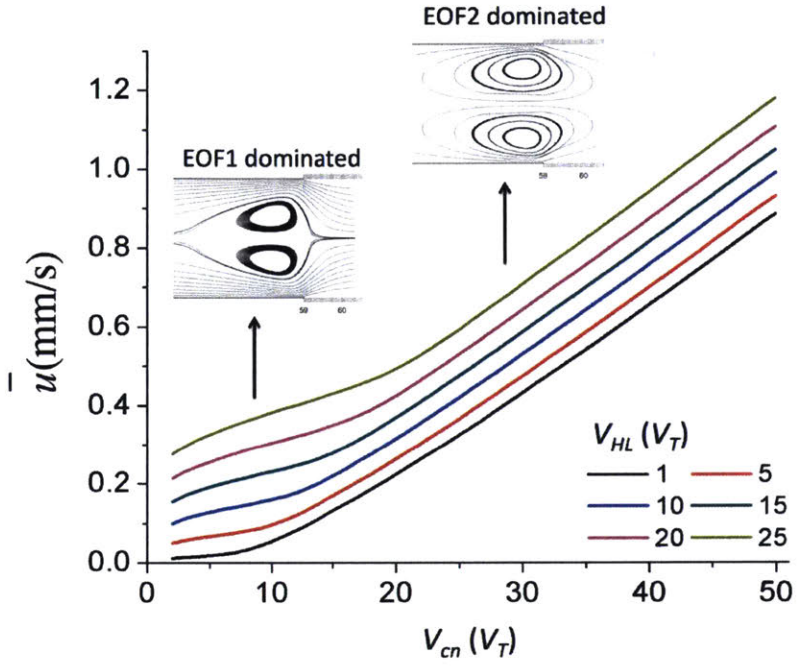


**Fig. A1-3-4.** Dependence of the net fluid velocity $\bar{u}$ on $V_{HL}$ and $V_{cn}$. When $V_{cn}$ is small, $\bar{u}$ is dominated by EOF1, which is approximately linear with $V_{cn}$. When $V_{cn}$ is large, $\bar{u}$ is dominated by EOF2, which is linear with $V_{cn}$ with a higher slope than that of the EOF1-dominated regime.

## A1.4. Effect of the electrophoretic mobility of buffer ions

We will only discuss symmetric electrolytes, where the electrophoretic mobility of the cation and anion equals ($\mu_1 = \mu_2$). We will simply use $\mu_2$ to refer to the electrophoretic mobility of the buffer ions.

The high electrophoretic mobility of buffer ions accelerates the transport of cations through the ion depletion zone and the nanochannels, and the repulsion of anions from the ion depletion zone, thereby forming ion depletion zones with lower ion concentrations, as shown in Fig. A1-4-1(a). Consequently, thicker extended space charge layers are formed in the ion depletion zone in buffers of higher ion mobility, as indicated by the color maps in Fig. A1-4-1(b). According to the Poisson equation, more abrupt changes of the electric field exist in the ion depletion zone at higher ion mobility, which leads to stronger electric fields, as indicated by the arrows in Fig. A1-4-1(b). As a result, the non-equilibrium EOF in the ion depletion zone is accelerated and the trapping of the analyte is enhanced, leading to higher CFs.

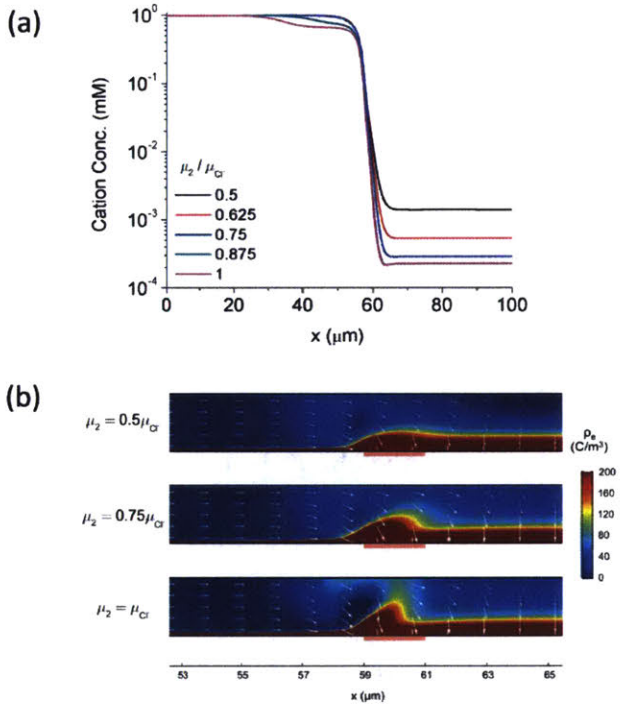


**Fig. A1-4-1.** Effect of the electrophoretic mobility of buffer ions. (a) Cation concentration profiles at different ion mobility. (b) The space charge density (color map) and the electric field (arrows plotted in natural logarithm-scale at different ion mobility.

## A1.5. Meshing issues

We adopted non-uniform distributed meshes to discretize the fluid domain. In the regions near the surface of the channel wall, the intersection of the channel wall and the membrane, as well as the inlet and outlet of the microchannel, the density of the mesh is increased significantly. While in the other regions, relatively coarse meshes are used. For example, to discretize the half width (2 μm) of the microchannel, we use a geometric sequence of 40 elements, with the maximum size being 12000 times larger than the minimum size (0.428 μm near the center of the microchannel and 0.036 nm near the charged surface, respectively). Inside the Electrical Double Layer (~10 nm), there are ~20 layers of exponentially decreased meshes, which provides sufficient details for the physical fields, while total number of meshes is kept small. Similarly, the 1 μm length of the membrane is discretized into 60 elements with the maximum size (in the middle) 30 times larger than the minimum size near the intersection of the membrane and the channel wall. This provides good approximation of the sharp changes of fields like electric potentials, fluid velocities, and ion fluxes at the intersection regions.

To further prove that the simulation is converged and mesh independent, we studied the results of concentration factor, maximum electric field and maximum velocity in the axial direction along the center line of the microchannel using increased mesh densities up to 10 times of our original mesh. The parameters are $Z_3$=-2, $D_3$=$D_2$/4, and $V_{cn}$=14$V_T$. From results in the table below, we can find that the differences are negligibly trivial, and there is no clear trend for increasing mesh density. Therefore, we believe that the difference between them is caused largely by random truncation errors, instead of by insufficient mesh densities.

**Table A1-5-1.** Comparison between different meshing densities.

| Relative mesh density | CF | Max(Ex ) (V/cm) | Max ($U_x$)(mm/s) |
|---|---|---|---|
| 1 | 304.7901175 | 229.486504707708 | 0.47307413622658 |
| 2 | 304.7901175 | 229.486504709585 | 0.47307413633830 |
| 3 | 304.7901174 | 229.486504707187 | 0.47307413631592 |
| 4 | 304.7901175 | 229.486504708426 | 0.47307413632509 |
| 5 | 304.7901174 | 229.486504705944 | 0.47307413618178 |
| 6 | 304.7901175 | 229.486504709408 | 0.47307413632049 |
| 7 | 304.7901176 | 229.486504710507 | 0.47307413632845 |
| 8 | 304.7901176 | 229.486504710479 | 0.47307413627204 |
| 9 | 304.7901174 | 229.486504707839 | 0.47307413632964 |
| 10 | 304.7901175 | 229.486504707485 | 0.47307413618932 |

# Appendix 2. Details of specific enrichment of target biomolecules

## A2.1 Alternative packaging scheme of the device

For applications where the sample volume is small (e.g. tens of microliters), an alternative packaging scheme could be used to adjust the hydrostatic pressure as needed, regardless of the sample volume. As shown in Fig. A2-1-1(a), after the device is fabricated as described in the main text, a pipet tip (of a desired volume) is cut at the narrow end and inserted into the inlet as the reservoir, and an Ag/AgCl electrode is inserted into the reservoir for electrical connection. At the outlet, an Ag/AgCl electrode and a Tygon tubing (0.5 mm inner diameter and 1.52 outer diameter) are fixed in a PDMS slab and bonded to the PDMS chip. One can therefore adjust the hydrostatic pressure by simply controlling the liquid level difference between the inlet and the lower end of the tubing. A 0.2 ml PCR tube is used to collect the waste from the lower end of the tubing. Fig. A2-1-1(b) shows a photo of the device packaged using this scheme.

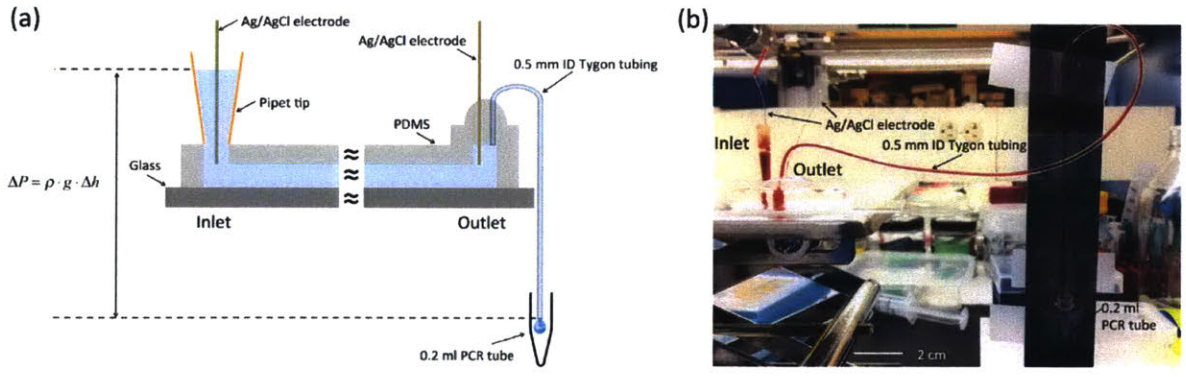


**Fig. A2-1-1.** (a) Alternative packaging scheme of the device. (b) Photo of the device packaged using this scheme.

The fabrication process of this packaging scheme is shown in Fig. A2-1-2 and described as follows:

A1. The device is fabricated as described in the main text.

A2. An access hole with a diameter of 0.5 mm and an access hole with a diameter of 1.5 mm are punched in a PDMS slab (5 mm long, 5 mm wide, 3 mm thick). An Ag/AgCl electrode is inserted into the 0.5 mm access hole, and a Tygon tubing is inserted into the 1.5 mm access hole.

A3. The device and the PDMS slab are treated with oxygen plasma. Afterwards, the PDMS slab containing the electrode and tubing is bonded onto the upper PDMS surface of the device.

B1. Uncured PDMS is poured onto the PDMS slab in order to seal the outlet.

B2. The device is incubated at 60°C for 60 min in an oven to cure the PDMS.

B3. Finally, a pipet tip is inserted into the inlet as the reservoir.

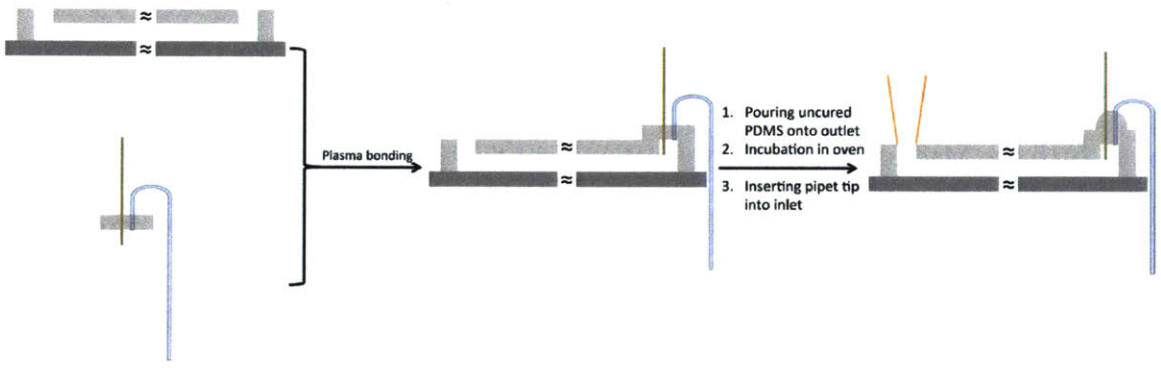


**Fig. A2-1-2.** Fabrication process of the packaging scheme.

## A2.2 Data processing

A2.2.1 Measurement of fluorescence intensity and back-propagation distance

We did time-lapse imaging to record the temporal evolution of the electrokinetic concentration behaviors. The field of view was fixed except when the concentration plugs back-propagated near the left end of the field of view. The field of view was then shifted left to allow for subsequent imaging. Fig. A2-2-1(a) is a stitched image showing the first field of view (used for imaging when $t<100$ s) and the second field of view (used for imaging during $100 \text{ s}<t<280$ s). The shift distance is added to the total back-propagation distance.

The fluorescence intensities of DNA concentration plugs and their back-propagation distances are measured using the following procedure:

A. Raw fluorescence images were opened with ImageJ.

B. As shown in Fig. A2-2-1(a), a region of interest (ROI) is selected on each channel of interest. The width of the ROI (21 pixels) equals that of the channel (100 μm).

C. The fluorescence profile of the ROI is measured using the Plot Profile function under the Analyze tab of ImageJ, which is plotted in Fig. A2-2-1(b).

D. The peak intensity of the fluorescence profile in each channel is extracted in Microsoft Excel 2010 for Mac using the MAX function, and the back-propagation distance (distance between the fluorescence peak and the left end of Nafion) is extracted in Microsoft Excel 2010 for Mac using the MATCH function.

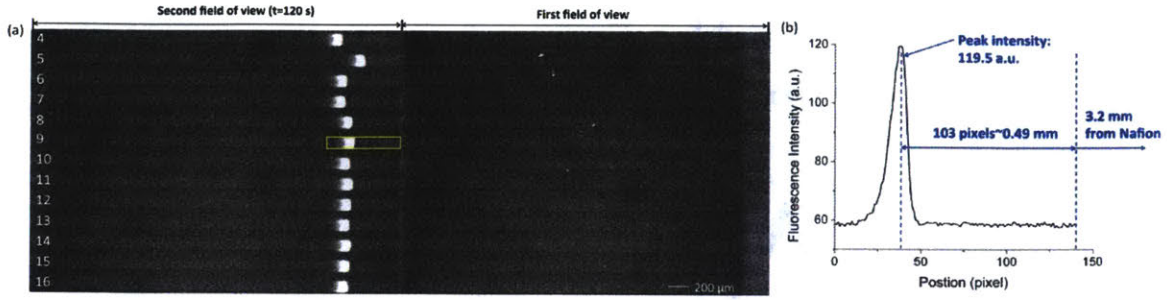


**Fig. A2-2-1.** Data processing procedure. (a) Raw fluorescence images are opened in ImageJ, after which the fluorescence profile in the ROI is measured. The raw image used represents the concentration behavior of DNA (initial concentration: 1 nM) after 2 minutes' concentration in 2.5×PBS with 50 mg/ml BSA (excitation wavelength: ~647 nm). (b) The corresponding fluorescence profile, from which the peak intensity and back-propagation distance are extracted.

A2.2.2 Channels used for data processing

Due to the limited field of view under the 10× objective lens, we could image no more than 13 channels per frame, as shown in Fig. A2-2-1(a). In time-lapse imaging, the position of the device was fixed (except the horizontal shift when concentration plugs back-propagated out of the field of view), so we were only able to record the temporal evolution of the concentration behaviors in no more than 13 channels in each experiment. In some experiments, fewer than 13 channels per frame were imaged, due to imperfect positioning of the device. To be consistent, we used channels #9-#16 (the lower half) for data processing. This is justified by the highly uniform concentration behaviors among the 16 channels.

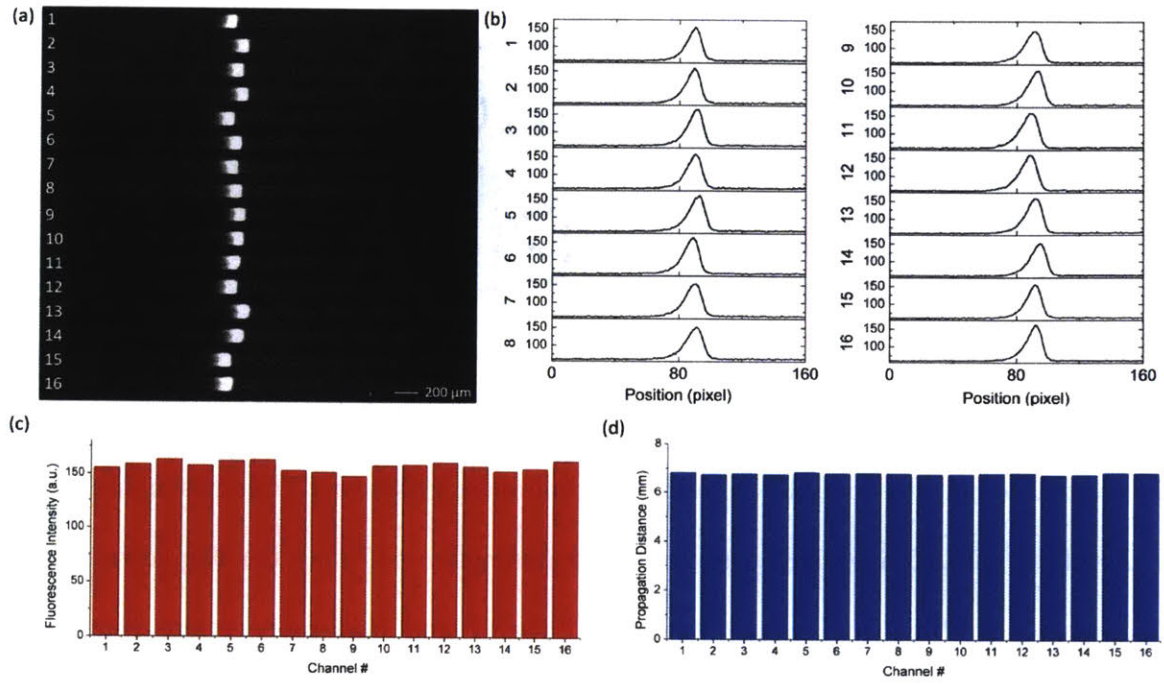


**Fig. A2-2-2.** Highly uniform concentration behaviors among the 16 channels. (a) Stitched fluorescence image of the 16 channels after 5 minutes' concentration in 2.5 ×PBS with 50 mg/ml BSA. The right end of the image is ~4.96 mm from Nafion. (b) The corresponding fluorescence profiles of the 16 channels. The y-axises are the fluorescence intensities (a.u.). The fluorescence profiles are aligned by the peak on the x-axis. (c) The distribution of peak fluorescence intensities. (d) The distribution of propagation distances.

In time-lapse imaging, we needed to fix the device and could not move the field of view back and forth to image all the channels. However, at the end of the experiments, it was possible to adjust the field of view to image all the 16 channels. Fig. A2-2-2 shows a stitched fluorescence image of the 16 channels after 5 minutes' concentration in 2.5 ×PBS with 50 mg/ml BSA, the

corresponding fluorescence profiles, and distributions of the peak fluorescence intensities and propagation distances. Due to the asymmetric design of the device, channels closer to GND experience stronger normal electric fields ($E_N$), which would seemingly cause systematic biases among the 16 channels in the concentration behaviors. However, as shown in Fig. A2-2-2, we did not observe systematic biases among the 16 channels in terms of the fluorescence intensities and propagation distances. The fluorescence intensities and propagation distances among the 16 channels were highly uniform.

The highly uniform concentration behaviors among the 16 channels (and even for devices with up to 128 channels) have been dedicatedly revealed in our previous publication [67]. In short, the reasons behind the uniformity are that: (1) The 16 channels are split through evenly bifurcated tree structures and converged through structures mirroring the splitting structures (Fig. 3-3(b)). This ensures that the tangential electric field ($E_T$) and fluid resistance in each channel are theoretically the same. (2) Although the normal electric field ($E_N$) along the Nafion membrane is inherently different for the 16 channels due to the asymmetric design, the effects of EN on the concentration speed and back-propagation distance were found to be negligible, which was speculated to be due to the high conductivity of Nafion [67].

In summary, although random errors may lead to variations between channels, the systematic biases among the 16 channels are negligible in terms of the concentration behaviors. This fact allows us to use data from the lower half of the channels to represent the performance of the whole device.

A2.2.3 Statistical presentation of the data

Each condition was tested three times using three different devices. For each test, as previously mentioned, channels #9-#16 were studied. As an example, Fig. A2-2-3 shows the fluorescence intensities and propagation distances of 8 channels in all the three runs in 2.5×PBS with 50 mg/ml BSA at t=5 min, and the analysis of variance (ANOVA) of these data.

(a)

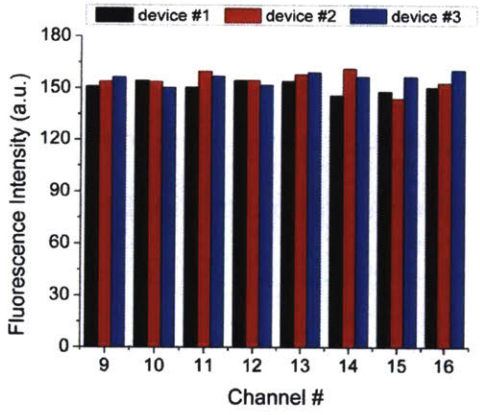


(b)

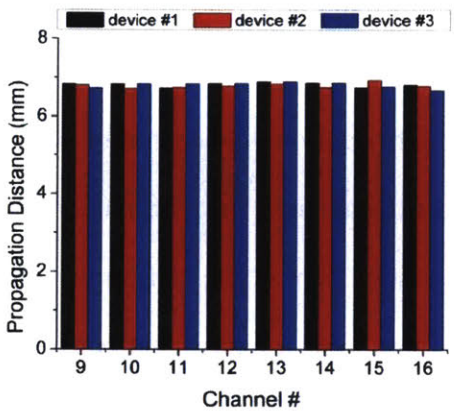


(c)

| Device # | N | Mean | Std. Deviation |
|---|---|---|---|
| 1 | 8 | 151.15 | 3.1369 |
| 2 | 8 | 154.7438 | 5.2979 |
| 3 | 8 | 156.0075 | 3.4501 |
| Total | 24 | 153.9671 | 4.4247 |

| Source | Sum of Squares | Degree of Freedom | Mean Square | F ($F_{0.05}$) |
|---|---|---|---|---|
| Between-devices | 101.6198 | 2 | 50.8099 | 3.06016 (3.4668) N.S. |
| Within-devices | 348.6773 | 21 | 16.6037 | |
| Total | 450.2971 | 23 | | |

(d)

| Device # | N | Mean | Std. Deviation |
|---|---|---|---|
| 1 | 8 | 6.8161 | 0.0579 |
| 2 | 8 | 6.7875 | 0.0691 |
| 3 | 8 | 6.7905 | 0.1041 |
| Total | 24 | 6.798 | 0.0771 |

| Source | Sum of Squares | Degree of Freedom | Mean Square | F ($F_{0.05}$) |
|---|---|---|---|---|
| Between-devices | 0.0039 | 2 | 0.002 | 0.3117 (3.4668) N.S. |
| Within-devices | 0.1327 | 21 | 0.0063 | |
| Total | 0.1367 | 23 | | |

**Fig. A2-2-3.** Statistical analysis of data. (a) Fluorescence intensities and (b) Propagation distances of 8 channels in all the three runs in 2.5×PBS with 50 mg/ml BSA at t=5 min

(excitation wavelength: ~647 nm). Data summary and analysis of variance for (c) fluorescence intensity and (d) propagation distance.

From Fig. A2-2-3, we can know that:

(1) According to Figs. A2-2-2(a-b), within devices, the errors were random errors. We did not observe biases among channels caused by the asymmetric design of the device.

(2) According to Fig. A2-2-2(c), between devices, the difference is not significant. The errors were also random errors.

In the main text, we use the grand mean (mean of all 3×8 points) and the total standard deviation (of 3×8 points) for each data point and the corresponding error bar, respectively.

## A2.3 Calculation of the enrichment factor

Samples spiked with known concentrations of Alexa Fluor 647-labeled DNA were loaded into the chip. No voltage was applied. The fluorescence intensities in the channels were measured using the method described in Section 2. The mean values and standard deviations of the fluorescence intensities are plotted in Fig. A2-3-1.

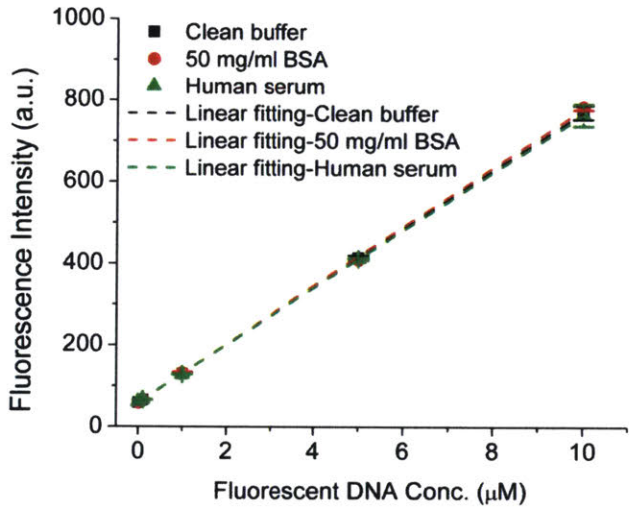


**Fig. A2-3-1.** Relationship between the fluorescence intensity and DNA concentration in different backgrounds. The ion concentration was 1×PBS. The exposure time was 100 ms.

The fitted linear relationships between the fluorescence intensity (F.I.) and DNA concentration ($c$) in samples of different backgrounds are as follows:

Clean buffer: F.I.=71.527$c$+58.529, $R^2$=1;

50 mg/ml BSA: F.I.=72.212$c$+57.375, $R^2$=0.99971;

Human serum: F.I.=70.54$c$+59.039, $R^2$=0.99999.

Based on the fitted linear relationship between the fluorescence intensity and DNA concentration, the maximum DNA concentration in a concentration plug ($c_{max}$) can be calculated by its peak fluorescence intensity. The enrichment factor of a concentration plug is defined as the ratio of the maximum DNA concentration to the initial DNA concentration ($c_0$, which is 1 nM in this work), i.e. $c_{max}/c_0$.

## A2.4 Measurement of fluid velocity

We first tried to visualize the fluid flows in the channels using the electrically neutral fluorescence dye BODIPY FL. However, this method could only provide order-of-magnitude estimation of the fluid velocity, and failed to work in the presence of proteins of high concentrations. Briefly, we first prepared the device as described in the main text, and loaded samples spiked with 100 μM BODIPY FL into the inlet. Next, we turned on the voltage and captured the motion of the dye along the channels every 100 ms using a fluorescence microscope and a CCD camera. Fig. A2-4-1 shows the fluorescence images that track the motion of the neutral dye along the channels with a time interval of 2000 ms in 0.1×PBS under 100 V and $\Delta P = 0$ using the 4× objective lens. Through the images, we could roughly estimate that the average fluid velocity approximately 1.1 mm/s. However, diffusion and dispersion blurred the boundaries between the fluorescent and non-fluorescent segments of the fluid, which prevented us from accurately measuring the fluid velocity using this method. In fact, accurate measurement of fluid velocity in microfluidics needs to be accomplished by micro-particle image velocimetry (μPIV) or similar methods [119], which require specialized experimental setups. Additionally, we found that, in the presence of proteins of high concentrations (e.g. 50 mg/ml), the neutral dye was concentrated in the concentrator even after the amine reactivity of the dye was quenched by 1 M Tris buffer (pH=8.0) for 24 hours, suggesting that the dye lost electroneutrality due to the non-covalent binding with proteins. Therefore, the neutral dye tracing method for fluid velocity measurement is not adopted for accurate measurement of fluid velocity in this work.

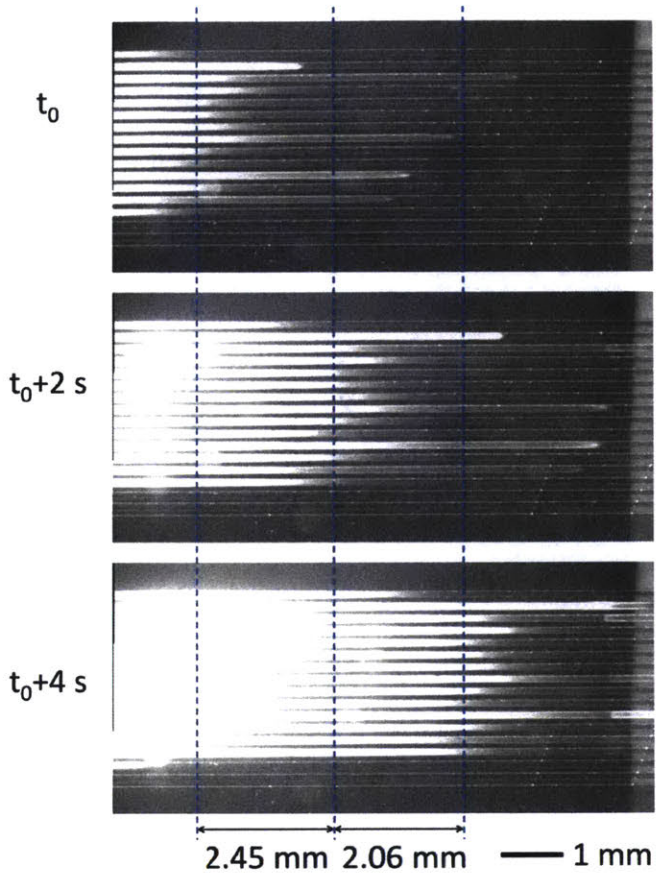


**Fig. A2-4-1.** Fluorescence images showing the motion of a neutral dye (BODIPY FL) along the channels with a time interval of 2000 ms in 0.1×PBS under 100 V and $\Delta P = 0$ using the 4× objective lens, indicating an average fluid velocity of approximately 1.1 mm/s.

We obtained the average fluid velocity in the channels indirectly by measuring the volume of fluid collected from the outlet of the tubing after operating the device for 20 min, using the setup shown in Fig. A2-1-1. Briefly, a 1 ml pipet tip was inserted into the inlet as the reservoir, and 500 μL sample was loaded into the reservoir. The hydrostatic pressure was controlled by

adjusting the height of the tubing outlet. Before the start of the experiments, the tubing was filled with buffer. We ran the device for $t$=20 min and collected liquid from the outlet of the tubing using a 0.2 ml PCR tube, the volume ($\Delta V$) of which was measured by a 20 μL pipet. The total cross-sectional area of the device is $S = 16 \times 100\ \mu m \times 15\ \mu m = 2.4 \times 10^{-8}\ m^2$. Therefore, the average fluid velocity $\bar{u}$ can be calculated as $\bar{u} = \frac{\Delta V}{S \cdot t}$. Based on this method, we obtained the average fluid velocity under various conditions described in the main text, as shown in the tables below.

**Table A2-4-1.** Average fluid velocity at different buffer concentrations, with the protein concentration being zero and the hydrostatic pressure being zero.

| Experimental results \ Buffer conc. | | 0.1×PBS | 1×PBS | 2.5×PBS | 5×PBS |
|---|---|---|---|---|---|
| Volume change (μL/20 min) | Run #1 | 27.2 | 25.2 | 20.2 | 18.4 |
| | Run #2 | 27.0 | 25.2 | 22.0 | 18.2 |
| | Run #3 | 27.6 | 24.6 | 22.2 | 18.6 |
| | Mean | 0.94 | 0.87 | 0.74 | 0.64 |

| | | | | | |
|---|---|---|---|---|---|
| Velocity (mm/s) | Standard Deviation | 0.011 | 0.012 | 0.038 | 0.007 |

**Table A2-4-2.** Average fluid velocity under different hydrostatic pressures in 2.5×PBS with a BSA concentration of 50 mg/ml.

| Hydrostatic Pressure (Pa) / Experimental results | | 0 | 70 | 100 | 120 |
|---|---|---|---|---|---|
| Volume change (μL/20 min) | Run #1 | 20.4 | 25.4 | 28.6 | 29.8 |
| | Run #2 | 20.8 | 26.8 | 28.0 | 30.2 |
| | Run #3 | 21.0 | 26.0 | 28.6 | 28.6 |
| Velocity (mm/s) | Mean | 0.72 | 0.91 | 0.98 | 1.02 |
| | Standard Deviation | 0.011 | 0.025 | 0.012 | 0.029 |

**Table A2-4-3.** Average fluid velocity in human serum under different conditions.

| Conditions | 1×PBS 0 Pa | 2.5×PBS 0 Pa | 5×PBS 0 Pa | 5×PBS 100 Pa | 5×PBS 200 Pa |
|---|---|---|---|---|---|

| Experimental results | | | | | | |
|---|---|---|---|---|---|---|
| Volume change (μL/20 min) | Run #1 | 19.0 | 17.4 | 13.6 | 20.0 | 31.2 |
| | Run #2 | 18.4 | 18.0 | 14.6 | 19.8 | 28.0 |
| | Run #3 | 19.6 | 16.2 | 12.0 | 18.8 | 27.8 |
| Velocity (mm/s) | Mean | 0.66 | 0.60 | 0.47 | 0.68 | 1.01 |
| | Standard Deviation | 0.021 | 0.032 | 0.046 | 0.023 | 0.066 |

## A2.5 Stability of the electric current

We applied the DC voltage (100 V) using a DC power supply (Stanford Research Systems, Sunnyvale, CA) and monitored the electric current with it, which has a resolution of 0.01 mA. Fig. A2-5-1 shows the temporal evolution of the electric current in different ionic strengths. For each ionic strength, three devices were tested. The electric current was relatively stable even in 5×PBS for the whole course of time (15 min). Potential factors, such as electrode reactions and membrane degradation, did not cause significant instabilities of the electric current.

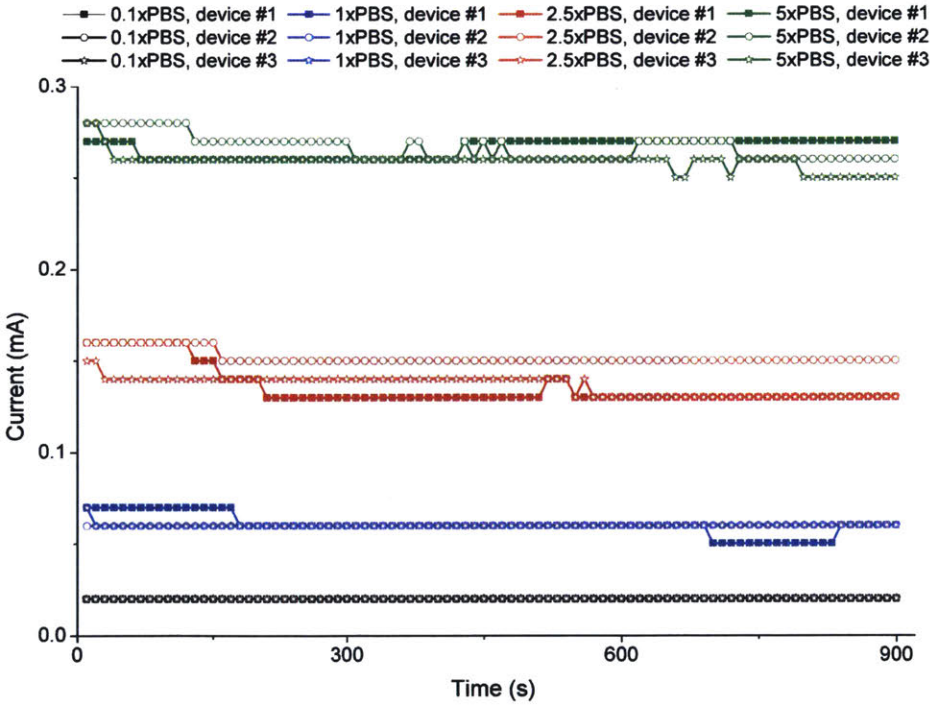


**Fig. A2-5-1.** Temporal evolution of the electric current in different ionic strengths. Three devices were tested for each ionic strength.

## A2.6 Temporal evolution of the DNA concentration plugs under 70 Pa and 120 Pa

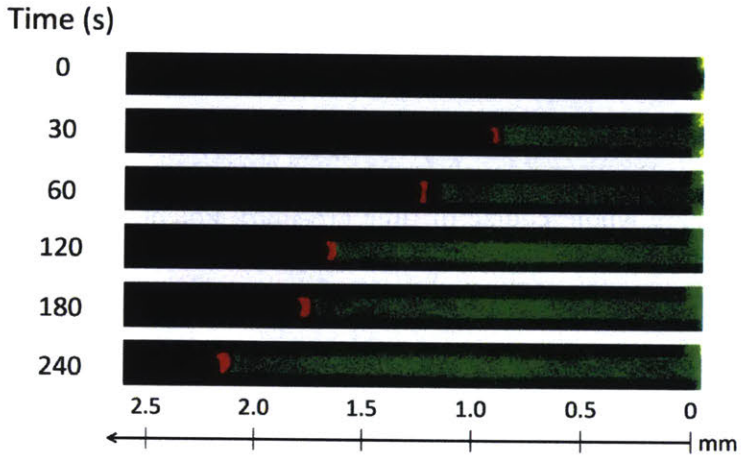


**Fig. A2-6-1.** Temporal evolution of the DNA concentration plugs under 70 Pa in 2.5×PBS with 50 mg/ml BSA in the 9th channel.

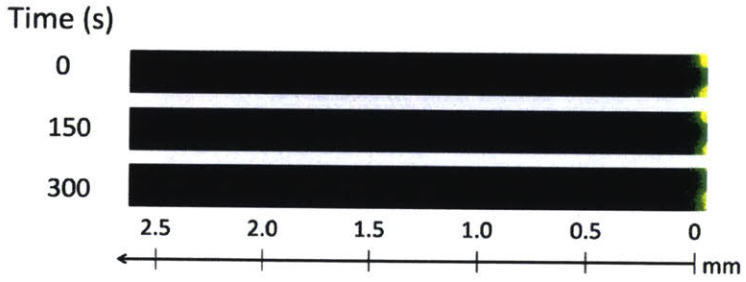


**Fig. A2-6-2.** Temporal evolution of the DNA concentration plugs under 120 Pa in 2.5×PBS with 50 mg/ml BSA in the 9th channel.

# Appendix 3. Details of the hierarchical electrokinetic concentrator

## A3.1 Rationale of device design

Having the two stages dramatically different in dimensions function independently without cross-interference yet enabling rapid transfer of biomolecules between them is challenging. HOLMES solves this problem by relayed transfer and reconcentration of biomolecules among the hierarchical stages via controlling the electrical configurations and ON/OFF states of side outlets. The enabling features of this design are as follows: (1) The ON state of the side outlets allows the regular concentration operation of each stage, and the OFF state allows the transfer of biomolecules to the latter stage; (2) The active concentration stage takes the majority of the voltage drop because of its dominant electrical resistance (due to much smaller cross-sectional area), which electrically inactivates the prior stage(s) to suppress their unwanted trapping effects and hence avoid electrical cross-interference; (3) Most crucially, relayed transfer of biomolecules between stages with only 10- to 100-fold dimension difference is much faster (taking minutes) than directly from the large-volume first stage to the low-throughput final stage with as high as $10^5$-fold dimension difference (taking hours).

## A3.2 Device fabrication

The fabrication process of the vertically stacked 38400-plex device is described as follows and illustrated in Fig. A3-1.

A: Fabrication of the bottom layer

A1. PDMS was poured onto the silicon mold and cured at 65°C for 3 hours. The cured PDMS was peeled off from the silicon mold and had access holes punched.

A2. The Nafion nanochannel networks were patterned on a glass slide using the micro-flow patterning technique. Specifically, a 800 μm wide and 50 μm deep PDMS microchannel was reversibly attached to a glass slide, followed by loading a droplet of Nafion resin (20 wt % solution in lower aliphatic alcohol/$H_2O$ mix, Sigma-Aldrich, St. Louis, MO) to one end of the microchannel. After the Nafion resin filled the microchannel by syringe sucking from the other end, the PDMS microchannel was peeled off from the glass slide and the glass slide was placed on a hotplate at 95°C for 5 min to form the nanochannel network (~1 μm thick.). This process was repeated until the nanochannel networks of all stages were patterned.

A3. The microchannel-patterned PDMS and the nanochannel network-patterned glass slide were treated with oxygen plasma (Femto Science, Gyeonggi-Do, Korea), and irreversibly bonded under a stereo microscope.

B: Fabrication of the upper layers

B1: Uncured PDMS was spin-coated (POLOS spin coater 150i, Germany) on the silicon mold at 200 rpm for 1 min, and cured at 120°C for 3 min. Then the PDMS thin layer was peeled off from the silicon mold, which had a thickness of ~1 mm.

B2: Nafion nanochannel network was patterned on a transparent silicone sheet (0.01 inch thick, Green Rubbers Company, Woburn, MA) using the aforementioned micro-flow patterning technique.

B3: The microchannel-patterned PDMS and nanochannel network-patterned silicone sheet were treated with oxygen plasma, and irreversibly bonded under a stereo microscope.

B4: Access holds were punched through the bonded PDMS-silicone sheet.

This process was repeated 11 times to fabricate 11 individual upper layers.

C: The 11 upper layers were bonded onto the bottom layer one by one by plasma bonding. The use of the silicone sheets was critical for the success of the 3D device fabrication, because it provided strong bonding between the PDMS layers.

D: Pellet Ag/AgCl electrodes (A-M systems, Sequim, WA) were inserted into all the reservoirs and Tygon non-DEHP microbore tubings were inserted into the outlets. The sealing layer was then bonded onto the 3D-stacked device. Uncured PDMS was poured to the outlets and cured to form tight sealing (65°C for 1 hour).

### A3.3 Optimization of electric field

The electric field is calculated by the ratio of the voltage to the x-directional distance between the inlet and outlet(s). As shown in Fig. A3-2(a), at low electric fields (*e.g.* 10 V/cm), the ion depletion zone was not sufficiently developed, and the electric field thereof was not strong enough to completely trap the biomolecules. Biomolecules could form "protrusion" into the ion depletion zone and leaked downstream. The trapping effect improved as the electric field increased. However, at 100 V/cm, strong electroconvections were formed in the depletion zone, and the vortices started to carry the biomolecules into the depletion zone and cause leakage. To minimize the effect of vortices on the concentration performance, we added 0.01% BSA in the sample as the sacrificial spacer, which concentrated between the DNA and vortices and shielded the effect of vortices on the DNA concentration plug. As shown in Fig. A3-2(a), with BSA added, the concentration plug had a uniform profile even at 100 V/cm. As shown in Fig. A3-2(b), the concentration factor generally increased with the electric field, though higher variation of the concentration factor was observed at 100 V/cm due to vortex-induced dispersion of the concentration plugs (w/o BSA). Fig. A3-2(c) shows the fluorescence profile along the microchannel with 1 μM DNA concentrated at 80 V/cm. While the fluorescence of 1 μM DNA was clearly observable, the fluorescence intensity past the depletion zone was indistinguishable from the background. The DNA concentration past the depletion zone was no higher than 10 nM, indicating DNA trapping efficiency of at least 99%. Overall, we used 80 V/cm as the starting value, and fine-adjusted the voltages applied at different stages. Higher electric fields were applied at latter stages to reduce band broadening at high concentration factors. The voltages used in each stage are described in Methods.

## A3.4 Hydrostatic pressures for rapid transfer of biomolecules between stages

During concentration, the fluid velocity generated by electroosmosis is ~1 mm/s. To facilitate rapid transfer of biomolecules to the latter stage, gravitational flow is superposed on electroosmosis (by hydrostatic pressure) to increase the fluid velocity to ~10 mm/s. The operation flow of a four-stage device includes seven steps: 1st stage concentration, rapid transfer from 1st stage to 2nd stage, 2nd stage reconcentration, rapid transfer from 2nd stage to 3rd stage, 3rd stage reconcentration, rapid transfer from 3rd stage to 4th stage, 4th stage reconcentration. The hydrostatic pressure is calculated by $\rho \cdot g \cdot h$ (water density, gravitational acceleration, height difference), which corresponds to 10 Pa per 1 mm height difference. The height difference between the inlet and outlet(s) is controlled by the height of the end of the tubing. We applied the hydrostatic pressure to rapidly transfer the concentrated biomolecules, until the front of the biomolecules arrived at the entrance of the latter stage. We aimed for the most rapid transfer while keeping the height difference below 50 cm (5000 Pa). The specific conditions were determined by experiments, which are described in Methods.

### A3.5 Standard curve

Standard curve of the fluorescence intensity corresponding to the concentration of Alexa Fluor 647-labeled ssDNA is shown in Fig. A3-3. ssDNA solutions of known concentrations were loaded into the device, and the corresponding fluorescence intensities were measured. The fluorescence intensity was normalized to an exposure time of 8000 ms. An offset of 100 a.u. was added to the original fluorescence intensities (to facilitate log-scale plotting in the figures of the main text).

### A3.6 Protein concentration

The concentration performance of protein (BSA) is shown in Fig. A3-4.

### A3.7 Calculation of amplification/concentration factor

In this work, we used a typical qPCR protocol with a amplicon length of ~100 bp and using Taqman polymerase as the enzyme. The protocol (described in Methods) includes a 3-min initial heating and 2-min thermal cycles. Given a total run time of $T$ (excluding sample preparation time), assuming an ideal exponential duplication, the amplification factor is $2^{\frac{T-3}{2}}$.

We calculated the concentration factor by varying the time of first-stage concentration and fixing the protocol of latter stages. The concentration speed at the first stage is approximately 10000-fold per 15 min. The total operation time of the latter stages are 6.25, 11.83, and 14.88 min for the 640-, 3200-, and 38400-plex devices, respectively. The enhancement factors between the first stages and final stages of the 640-, 3200-, and 38400-

plex devices are approximately 300, 1000, and 10000, respectively. Therefore, given a total run time of $T$, the concentration factors of the three devices are as follows:

$$\text{640-plex: } (T - 6.25) \times \frac{10000}{15} * 300 = 2 \times 10^5 \times (T - 6.25).$$

$$\text{3200-plex: } (T - 11.83) \times \frac{10000}{15} \times 1000 = 6.7 \times 10^5 \times (T - 11.83).$$

$$\text{38400-plex: } (T - 14.88) \times \frac{10000}{15} * 10000 = 6.7 \times 10^6 \times (T - 14.88).$$

### A3.8 Suppression effect of background biomolecules

The electroneutrality condition must be observed in the concentration zone, so volume charge densities of all charged species satisfy the following relation: $\rho_+(\text{cation}) = \rho_-(\text{anion}) + \rho_-(\text{BG}) + \rho_-(\text{target})$ (BG represents background biomolecules)[1]. During the concentration of negatively charged biomolecules, concentrated biomolecules displace anions in the concentration zone, until the anion concentration becomes zero ($\rho_-(\text{anion}) = 0$). The concentrations of background and target biomolecules need to satisfy $q_-(\text{BG}) \cdot c(\text{BG}) + q_-(\text{target}) \cdot c(\text{target}) \leq q_+(\text{cation}) \cdot c(\text{cation})$ ($q$: number of charges per molecule).

We first consider the concentration of HIV p24 in serum with ~100 mg/ml proteins in PBS (150 mM). The charges carried by proteins are calculated by http://protcalc.sourceforge.net. HIV p24 (Accession AAA44868.1, aa 133-363) has 3 negative charges per molecule. We use BSA as the representative protein (1.45 mM for 100 mg/ml), which has 14 negative charges per molecule (Accession NP_851335). The above relation reduces to: $14 \cdot c(\text{BSA}) + 3 \cdot c(\text{p24}) \leq 100\ \text{mM}$. HIV p24 and BSA concentrate

simultaneously in the same region. As soon as BSA concentrates by 5-fold (to 7.25 mM), the "charge allowance" will be reached, which prevents the further concentration of HIV p24.

We then consider the concentration of a 100-bp DNA in a background of 10 ng/ml (0.2 nM) 100-bp DNA in PBS (150 mM). Similarly, the above relation reduces to: $200 \cdot c(\text{BG DNA}) + 200 \cdot c(\text{target DNA}) \leq 100\ \text{mM}$. Target and background DNAs concentrate simultaneously in the same region. As soon as the background DNA concentrates by million-fold, the "charge allowance" will be reached, which prevents the further concentration of the target DNA.

### A3.9 Selective enrichment

The key to selective enrichment is generating a fluid flow that pushes proteins across the electric field barrier while still retaining higher mobility species. The width of the microchannels ($w$=200 μm, except the final stage) is much greater than the depth ($h$=15 μm), so the velocity profile of a gravitational flow (pressure-driven) along the width can be approximately seen as uniform. Let $v_{EO}$ be the electroosmostic velocity and $v_{GF}$ be the gravitational flow velocity. Under a hydrostatic pressure of $\Delta P$, $v_{GF}$ can be calculated as $v_{GF} = \frac{h^2}{12\eta} \cdot \frac{\Delta P}{L}$, where $L$ is the length of the channel and $\eta$ is dynamic viscosity of fluid ($10^{-3}$ Pa*s for water)[2]. Note that because of fluid incompressibility, electroosmotic velocity $v_{EO}$ is constant along the channel, regardless of the local variation of electric field in the electric field barrier. Overall, the velocity component of biomolecules from fluid drag is $v_{GF} + v_{EO}$.

Let $E_{max}$ be the maximum magnitude of the electric field in the electric field barrier in the depletion zone, $\mu$ and $\mu'$ be the electrophoretic mobility of the higher mobility species (*e.g.* DNA-PNA complex, DNA-Ab-target protein complex) and proteins, respectively. In order to filtrate proteins, the velocity from fluid drag must overcome the maximum electrophoretic velocity, *i.e.* $v_{GF} + v_{EO} >= \mu' E_{max}$; in order to still concentrate higher mobility species, the velocity from fluid drag must be less than the maximum electrophoretic velocity, *i.e.* $v_{GF} + v_{EO} < \mu E_{max}$. The gravitational flow needs to satisfy the following condition: $\mu' E_{max} - v_{EO} <= v_{GF} < \mu E_{max} - v_{EO}$.

Because of the difficulty in theoretically predicting the maximum electric field, we optimized the gravitational flows experimentally using fluorescently labeled high-mobility capture Ab in 0.25× human serum. Selective enrichment at the first stage is most important, as it directly filtrates the background proteins from input samples. We first optimized the hydrostatic pressure for the first stage of the 3200-plex device ($L$=81 mm), through which the optimal hydrostatic pressure of 850-950 Pa ($v_{GF}$=0.20-0.22 mm/s) was obtained. Therefore, a gravitational flow of ~0.20 mm/s superposed on electroosmosis (~1 mm/s at 80 V/cm) could realize selective enrichment. Because the gravitational flow is proportional to $\frac{\Delta P}{L}$, the optimal conditions were obtained for other stages and devices by scaling the hydrostatic pressures according to the corresponding lengths. The optimized conditions are described in Methods.

### A3.10 DNA detection

Fluorescence profiles corresponding to the fluorescence images in Figs. 4-5(c), 4-5(f), 4-5(i) are shown in Figs. A3-5(a), A3-5(b), A3-5(c), respectively.

### A3.11 Protein detection by ELISA

The standard curve of cTnI detection by ELISA and cTnI concentrations of patient plasma samples measured by ELISA are shown in Fig. A3-6.

### A3.12 Protein detection by HOLMES

The standard curve of cTnI detection by HOLMES and cTnI concentrations of patient plasma samples measured by HOLMES are shown in Fig. A3-7.

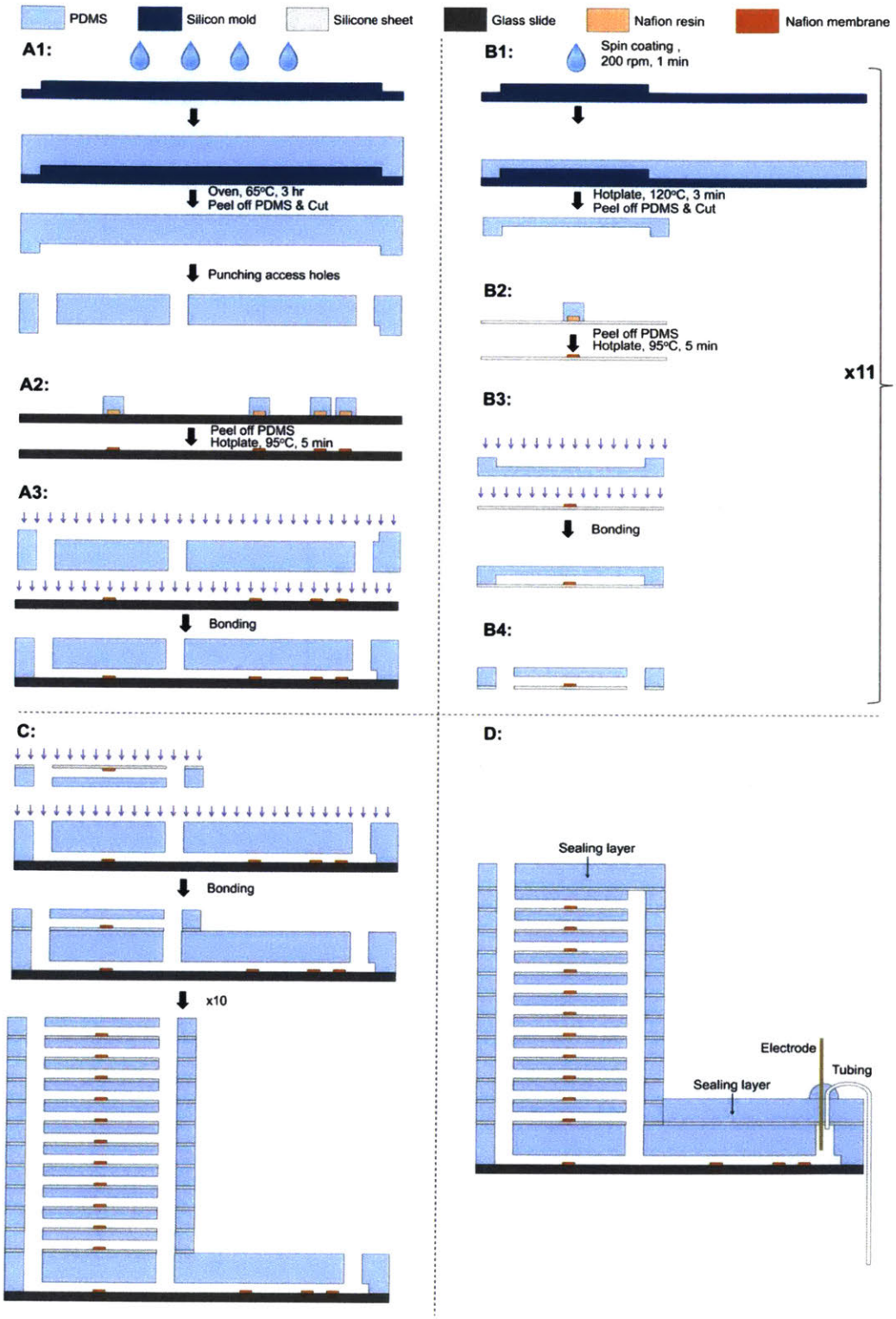
PDMS
Silicon mold
Silicone sheet
Glass slide
Nafion resin
Nafion membrane
A1:
Oven, 65°C, 3 hr
Peel off PDMS & Cut
Punching access holes
A2:
Peel off PDMS
Hotplate, 95°C, 5 min
A3:
Bonding
B1:
Spin coating ,
200 rpm, 1 min
Hotplate, 120°C, 3 min
Peel off PDMS & Cut
B2:
Peel off PDMS
Hotplate, 95°C, 5 min
B3:
Bonding
B4:
x11
C:
Bonding
x10
D:
Sealing layer
Electrode
Tubing
Sealing layer

**Fig. A3-1.** Fabrication of the 38400-plex device.

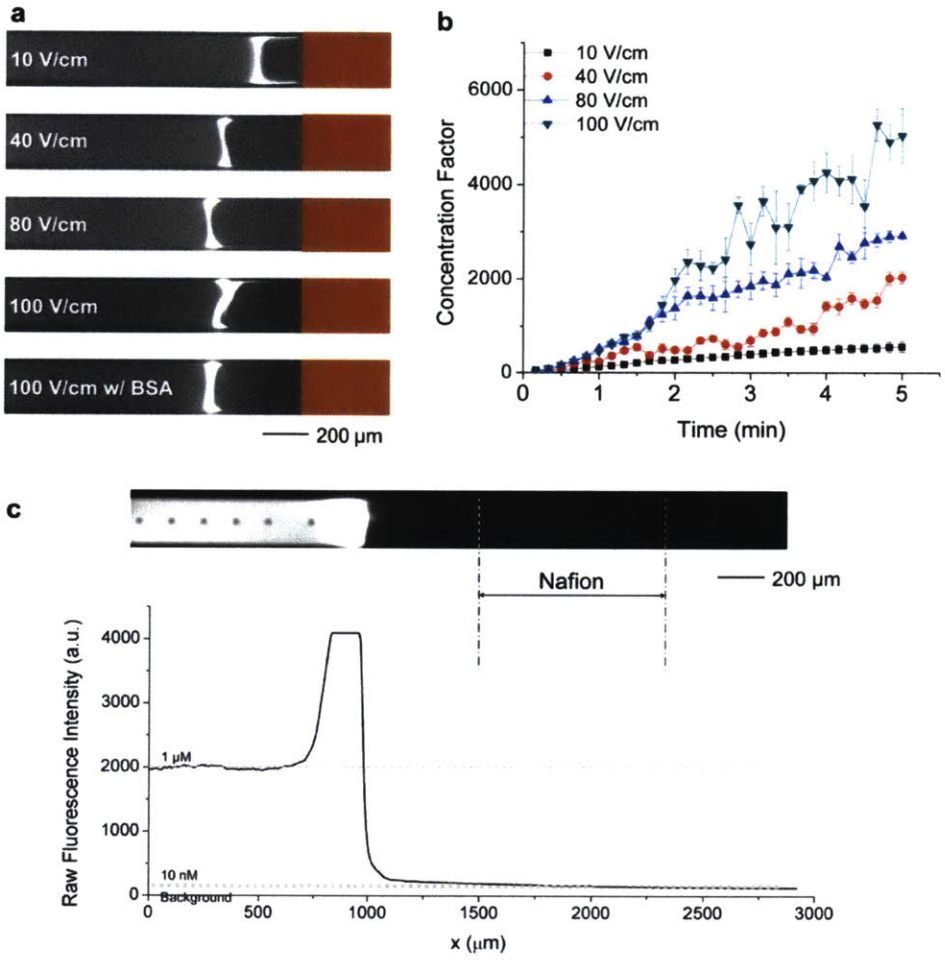


**Fig. A3-2.** Effect of electric field on concentration performance. (a) The profiles of concentration plugs under different electric fields (t=150 s). (b) The dependence of concentration factor on electric field. (c) The raw fluorescence intensity profile along a channel at 80 V/cm. 1 μM ssDNA in 0.1×PBS was tested. The exposure time is 3000 ms.

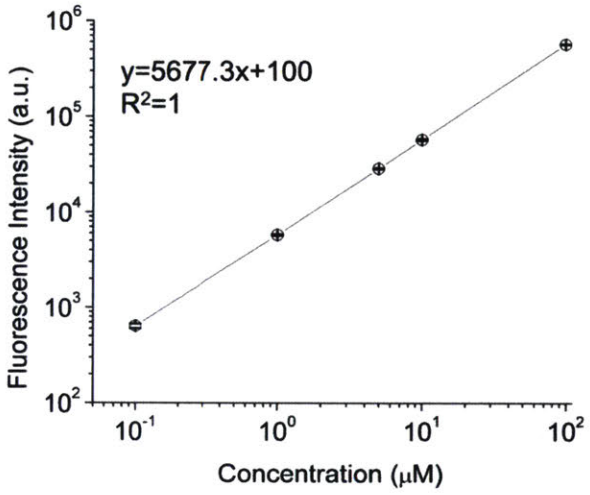


**Fig. A3-3.** Standard curve of the fluorescence intensity corresponding to the concentration of Alexa Fluor 647-labeled ssDNA.

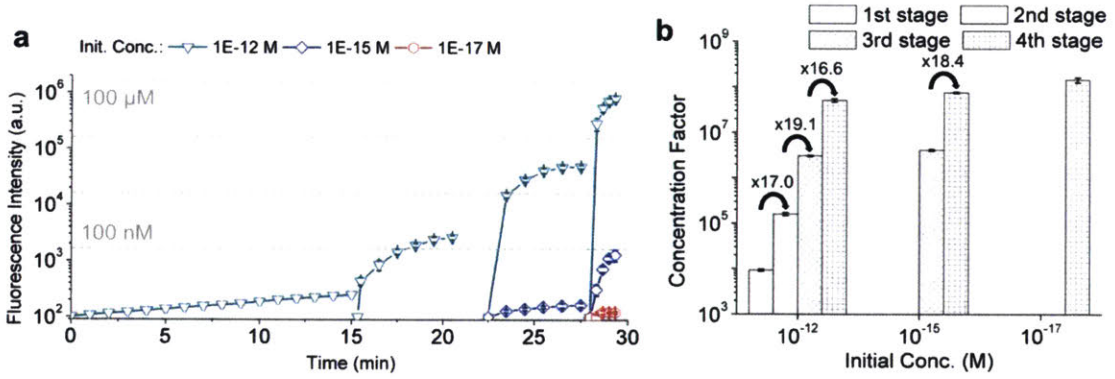


**Fig. A3-4.** Concentration of Alexa Fluor 555-labeled BSA in 0.1×PBS in the 38400-plex device. (a) The temporal evolution of the average peak fluorescence intensities of the concentration plugs at the active stages at different concentrations. (b) The concentration factors at different stages and different initial concentrations.

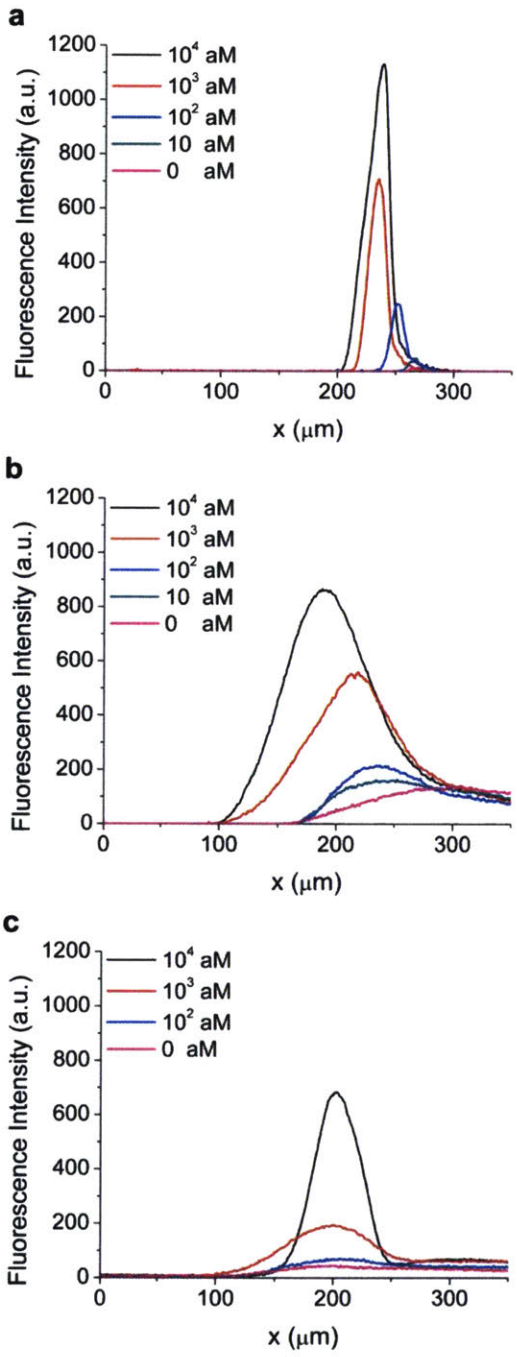
a
b
c
Fluorescence Intensity (a.u.)
x (μm)
10^4 aM
10^3 aM
10^2 aM
10 aM
0 aM
0
100
200
300
400
600
800
1000
1200

**Fig. A3-5.** Fluorescence profiles corresponding to the fluorescence images in Figs. 4-5(c), 4-5(f), 4-5(i), respectively.

a

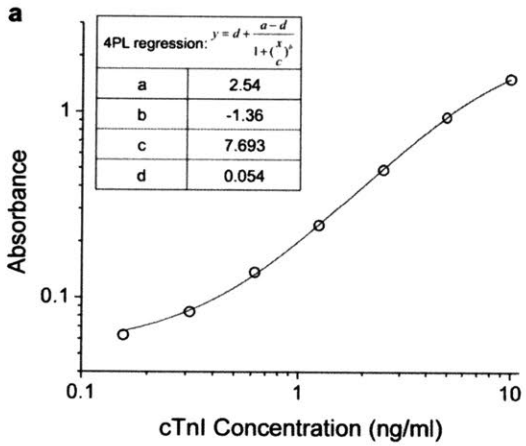


b

| Patient # | Absorbance (avg. ± s.d.) | Concentration (ng/ml) |
|---|---|---|
| 1 | 0.029±0.006 | Not detected |
| 2 | 0.467±0.029 | 2.36±0.14 |
| 3 | 0.065±0.001 | 0.15±0.01 |
| 4 | 0.067±0.003 | 0.16±0.03 |
| 5 | 0.446±0.040 | 2.26±0.20 |
| 6 | 0.627±0.023 | 3.19±0.12 |
| 7 | 0.029±0.001 | Not detected |
| 8 | 0.022±0.003 | Not detected |
| 9 | 0.662±0.035 | 3.37±0.18 |

**Fig. A3-6.** cTnI detection by ELISA. (a) Standard curve of ELISA (fitted by four parameters logistic regression) measured by spiking recombinant cTnI in reagent diluent. (b) cTnI concentrations of patient plasma samples measured by ELISA.

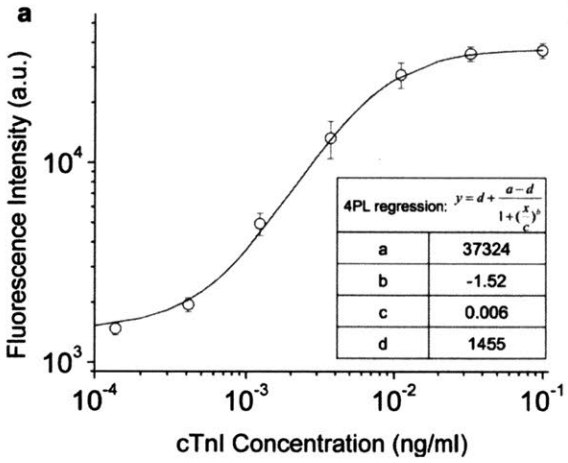


b

| Dilution | Patient # | Fluorescence (avg. ± s.d.) | Concentration (ng/ml) | Original Conc. (ng/m) |
|---|---|---|---|---|
| 4-fold | 1 | 12216±1009 | 0.0033±0.0003 | 0.0133±0.0012 |
| | 7 | 8934±1919 | 0.0024±0.0005 | 0.0097±0.0021 |
| | 8 | 3514±459 | 0.0012±0.0001 | 0.0037±0.0006 |
| 100-fold | 3 | 7180±2078 | 0.0019±0.0006 | 0.1943±0.0556 |
| | 4 | 8753±2126 | 0.0024±0.0006 | 0.2366±0.0569 |
| 1000-fold | 2 | 9458±1829 | 0.0026±0.0005 | 2.5567±0.4925 |
| | 5 | 8825±1501 | 0.0024±0.0004 | 2.3704±0.4073 |
| | 6 | 10749±1574 | 0.0029±0.0004 | 2.9117±0.4398 |
| | 9 | 13464±2062 | 0.0037±0.0006 | 3.7097±0.6306 |

**Fig. A3-7.** cTnI detection by HOLMES. (a) Standard curve of HOLMES (fitted by four parameters logistic regression) measured by spiking recombinant cTnI in reagent diluent. The LOD is ~$10^{-4}$ ng/ml (~1 fM). The lower sensitivity compared to HIV p24 detection (~0.01 fM) was attributed to the lower affinities of the cTnI antibody pair. (b) cTnI concentrations of patient plasma samples measured by HOLMES.

# Bibliography


[1] S. O. Kelley, "What are clinically relevant levels of cellular and biomolecular analytes?," *ACS sensors*, vol. 2, no. 2, pp. 193–197, 2017.

[2] T. Shi *et al.*, "IgY14 and SuperMix immunoaffinity separations coupled with liquid chromatography–mass spectrometry for human plasma proteomics biomarker discovery," *Methods*, vol. 56, no. 2, pp. 246–253, 2012.

[3] G. Wu, R. H. Datar, K. M. Hansen, T. Thundat, R. J. Cote, and A. Majumdar, "Bioassay of prostate-specific antigen (PSA) using microcantilevers," *Nat. Biotechnol.*, vol. 19, no. 9, p. 856, 2001.

[4] J. Wang, J. Hou, H. Zhang, Y. Tian, and L. Jiang, "Single nanochannel-aptamer-based biosensor for ultrasensitive and selective cocaine detection," *ACS Appl. Mater. Interfaces*, vol. 10, no. 2, pp. 2033–2039, 2018.

[5] S. Afsahi *et al.*, "Novel graphene-based biosensor for early detection of Zika virus infection," *Biosens. Bioelectron.*, vol. 100, pp. 85–88, 2018.

[6] D. Sarkar, W. Liu, X. Xie, A. C. Anselmo, S. Mitragotri, and K. Banerjee, "MoS2 field-effect transistor for next-generation label-free biosensors," *ACS Nano*, vol. 8, no. 4, pp. 3992–4003, 2014.

[7] S. O. Kelley, C. A. Mirkin, D. R. Walt, R. F. Ismagilov, M. Toner, and E. H. Sargent, "Advancing the speed, sensitivity and accuracy of biomolecular detection using multi-length-scale engineering," *Nat. Nanotechnol.*, vol. 9, no. 12, p. 969, 2014.

[8] T. Notomi *et al.*, "Loop-mediated isothermal amplification of DNA," *Nucleic Acids*

*Res.*, vol. 28, no. 12, pp. e63–e63, 2000.

[9] I. M. Lobato and C. K. O'Sullivan, "Recombinase polymerase amplification: Basics, applications and recent advances," *Trac Trends Anal. Chem.*, vol. 98, pp. 19–35, 2018.

[10] M. Vincent, Y. Xu, and H. Kong, "Helicase-dependent isothermal DNA amplification," *EMBO Rep.*, vol. 5, no. 8, pp. 795–800, 2004.

[11] "http://thescienceinfo.com/components-of-polymerase-chain-reaction/." .

[12] "https://antisensescienceblog.wordpress.com/2013/12/04/a-cornerstone-of-molecular-biology-the-pcr-reaction/." .

[13] "https://www.neb-online.de/en/pcr-and-dna-amplification/isothermal-amplification." .

[14] "http://technologyinscience.blogspot.com/2013/07/helicase-dependent-amplificationdna.html#.XZ1LuC2ZPPA." .

[15] C. Eid and J. G. Santiago, "Isotachophoresis applied to biomolecular reactions," *Lab Chip*, vol. 18, no. 1, pp. 11–26, 2018.

[16] B. Ma, Y.-Z. Song, J.-C. Niu, and Z.-Y. Wu, "Highly efficient sample stacking by enhanced field amplification on a simple paper device," *Lab Chip*, vol. 16, no. 18, pp. 3460–3465, 2016.

[17] R. Bharadwaj and J. G. Santiago, "Dynamics of field-amplified sample stacking," *J. Fluid Mech.*, vol. 543, pp. 57–92, 2005.

[18] R. T. Kelly and A. T. Woolley, "Electric field gradient focusing," *J. Sep. Sci.*, vol. 28, no. 15, pp. 1985–1993, 2005.

[19] J. W. Quist, *Single-electrolyte isotachophoresis: on-chip analyte focusing and separation*. Leiden Academic Center for Drugs Research, Department Analytical

Biosciences ..., 2014.

[20] D. Ross and L. E. Locascio, "Microfluidic temperature gradient focusing," *Anal. Chem.*, vol. 74, no. 11, pp. 2556–2564, 2002.

[21] "http://microfluidics.stanford.edu/Projects/Archive/tgf.htm." .

[22] Y.-C. Wang, A. L. Stevens, and J. Han, "Million-fold preconcentration of proteins and peptides by nanofluidic filter," *Anal. Chem.*, vol. 77, no. 14, pp. 4293–4299, 2005.

[23] S. H. Ko, Y.-A. Song, S. J. Kim, M. Kim, J. Han, and K. H. Kang, "Nanofluidic preconcentration device in a straight microchannel using ion concentration polarization," *Lab Chip*, vol. 12, no. 21, pp. 4472–4482, 2012.

[24] L. Gong, W. Ouyang, Z. Li, and J. Han, "Force fields of charged particles in micro-nanofluidic preconcentration systems," *AIP Adv.*, vol. 7, no. 12, p. 125020, 2017.

[25] R. B. Schoch, J. Han, and P. Renaud, "Transport phenomena in nanofluidics," *Rev. Mod. Phys.*, vol. 80, no. 3, p. 839, 2008.

[26] K. Huang and R. Yang, "A nanochannel-based concentrator utilizing the concentration polarization effect," *Electrophoresis*, vol. 29, no. 24, pp. 4862–4870, 2008.

[27] P. Kim, S. J. Kim, J. Han, and K. Y. Suh, "Stabilization of ion concentration polarization using a heterogeneous nanoporous junction," *Nano Lett.*, vol. 10, no. 1, pp. 16–23, 2009.

[28] R. K. Anand, E. Sheridan, D. Hlushkou, U. Tallarek, and R. M. Crooks, "Bipolar electrode focusing: tuning the electric field gradient," *Lab Chip*, vol. 11, no. 3, pp. 518–527, 2011.

[29] R. Kwak, S. J. Kim, and J. Han, "Continuous-flow biomolecule and cell concentrator

by ion concentration polarization," *Anal. Chem.*, vol. 83, no. 19, pp. 7348–7355, 2011.

[30] D. Stein, Z. Deurvorst, F. H. J. van der Heyden, W. J. A. Koopmans, A. Gabel, and C. Dekker, "Electrokinetic concentration of DNA polymers in nanofluidic channels," *Nano Lett.*, vol. 10, no. 3, pp. 765–772, 2010.

[31] W. Ouyang *et al.*, "Microfluidic Platform for Assessment of Therapeutic Proteins Using Molecular Charge Modulation Enhanced Electrokinetic Concentration Assays," *Anal. Chem.*, vol. 88, no. 19, pp. 9669–9677, 2016.

[32] L. Gong, W. Ouyang, Z. Li, and J. Han, "Direct numerical simulation of continuous lithium extraction from high Mg2+/Li+ ratio brines using microfluidic channels with ion concentration polarization," *J. Memb. Sci.*, vol. 556, pp. 34–41, 2018.

[33] L. Fu, H. Hou, P. Chiu, and R. Yang, "Sample preconcentration from dilute solutions on micro/nanofluidic platforms: A review," *Electrophoresis*, vol. 39, no. 2, pp. 289–310, 2018.

[34] S. J. Kim, Y.-A. Song, and J. Han, "Nanofluidic concentration devices for biomolecules utilizing ion concentration polarization: theory, fabrication, and applications," *Chem. Soc. Rev.*, vol. 39, no. 3, pp. 912–922, 2010.

[35] D. Hlushkou, R. K. Perdue, R. Dhopeshwarkar, R. M. Crooks, and U. Tallarek, "Electric field gradient focusing in microchannels with embedded bipolar electrode," *Lab Chip*, vol. 9, no. 13, pp. 1903–1913, 2009.

[36] M. Kim, M. Jia, and T. Kim, "Ion concentration polarization in a single and open microchannel induced by a surface-patterned perm-selective film," *Analyst*, vol. 138, no. 5, pp. 1370–1378, 2013.

[37] M. Shen, H. Yang, V. Sivagnanam, and M. A. M. Gijs, "Microfluidic protein preconcentrator using a microchannel-integrated Nafion strip: experiment and modeling," *Anal. Chem.*, vol. 82, no. 24, pp. 9989–9997, 2010.

[38] M. Jia and T. Kim, "Multiphysics simulation of ion concentration polarization induced by nanoporous membranes in dual channel devices," *Anal. Chem.*, vol. 86, no. 15, pp. 7360–7367, 2014.

[39] M. Jia and T. Kim, "Multiphysics simulation of ion concentration polarization induced by a surface-patterned nanoporous membrane in single channel devices," *Anal. Chem.*, vol. 86, no. 20, pp. 10365–10372, 2014.

[40] R. F. Probstein, *Physicochemical hydrodynamics: an introduction*. John Wiley & Sons, 2005.

[41] T. A. Zangle, A. Mani, and J. G. Santiago, "Theory and experiments of concentration polarization and ion focusing at microchannel and nanochannel interfaces," *Chem. Soc. Rev.*, vol. 39, no. 3, pp. 1014–1035, 2010.

[42] I. Cho, W. Kim, J. Kim, H.-Y. Kim, H. Lee, and S. J. Kim, "Non-negligible Diffusio-osmosis inside an ion concentration polarization layer," *Phys. Rev. Lett.*, vol. 116, no. 25, p. 254501, 2016.

[43] Y. Green, R. Eshel, S. Park, and G. Yossifon, "Interplay between nanochannel and microchannel resistances," *Nano Lett.*, vol. 16, no. 4, pp. 2744–2748, 2016.

[44] I. Rubinstein, E. Staude, and O. Kedem, "Role of the membrane surface in concentration polarization at ion-exchange membrane," *Desalination*, vol. 69, no. 2, pp. 101–114, 1988.

[45] A. Plecis, C. Nanteuil, A.-M. Haghiri-Gosnet, and Y. Chen, "Electropreconcentration with charge-selective nanochannels," *Anal. Chem.*, vol. 80, no. 24, pp. 9542–9550, 2008.

[46] S. J. Kim, Y.-C. Wang, J. H. Lee, H. Jang, and J. Han, "Concentration polarization and nonlinear electrokinetic flow near a nanofluidic channel," *Phys. Rev. Lett.*, vol. 99, no. 4, p. 44501, 2007.

[47] S. M. Rubinstein *et al.*, "Direct observation of a nonequilibrium electro-osmotic instability," *Phys. Rev. Lett.*, vol. 101, no. 23, p. 236101, 2008.

[48] E. V. Dydek, B. Zaltzman, I. Rubinstein, D. S. Deng, A. Mani, and M. Z. Bazant, "Overlimiting current in a microchannel," *Phys. Rev. Lett.*, vol. 107, no. 11, p. 118301, 2011.

[49] S. Nam *et al.*, "Experimental verification of overlimiting current by surface conduction and electro-osmotic flow in microchannels," *Phys. Rev. Lett.*, vol. 114, no. 11, p. 114501, 2015.

[50] B. J. Kirby, *Micro-and nanoscale fluid mechanics: transport in microfluidic devices.* Cambridge university press, 2010.

[51] J. H. G. Van Der Stegen, J. Görtzen, J. A. M. Kuipers, J. A. Hogendoorn, and G. F. Versteeg, "Radial distribution of ions in pores with a surface charge," *J. Memb. Sci.*, vol. 183, no. 1, pp. 61–74, 2001.

[52] F. C. Leinweber and U. Tallarek, "Nonequilibrium electrokinetic effects in beds of ion-permselective particles," *Langmuir*, vol. 20, no. 26, pp. 11637–11648, 2004.

[53] I. Rubinstein and B. Zaltzman, "Electro-osmotically induced convection at a

permselective membrane," *Phys. Rev. E*, vol. 62, no. 2, p. 2238, 2000.

[54] R. Kwak, V. S. Pham, K. M. Lim, and J. Han, "Shear flow of an electrically charged fluid by ion concentration polarization: Scaling laws for electroconvective vortices," *Phys. Rev. Lett.*, vol. 110, no. 11, p. 114501, 2013.

[55] V. Pham, Z. Li, K. Lim, J. White, and J. Han, "Direct numerical simulation of electroconvective instability and hysteretic current-voltage response of a permselective membrane," 2012.

[56] J. T. Edward, "Molecular volumes and the Stokes-Einstein equation," *J. Chem. Educ.*, vol. 47, no. 4, p. 261, 1970.

[57] R. K. Anand, E. Sheridan, K. N. Knust, and R. M. Crooks, "Bipolar electrode focusing: faradaic ion concentration polarization," *Anal. Chem.*, vol. 83, no. 6, pp. 2351–2358, 2011.

[58] X. Wei, P. Panindre, Q. Zhang, and Y.-A. Song, "Increasing the detection sensitivity for DNA-morpholino hybridization in sub-nanomolar regime by enhancing the surface ion conductance of PEDOT: PSS membrane in a microchannel," *Acs Sensors*, vol. 1, no. 7, pp. 862–865, 2016.

[59] S. A. Hong, Y.-J. Kim, S. J. Kim, and S. Yang, "Electrochemical detection of methylated DNA on a microfluidic chip with nanoelectrokinetic pre-concentration," *Biosens. Bioelectron.*, vol. 107, pp. 103–110, 2018.

[60] W. Thormann, C.-X. Zhang, J. Caslavska, P. Gebauer, and R. A. Mosher, "Modeling of the impact of ionic strength on the electroosmotic flow in capillary electrophoresis with uniform and discontinuous buffer systems," *Anal. Chem.*, vol. 70, no. 3, pp. 549–

562, 1998.

[61] A. S. Khair and T. M. Squires, "Fundamental aspects of concentration polarization arising from nonuniform electrokinetic transport," *Phys. Fluids*, vol. 20, no. 8, p. 87102, 2008.

[62] C. L. Druzgalski, M. B. Andersen, and A. Mani, "Direct numerical simulation of electroconvective instability and hydrodynamic chaos near an ion-selective surface," *Phys. Fluids*, vol. 25, no. 11, p. 110804, 2013.

[63] E. A. Demekhin, N. V Nikitin, and V. S. Shelistov, "Direct numerical simulation of electrokinetic instability and transition to chaotic motion," *Phys. Fluids*, vol. 25, no. 12, p. 122001, 2013.

[64] N. C. Stellwagen and E. Stellwagen, "Effect of the matrix on DNA electrophoretic mobility," *J. Chromatogr. A*, vol. 1216, no. 10, pp. 1917–1929, 2009.

[65] S. H. Behrens and D. G. Grier, "The charge of glass and silica surfaces," *J. Chem. Phys.*, vol. 115, no. 14, pp. 6716–6721, 2001.

[66] K. Kim, W. Kim, H. Lee, and S. J. Kim, "Stabilization of ion concentration polarization layer using micro fin structure for high-throughput applications," *Nanoscale*, vol. 9, no. 10, pp. 3466–3475, 2017.

[67] S. H. Ko, S. J. Kim, L. F. Cheow, L. D. Li, K. H. Kang, and J. Han, "Massively parallel concentration device for multiplexed immunoassays," *Lab Chip*, vol. 11, no. 7, pp. 1351–1358, 2011.

[68] K. A. Mauritz and R. B. Moore, "State of understanding of Nafion," *Chem. Rev.*, vol. 104, no. 10, pp. 4535–4586, 2004.

[69] W. Ouyang, X. Ye, Z. Li, and J. Han, "Deciphering ion concentration polarization-based electrokinetic molecular concentration at the micro-nanofluidic interface: theoretical limits and scaling laws," *Nanoscale*, vol. 10, no. 32, pp. 15187–15194, 2018.

[70] D. Jantz and J. M. Berg, "Probing the DNA-binding affinity and specificity of designed zinc finger proteins," *Biophys. J.*, vol. 98, no. 5, pp. 852–860, 2010.

[71] V. Hruška and B. Gaš, "Kohlrausch regulating function and other conservation laws in electrophoresis," *Electrophoresis*, vol. 28, no. 1-2, pp. 3–14, 2007.

[72] A. Cannas *et al.*, "Mycobacterium tuberculosis DNA detection in soluble fraction of urine from pulmonary tuberculosis patients," *Int. J. Tuberc. lung Dis.*, vol. 12, no. 2, pp. 146–151, 2008.

[73] Y. Xu, C.-X. Zhang, D. Janasek, and A. Manz, "Sub-second isoelectric focusing in free flow using a microfluidic device," *Lab Chip*, vol. 3, no. 4, pp. 224–227, 2003.

[74] K. J. Freedman, L. M. Otto, A. P. Ivanov, A. Barik, S.-H. Oh, and J. B. Edel, "Nanopore sensing at ultra-low concentrations using single-molecule dielectrophoretic trapping," *Nat. Commun.*, vol. 7, p. 10217, 2016.

[75] P. Smejkal *et al.*, "Microfluidic isotachophoresis: A review," *Electrophoresis*, vol. 34, no. 11, pp. 1493–1509, 2013.

[76] J. H. Lee, Y.-A. Song, and J. Han, "Multiplexed proteomic sample preconcentration device using surface-patterned ion-selective membrane," *Lab Chip*, vol. 8, no. 4, pp. 596–601, 2008.

[77] Z. Pang, N. E. Laplante, and R. J. Filkins, "Dark pixel intensity determination and its

applications in normalizing different exposure time and autofluorescence removal," *J. Microsc.*, vol. 246, no. 1, pp. 1–10, 2012.

[78] A. Zinkova, I. Brynychova, A. Svacina, M. Jirkovska, and M. Korabecna, "Cell-free DNA from human plasma and serum differs in content of telomeric sequences and its ability to promote immune response," *Sci. Rep.*, vol. 7, no. 1, p. 2591, 2017.

[79] M. De *et al.*, "Sensing of proteins in human serum using conjugates of nanoparticles and green fluorescent protein," *Nat. Chem.*, vol. 1, no. 6, p. 461, 2009.

[80] P. E. Nielsen, *Peptide nucleic acids: protocols and applications*. Garland Science, 2004.

[81] J. Däbritz, J. Hänfler, R. Preston, J. Stieler, and H. Oettle, "Detection of Ki-ras mutations in tissue and plasma samples of patients with pancreatic cancer using PNA-mediated PCR clamping and hybridisation probes," *Br. J. Cancer*, vol. 92, no. 2, p. 405, 2005.

[82] W. Ouyang, Z. Li, and J. Han, "Pressure-modulated selective electrokinetic trapping for direct enrichment, purification, and detection of nucleic acids in human serum," *Anal. Chem.*, vol. 90, no. 19, pp. 11366–11375, 2018.

[83] V. Masilamani, V. Trinka, M. Al Salhi, K. Govindaraj, A. P. V. Raghavan, and B. Antonisamy, "Cancer detection by native fluorescence of urine," *J. Biomed. Opt.*, vol. 15, no. 5, p. 57003, 2010.

[84] R. H. Christenson *et al.*, "Comparison of 13 commercially available cardiac troponin assays in a multicenter North American study," *J. Appl. Lab. Med.*, p. jalm-2016, 2017.

[85] T. Omland *et al.*, "A sensitive cardiac troponin T assay in stable coronary artery disease," *N. Engl. J. Med.*, vol. 361, no. 26, pp. 2538–2547, 2009.

[86] C. Meex *et al.*, "Direct identification of bacteria from BacT/ALERT anaerobic positive blood cultures by MALDI-TOF MS: MALDI Sepsityper kit versus an in-house saponin method for bacterial extraction," *J. Med. Microbiol.*, vol. 61, no. 11, pp. 1511–1516, 2012.

[87] J. S. Gootenberg *et al.*, "Nucleic acid detection with CRISPR-Cas13a/C2c2," *Science (80-. ).*, vol. 356, no. 6336, pp. 438–442, 2017.

[88] D. A. Giljohann and C. A. Mirkin, "Drivers of biodiagnostic development," *Nature*, vol. 462, no. 7272, p. 461, 2009.

[89] P. Craw and W. Balachandran, "Isothermal nucleic acid amplification technologies for point-of-care diagnostics: a critical review," *Lab Chip*, vol. 12, no. 14, pp. 2469–2486, 2012.

[90] S. Park, Y. Zhang, S. Lin, T.-H. Wang, and S. Yang, "Advances in microfluidic PCR for point-of-care infectious disease diagnostics," *Biotechnol. Adv.*, vol. 29, no. 6, pp. 830–839, 2011.

[91] O. Piepenburg, C. H. Williams, D. L. Stemple, and N. A. Armes, "DNA detection using recombination proteins," *PLoS Biol.*, vol. 4, no. 7, p. e204, 2006.

[92] Q. Chou, M. Russell, D. E. Birch, J. Raymond, and W. Bloch, "Prevention of pre-PCR mis-priming and primer dimerization improves low-copy-number amplifications," *Nucleic Acids Res.*, vol. 20, no. 7, pp. 1717–1723, 1992.

[93] E. H. Ashrafi and N. Paul, "Improved PCR specificity with hot start PCR primers,"

*Biotechniques*, vol. 47, no. 3, pp. 789–790, 2009.

[94] A. Ruiz-Villalba, E. van Pelt-Verkuil, Q. D. Gunst, J. M. Ruijter, and M. J. B. van den Hoff, "Amplification of nonspecific products in quantitative polymerase chain reactions (qPCR)," *Biomol. Detect. Quantif.*, vol. 14, pp. 7–18, 2017.

[95] Y. Kimura *et al.*, "Optimization of turn-back primers in isothermal amplification," *Nucleic Acids Res.*, vol. 39, no. 9, pp. e59–e59, 2011.

[96] Y. Mori and T. Notomi, "Loop-mediated isothermal amplification (LAMP): a rapid, accurate, and cost-effective diagnostic method for infectious diseases," *J. Infect. Chemother.*, vol. 15, no. 2, pp. 62–69, 2009.

[97] S. J. Reinholt and A. J. Baeumner, "Microfluidic isolation of nucleic acids," *Angew. Chemie Int. Ed.*, vol. 53, no. 51, pp. 13988–14001, 2014.

[98] C. W. Price, D. C. Leslie, and J. P. Landers, "Nucleic acid extraction techniques and application to the microchip," *Lab Chip*, vol. 9, no. 17, pp. 2484–2494, 2009.

[99] S. C. Tan and B. C. Yiap, "DNA, RNA, and protein extraction: the past and the present," *Biomed Res. Int.*, vol. 2009, 2009.

[100] B. Nasseri, N. Soleimani, N. Rabiee, A. Kalbasi, M. Karimi, and M. R. Hamblin, "Point-of-care microfluidic devices for pathogen detection," *Biosens. Bioelectron.*, vol. 117, pp. 112–128, 2018.

[101] C. Zhang and D. Xing, "Miniaturized PCR chips for nucleic acid amplification and analysis: latest advances and future trends," *Nucleic Acids Res.*, vol. 35, no. 13, pp. 4223–4237, 2007.

[102] K.-Y. Lien, W.-Y. Lin, Y.-F. Lee, C.-H. Wang, H.-Y. Lei, and G.-B. Lee,

"Microfluidic systems integrated with a sample pretreatment device for fast nucleic-acid amplification," *J. Microelectromechanical Syst.*, vol. 17, no. 2, pp. 288–301, 2008.

[103] C.-M. Chang, W.-H. Chang, C.-H. Wang, J.-H. Wang, J. D. Mai, and G.-B. Lee, "Nucleic acid amplification using microfluidic systems," *Lab Chip*, vol. 13, no. 7, pp. 1225–1242, 2013.

[104] J. Yin *et al.*, "Integrated microfluidic systems with sample preparation and nucleic acid amplification," *Lab Chip*, vol. 19, no. 17, pp. 2769–2785, 2019.

[105] B. H. Park *et al.*, "An integrated rotary microfluidic system with DNA extraction, loop-mediated isothermal amplification, and lateral flow strip based detection for point-of-care pathogen diagnostics," *Biosens. Bioelectron.*, vol. 91, pp. 334–340, 2017.

[106] J. Wen, L. A. Legendre, J. M. Bienvenue, and J. P. Landers, "Purification of nucleic acids in microfluidic devices," *Anal. Chem.*, vol. 80, no. 17, pp. 6472–6479, 2008.

[107] S. H. Lee *et al.*, "Bubble-free rapid microfluidic PCR," *Biosens. Bioelectron.*, vol. 126, pp. 725–733, 2019.

[108] C.-Y. Chao, C.-H. Wang, Y.-J. Che, C.-Y. Kao, J.-J. Wu, and G.-B. Lee, "An integrated microfluidic system for diagnosis of the resistance of Helicobacter pylori to quinolone-based antibiotics," *Biosens. Bioelectron.*, vol. 78, pp. 281–289, Apr. 2016.

[109] N. C. Cady, S. Stelick, and C. A. Batt, "Nucleic acid purification using microfabricated silicon structures," *Biosens. Bioelectron.*, vol. 19, no. 1, pp. 59–66, 2003.

[110] L. A. Marshall, L. L. Wu, S. Babikian, M. Bachman, and J. G. Santiago, "Integrated printed circuit board device for cell lysis and nucleic acid extraction," *Anal. Chem.*, vol. 84, no. 21, pp. 9640–9645, 2012.

[111] A. Rogacs, L. A. Marshall, and J. G. Santiago, "Purification of nucleic acids using isotachophoresis," *J. Chromatogr. A*, vol. 1335, pp. 105–120, 2014.

[112] S. O. Kelley, "What Are Clinically Relevant Levels of Cellular and Biomolecular Analytes?," *ACS Sensors*, vol. 2, no. 2, pp. 193–197, 2017.

[113] D. Martins, R. Levicky, and Y.-A. Song, "Enhancing the speed of morpholino-DNA biosensor by electrokinetic concentration of DNA in a microfluidic chip," *Biosens. Bioelectron.*, vol. 72, pp. 87–94, 2015.

[114] M. Li and R. K. Anand, "Recent advancements in ion concentration polarization," *Analyst*, vol. 141, no. 12, pp. 3496–3510, 2016.

[115] W. Ouyang and J. Han, "Universal amplification-free molecular diagnostics by billion-fold hierarchical nanofluidic concentration," *Proc. Natl. Acad. Sci.*, vol. 116, no. 33, pp. 16240–16249, 2019.

[116] A. K. White *et al.*, "High-throughput microfluidic single-cell RT-qPCR," *Proc. Natl. Acad. Sci.*, vol. 108, no. 34, pp. 13999–14004, 2011.

[117] P. Neuzil, C. Zhang, J. Pipper, S. Oh, and L. Zhuo, "Ultra fast miniaturized real-time PCR: 40 cycles in less than six minutes," *Nucleic Acids Res.*, vol. 34, no. 11, pp. e77–e77, 2006.

[118] K. Kolari, R. Satokari, K. Kataja, J. Stenman, and A. Hokkanen, "Real-time analysis of PCR inhibition on microfluidic materials," *Sensors Actuators B Chem.*, vol. 128,

no. 2, pp. 442–449, 2008.

[119] J.-H. Wang *et al.*, "A miniaturized quantitative polymerase chain reaction system for DNA amplification and detection," *Sensors Actuators B Chem.*, vol. 141, no. 1, pp. 329–337, 2009.

[120] T. R. Ioerger *et al.*, "Variation among genome sequences of H37Rv strains of Mycobacterium tuberculosis from multiple laboratories," *J. Bacteriol.*, vol. 192, no. 14, pp. 3645–3653, 2010.

[121] J. L. Reed *et al.*, "Highly sensitive sequence specific qPCR detection of Mycobacterium tuberculosis complex in respiratory specimens," *Tuberculosis*, vol. 101, pp. 114–124, 2016.

[122] M. M. Kulkarni, "Digital multiplexed gene expression analysis using the NanoString nCounter system," *Curr. Protoc. Mol. Biol.*, vol. 94, no. 1, pp. 25B–10, 2011.

[123] G. K. Geiss *et al.*, "Direct multiplexed measurement of gene expression with color-coded probe pairs," *Nat. Biotechnol.*, vol. 26, no. 3, p. 317, 2008.

[124] H. W. Hou, R. P. Bhattacharyya, D. T. Hung, and J. Han, "Direct detection and drug-resistance profiling of bacteremias using inertial microfluidics," *Lab Chip*, vol. 15, no. 10, pp. 2297–2307, 2015.

[125] S. S. Dukhin, "Electrokinetic phenomena of the second kind and their applications," *Adv. Colloid Interface Sci.*, vol. 35, pp. 173–196, 1991.

[126] I. Rubinstein and B. Zaltzman, "Electro-osmotic slip of the second kind and instability in concentration polarization at electrodialysis membranes," *Math. Model. Methods Appl. Sci.*, vol. 11, no. 02, pp. 263–300, 2001.

[127] I. Rubinstein, B. Zaltzman, and I. Lerman, "Electroconvective instability in concentration polarization and nonequilibrium electro-osmotic slip," *Phys. Rev. E*, vol. 72, no. 1, p. 11505, 2005.

## Journal publications during Ph.D.


[1]. **W. Ouyang**, and J. Han, "Universal Amplification-Free Molecular Diagnostics by Billion-fold Hierarchical Nanofluidic Concentration", ***Proceedings of the National Academy of Sciences of the United States of America (PNAS)***, 116(33), 16240-16249, 2019

[2]. S.H. Ko, D. Chandra, **W. Ouyang**, T. Kwon, P. Karande, and J. Han, "Nanofluidic Device for Continuous Multiparameter Quality Assurance of Biologics", ***Nature Nanotechnology***, 12(8), 804, 2017

[3]. **W. Ouyang**, Z. Li, and J. Han, "Pressure-Modulated Selective Electrokinetic Trapping for Direct Enrichment, Purification, And Detection of Nucleic Acids in Human Serum", ***Analytical Chemistry***, 90(19), 11366-11375, 2018

[4]. **W. Ouyang**, X. Ye, Z. Li, and J. Han, "Deciphering Ion Concentration Polarization-based Electrokinetic Molecular Concentration at the Micro-Nanofluidic Interface: Theoretical Limits and Scaling Laws", ***Nanoscale***, 10(32), 15187-15194, 2018 (inside front cover)

[5]. **W. Ouyang**, J. Han, and W. Wang, "Enabling Electrical Biomolecular Detection in High Ionic Concentrations and Enhancement of the Detection Limit Thereof by Coupling a Nanofluidic Crystal with Reconfigurable Ion Concentration Polarization", ***Lab on a Chip***, 7(22), 3772-3784, 2017 (outside front cover)

[6]. **W. Ouyang**, J. Han, and W. Wang, "Nanofluidic Crystals: Nanofluidics in a Close-Packed Nanoparticle Array", ***Lab on a Chip***, 17(18), 3006-3025, 2017

[7]. **W. Ouyang**, S.H. Ko, D. Wu, A.Y. Wang, P. Barone, W.S. Hancock, and J. Han, "Microfluidic Platform for Assessment of Therapeutic Proteins Using Molecular Charge Modulation Enhanced Electrokinetic Concentration Assays", ***Analytical Chemistry***, 88(19), 9669-9677, 2016

[8]. L. Gong#, **W. Ouyang#**, Z. Li, and J. Han, "Force Fields of Charged Particles in Micro-Nanofluidic Preconcentration Systems", ***AIP Advances***, 7(12), 125020, 2017 (#: equally contributed authors)

[9]. J. Niu, X. Hu, **W. Ouyang**, Y. Chen, S. Liu, J. Han, and L. Liu, "Femtomolar Detection of Lipopolysaccharide in Injectables and Serum Samples Using Aptamer-Coupled Reduced Graphene Oxide in a Continuous Injection-Electrostacking Biochip", ***Analytical Chemistry***, 91(3), 2360-2367, 2018

[10]. L. Gong, **W. Ouyang**, Z. Li, and J. Han, "Direct Numerical Simulation of Continuous Lithium Extraction from High $Mg^{2+}/Li^{+}$ Ratio Brines Using Microfluidic Channels with Ion Concentration Polarization", ***Journal of Membrane Science***, 556, 34-41, 2018

[11]. **W. Ouyang**, and J. Han, "One-Step Nucleic Acid Purification and Noise-Resistant PCR by Electrokinetic Concentration for Ultralow-Abundance Nucleic Acid Detection", *under review*